THZ DEVICE-TO-DEVICE COMMUNICATIONS: CHANNEL MEASUREMENTS, MODELLING, SIMULATION, AND ANTENNA DESIGN

A Thesis
Presented to
The Academic Faculty

by

Seunghwan Kim

In Partial Fulfillment
of the Requirements for the Degree
Doctor of Philosophy in the
School of Electrical and Computer Engineering

Georgia Institute of Technology
December 2016

THZ DEVICE-TO-DEVICE COMMUNICATIONS: CHANNEL MEASUREMENTS, MODELLING, SIMULATION, AND ANTENNA DESIGN

Approved by:

Professor Alenka Zajić, Advisor
School of Electrical and Computer Engineering
Georgia Institute of Technology

Professor Gregory Durgin
School of Electrical and Computer Engineering
Georgia Institute of Technology

Professor Andrew F. Peterson
School of Electrical and Computer Engineering
Georgia Institute of Technology

Professor Heinrich Matzinger
School of Mathematics
Georgia Institute of Technology

Professor Milos Prvulovic
School of Computer Science
Georgia Institute of Technology

Date Approved: November 3 2016

To

my parents, Sang-Woon Kim and Mi-Sook Chang,

and

my soulmate, Bella

ACKNOWLEDGEMENTS

I have been very fortunate in my life to have met so many great people. My Ph.D. years were no exception, and I have been especially lucky to have met Prof. Zajić. She has taught me what research is, how to realize, present, and communicate your ideas with other researchers. Her unshakable focus on target and right guidance has always put me on the right track whenever I strayed too far. Also, I truly appreciate her providing the motivation I needed to keep myself moving forward when things didn't go as planned.

I cannot forget to thank the committee members, Prof. Durgin, Prof. Peterson, and Prof. Matzinger, from whom I've had the honor of receiving valuable input for my research either through classes or personal discussions. One day I hope to be a researcher of such great erudition in his or her field.

I was also fortunate to have such great lab mates and friends; Hyunwoo, Michael, Rob, Derrick, Nader, Alireza, and Woody. When research hits a snag, just having someone to freely discuss the problem with makes it possible to gain a new, different perspective that often leads to a solution. I am grateful for all their input and discussions (and fun) we have had throughout my Ph.D. life.

Finally, my most sincere gratitude and respect goes to my parents, Sang-Woon and Mi-Sook, as well as my other half, Bella. Without their unrelenting support and encouragement during the past four years, this degree would not have been possible, or at least, would have been much longer, lonelier, and more tedious a journey.

TABLE OF CONTENTS

LIST OF TABLES

LIST OF FIGURES

SUMMARY

As the demand for smaller devices that can offer higher speed wireless communication any time and anywhere is growing relentlessly, the need for higher frequency bands with wide unregulated bandwidth that can support multi-Gigabits/s data rates have become essential. The opening up of carrier frequencies in the THz-range, such as D-band (i.e., 110 GHz–170 GHz) and around 300 GHz, is the most promising approach to provide sufficient bandwidth required for ultra-fast and ultra-broadband data transmission. This large bandwidth paired with higher speed wireless links can open the door to a large number of novel applications such as ultra-high-speed pico-cell cellular links, Terabits/s (Tbps) WLAN and WPAN, secure wireless communication for military and defense applications, and on-body communication for health monitoring systems.

The substance of this research is measurement, characterization, and modelling of short-range indoor THz channels that can provide ultra-high-speed communication links. Specifically, in this work, frequencies in D-band as well as the 300 GHz band (300 GHz–320 GHz) that have 20 to 60 GHz of essentially undeveloped and available bandwidths are considered. In this research, first of all, a Linearly-Tapered Slot Antenna (LTSA) that operates in the frequency range 280 GHz–320 GHz is designed, simulated, and fabricated to test the efficiency of a classical ultra-broadband antenna when operated at THz band. Secondly, the Line-of-Sight (LoS) and the Non-Line-of-Sight (NLoS) channel measurements are obtained in 300 GHz band and D-band through extensive indoor measurement campaigns, and the large- and the small-scale characterization is performed on each channel. Further, the NLoS transmissions through different propagation mechanisms, such as reflection and diffraction,

caused by obstruction of varying shapes and materials are characterized and modelled. Third, a two-dimensional (2-D) geometry-based statistical channel model for short-range THz channels is proposed and validated using the data collected from the measurement campaigns in the two THz bands. Finally, another sub-THz band around 33.25 GHz (26.5 GHz–40 GHz), or 30 GHz band, is also measured in the same environment as the two THz bands, and the comparative analysis of the three bands is done.

This work provides system designers and researchers with essential input needed for realizing THz wireless communication systems.

CHAPTER I

INTRODUCTION

1.1 Motivations

Over the last few years, the change in the way today's society creates, shares, and consumes information accompanied by the progress in wireless technologies have triggered a tremendous amount of wireless data traffic. The ever-growing need for smaller devices that can offer higher speed wireless communication anywhere and any time can only increase the required wireless data rate, which is expected to approach Terabit-per-second (Tbps) range within the next five to ten years. Advanced physical layer solutions and, more importantly, new spectral bands will be required to support these extremely high data rates.

With the current wireless systems, spectrum scarcity and capacity limitations are a serious problem. Specifically, wireless technologies below 0.1 THz are not capable of supporting Tbps links. Use of advanced digital modulation schemes, such as Orthogonal Frequency Domain Multiplexing (OFDM), as well as Multiple-Input-Multiple-Output (MIMO) radio technology has enhanced the spectral efficiency at frequencies below 5 GHz, but the scarcity of the available bandwidth imposes an upper bound on the achievable data rate. For example, in Long-Term Evolution Advanced (LTE-A) cellular networks, using a four-by-four MIMO scheme over a 100 MHz aggregated bandwidth achieves the peak data rates in the order of 1 Gbps [1]. However, these service rates are still three orders of magnitude below the targeted 1 Tbps. With modulation efficiency reaching its practical limits, a key enabler for higher speed data is the availability of wideband channels, such as those at 60 GHz with an unregulated bandwidth of 7 GHz [2]–[9]. There is an ongoing effort to migrate indoor WLAN

and WPAN toward these less congested higher frequency unlicensed spectrum bands, where data rates in the order of 10 Gbps within one meter are expected [10]. However, this is still two orders of magnitude below the Tbps demand, and the usable bandwidth at 60 GHz still limits the possibility of realizing Tbps links.

The higher spectral bands with wide enough unregulated bandwidths available for the realization of Tbps links are found in THz and optical communication bands, i.e., infrared (IR) frequencies and above, which are considered the next frontiers on the wireless technologies roadmap. Although Free Space Optical (FSO) communications offer large available bandwidth, there are several reasons that prevent us from using optical communication systems for personal wireless communications. First of all, the achievable data rate and the transmission range of FSO communication systems are limited by low transmitted power due to eye safety constraints, very high path loss as well as the impact of atmospheric affects (e.g. fog, rain, dust or pollution) on propagation, and high sensitivity to misalignment between transmitter and receiver due to extremely narrow beamwidths [11]. A infrared (IR) FSO communication system that supports 10 Gbps Line-of-Sight (LoS) wireless links has been reported in [12], and an indoor FSO communication system capable of supporting 1-Gbps link at visible light frequencies was also reported in [13]. However, as demonstrated in [14], the data rate was reduced dramatically for diffused Non-Line-of-Sight (NLoS) scenarios. More importantly, the difficulty of integrating FSO communication systems into a compact package is the major reason for their impracticality. In [15], a long-distance FSO system that supports a 1.28 Tbps link was demonstrated, but the dimensions of the optical front-end used were 12 cm $\times$ 12 cm $\times$ 20 cm and it weighed almost 1 kg, not including the signal generation/detection and modulation/demodulation blocks. All these constraints limit the feasibility of optical approach to personal and mobile wireless communications.

THz band refers to the spectral band that spans the frequencies between 0.3 THz

and 10 THz. Terahertz wireless communication has two key advantages that can be combined to achieve the required data rates. First, the usable frequency band around each frequency is much larger, so each channel can have a much higher data rate. This alone can increase data rates to several tens of Gbits/s, but multiplexing (MIMO) is still needed to reach Tbps data rates. Fortunately, THz frequencies allow smaller antennas and antenna spacing, which provides for more MIMO channels within the same array aperture. Second, since terahertz radiation can be generated by using frequency multipliers to increase operation frequencies from the millimeter-wave range, THz communication systems are compatible with the electronics that is already available for the existing mm-Wave systems, which provides a tremendous advantage over optical communication in terms of cost and integration.

The THz band is one of the least-explored frequency bands for communication. While the technology required to make THz band communication a reality is rapidly advancing with the development of new transceiver architectures and antennas built upon novel materials, there still exist several research challenges both from the device and the communication perspectives. First, the efficiency of classical ultra-broadband antennas when operated at THz band frequencies remains unknown. Therefore, an evaluation of critical performance characteristics of different types of antennas, including bandwidth, reflection, impedance, and polarization should be systematically performed in the THz band. Second, not only the Line-of-Sight, but the Non-Line-of-Sight transmissions of EM waves through different propagation mechanisms, such as reflection, scattering, and diffraction, need to be characterized, modelled, and validated with measurements for different materials at THz band frequencies. Third, a statistical model that efficiently characterizes THz multipath fading channels with parameters that affect the received multi-path signals, including the probability of the presence of LoS, that of the resolvable NLoS components, propagation delays, and path gains, needs to be developed. This thesis answers the aforementioned challenges.

1.2 Antennas for THz Communications

To design THz communication systems, we need wideband, high-gain antennas to cover the large frequency range and compensate for the high propagation loss. In addition, THz antennas need to be planar and suited to be realized in integrated or printed circuit board (PCB) technology. Although numerous antennas have been proposed in [16]-[25], they suffer from either a very limited bandwidth or bulky 3-D structure that is not desirable for antennas operating at THz frequencies since they cannot be easily integrated with the transceiver within a compact package. Another type of high-gain antenna, such as the slotted waveguide antenna, is proposed in [26]-[29]. However, the antenna performance is compromised by fabrication accuracy, material losses, and process complexity. Specifically, in [29], a SU-8-based slotted waveguide antenna designed to operate at 300 GHz is proposed, but the antenna's gain is only 5 dBi due to the resistive losses from the imperfect joints between SU-8 layers that require high precision micro-machining.

We propose that the optimal type of antenna that fulfils all three requirements, namely, high-gain, wideband, and 2-D planar structure, is the linearly-tapered slot antenna (LTSA) or Vivaldi antenna, which only differs in the way the slot is tapered. The 300 GHz multilayer LTSA has been analyzed in [30]. However, this work is based only on simulation results, which presents the maximum LTSA gain of mere 6 dBi or a very wide 3 dB beamwidth of up to 170° with a maximum gain around 3 dBi. The first objective of this thesis is to design, simulate, and fabricate a linearly-tapered slot antenna (LTSA) that operates in the frequency range $280 - 320$ GHz. A simple post-processing algorithm is developed to measure the LTSA's gain and return loss, which are verified by simulation.

1.3 THz Indoor Channel Characterization

1.3.1 300 GHz **Band**

A suitable frequency window in the THz range is found around 300 GHz, where an unregulated bandwidth of 47 GHz is available [31] and the atmospheric affects are minimal. This large bandwidth paired with higher speed wireless links can open the door to a large number of novel applications such as ultra-high-speed pico-cell cellular links, wireless short-range communications, secure wireless communications for military and defense applications, and on-body communication for health monitoring systems.

The first free-space measurements at 300 GHz with bandwidth of 10 GHz have been reported in [32]-[34] for two indoor scenarios: 1) a free-space link of devices on a desktop and 2) a free-space connection of a laptop to an access point in the middle of an office. Also, in [35], the LoS and NLoS indoor measurements obtained from [32] have been compared with ray-tracing simulation. However, no statistical characterization of 300 GHz channel has been reported so far. While deterministic channel characterization is useful, the accuracy of the ray-tracing model depends heavily on complete knowledge of material properties that require the adaptation of the model to a new environment, which can limit the time-efficiency of the model. Therefore, from the communications perspective, it is imperative to understand the large- (i.e., path loss, shadowing) and small-scale (i.e., multipath propagation) statistics of the channel that provide easy insight into the channel properties that govern communication at THz frequencies. The second objective of this thesis is to perform large- and small-scale statistical characterization of the 300 GHz channels in Line-of-Sight (LoS) and NLoS indoor scenarios with larger available bandwidth (i.e., 20 GHz of bandwidth) between the transmitter T_x and the receiver R_x on a desktop.

1.3.2 D-Band

Another potential spectral band that can be used for THz communication is D-band (110 GHz – 170 GHz). Not only that the entire 60 GHz of bandwidth at this band is unregulated and available, but the signals at this band suffer less from the free-space path loss compared to 300 GHz band, which makes it attractive for short- to medium-range indoor applications, such as WLAN and WPAN. While D-band has been extensively used for microwave atmospheric sounding (e.g., [36]), to the best of the author's knowledge, no indoor D-band channel characterization based on measurements has been reported in the open literature. Although channel characterization at 120 GHz for an indoor office scenario has been reported in [37], this work only presents ray-tracing simulation results for a single frequency in D-band.

As much as the LoS scenario, it is important for the system designer to know how different propagation mechanisms, such as reflection, diffraction, and scattering, caused by obstructions of different shapes and materials can be characterized in Non-Line-of-Sight (NLoS) environment. The third objective of this thesis is to perform large- and small-scale characterization of D-band channels in Line-of-Sight (LoS) and NLoS indoor scenarios, and to identify the types of propagation mechanisms present in various NLoS channels as well as to model the associated losses.

1.4 THz Chip-to-Chip Channel Characterization

Communication between components, such as processor and memory within a computer system, currently relies on metal wires and a transition to optical interconnects is expected in the future [38]. While optics promise much higher bandwidth (and thus improved computing performance), both wires and optics suffer from significant challenges in terms of assembly cost, airflow, service time, and overall cost, etc. [38]-[39]. For system components, the number of pins or optical interfaces that a small chip package can have is limited, and sophisticated connections can also

make component insertion (e.g. during assembly) and removal (e.g. to replace a failed component) more time-consuming and costly [40]-[42]. For communications between systems, cables (electrical or optical) require careful physical routing and "cable management" to allow good airflow (for system cooling), rapid servicing of failed computing blades/nodes, etc [43].

Wireless communication can alleviate such cable management, serviceability, and packaging constraints [43]-[54]. Integration of wireless transceivers and antennas into the chip package would provide communication bandwidth without adding pins or fiber connectors to the chip package [55]-[56]. 300 GHz channels can carry ultra-high data rate over short-range with extremely narrow beamwidth, which makes it ideal for chip-to-chip wireless links. While measurements on the computer motherboard have been reported at lower frequencies [57]-[59], to the best of our knowledge, no channel measurements in the computer motherboard environment at 300 GHz have been reported in the open literature. Chip-to-chip channel environment is that of a very densely packed communications network, where LoS is a rare condition. Therefore, it is necessary to study the THz-waves interaction with motherboard components by characterizing the path loss and multipath propagation in the numerous channel environment found on a motherboard to test the feasibility of realizing Chip-to-Chip communications in THz band, which constitutes the third objective of the thesis.

1.5 THz Statistical Channel Model

In addition to the measurement data, the THz band is also currently missing a statistical model that efficiently characterizes short-range indoor THz multipath fading channels with parameters that affect the received multi-path signals, including the probability of the presence of LoS, that of the resolvable NLoS components, propagation delays, and path gains.

Deterministic THz channel models based on the ray-tracing method has been

reported in the literature[35], where measurements obtained from a small office environment are compared with ray-tracing simulations. Other THz indoor propagation models based on ray-tracing are found in [60], where the power of a single-reflected NLoS path is modelled by a summation of clusters with standard deviation statistics of amplitude and AoA (Angle-of-Arrival) that are pre-defined for a specific wall material (plaster) in [61]. Further, the model includes reflection and scattering losses that need to be re-calculated for different polarization, dielectric constant, and Rayleigh roughness factors of the reflecting surface. As these material-specific parameters limit the practicality of ray-tracing-based channel models, for the cases when the number of multipath components is large, or when the geometry and dielectric properties of the propagation environment are unknown, we must use statistical approximations to characterize the propagation medium.

In [62], the first stochastic model for THz indoor channels is proposed. In the proposed model, the frequency-dependent path gain model [63] and the indoor Saleh-Valenzuela model [64] are adapted for the THz frequencies, and ray-tracing simulation for an office environment is performed to extract the statistical parameters that are used for the generation of a large set of channel realizations. While this approach significantly simplifies channel simulations, it does not provide insight into statistical properties, such as the correlation function (i.e., the function that characterizes how fast a wireless channel changes with time, movement, or frequency) and the power delay profile (i.e., the function that characterizes multipath propagation). These statistics enable the system designer to make informed decisions when choosing modulation, interleaving, and coding schemes at the transmitting end and the type of channel estimator and decoder at the receiving end.

The fourth objective of this thesis is to devise a two-dimensional (2-D) geometry-based statistical channel model for short-range device-to-device THz wireless channels between the stationary and directive T_x/R_x antennas, and to validate the model with

measurements obtained from the measurement campaigns conducted in 300 GHz band and D-band.

1.6 mm-Wave vs. THz Propagation

While THz band offers ultra-wide bandwidths, and therefore, ultra-high data rates, the channel suffers from inherently high free-space path loss due to its dependence on frequency. Hence, LoS signals are limited in range, and NLoS propagation is even more problematic at THz frequencies, unless it is directed, or guided, by reflections. However, even an LoS condition between transmitter and receiver is not always guaranteed in indoor environment, and the narrow beamwidth (i.e., high gain) of the antenna does not provide many other options for the signal to reach the receiver once the LoS is obstructed by non-transmissive objects. Therefore, it is of interest to investigate a lower spectrum, or the mm-Wave band, where, at the expense of available bandwidth, signals are much less attenuated by free-space propagation and antennas have wider beamwidths. This trade-off between the bandwidth and range necessitates a comparative analysis among a mm-Wave band and the two THz bands characterized above, 300 GHz and D-band.

It has been recently shown that new mm-Wave broadband cellular communication networks (5G) can be realized at frequencies 28 GHz and 38 GHz with steerable directional antennas [65]. The available bandwidth at 28/38 GHz is significantly less compared to THz bands (i.e., 1 GHz [65] vs. tens of GHz), while antennas of much wider beamwidths can be used due to the relaxed requirement on gain. Different path loss parameters and power delay profiles are expected for 30 GHz channels because of the richer multipaths due to the wider beamwidth of the antennas and different reflection/penetration losses.

The final objective of this thesis is to compare propagation mechanisms in mm-Wave channels with those in THz channels. To achieve that, we compare the same

indoor scenarios measured at D-band and 300 GHz with 30 GHz channel measurements.

1.7 Research Contributions

This section summarizes the contributions of this thesis as follows:

1. Design, simulation, and fabrication of a double-sided Linearly-Tapered Slot Antenna (LTSA) that operates at THz frequencies, i.e., between 305 GHz and 320 GHz [66]

2. Measurement and statistical characterization of $300 - 320$ GHz LoS and NLoS desktop channels [67], [68]

3. D-band ($110 - 170$ GHz) channel measurement and statistical characterization in LoS and NLoS indoor scenarios with obstructions of different shapes and materials [69], [70]

4. Measurement and modelling of losses associated with different propagation mechanisms (i.e., diffraction, reflection) in D-band and 300 GHz band NLoS channels [71]

5. Characterization of Chip-to-Chip communications channels on a computer motherboard at 300 GHz [72], [73]

6. Development of 2-D geometry-based statistical channel model for indoor short-range THz channels and its validation with measurement data [74], [75]

7. Comparative analysis of mm-Wave band (26.5 GHz–40 GHz) and THz band (D-band and 300 GHz) for LoS and NLoS indoor scenarios

1.8 Thesis Outline

The remainder of this thesis is organized as follows: Chapter 2 reviews the important concepts of statistical channel characterization and describes the two approaches to channel modeling: deterministic and statistical. Chapter 3 describes the Linearly-Tapered Slot Antenna designed for operation at 300 GHz, and presents the simulated and measured results. Chapter 4 lays out the results of measurement and statistical characterization of 300 GHz LoS and NLoS desktop channels, while those of D-band are presented in Chapter 5. Chapter 6 details another extensive measurement campaign, where the unique propagation environment of a computer motherboard is characterized for the viability of 300 GHz Chip-to-Chip communications channel, and Chapter 7 presents the 2-D geometry-based parametric reference and simulation models for indoor short-range THz channels along with experimental verification with the measurement data collected from Chapter 4, 5, and 6. Finally, Chapter 8 compares the mm-Wave band propagation mechanisms with those of the THz bands, and the thesis is concluded in Chapter 9 with the summary of its research contributions and future research directions.

CHAPTER II

BACKGROUND

This chapter briefly reviews important channel statistics that will appear repeatedly in this thesis. Also, the two approachees to channel modeling; deterministic and statistical, as well as their application in THz bands are reviewed.

2.1 Statistical Channel Characterization

Channel statistics can be classified as either large- or small-scale statistics. Large-scale statistics pertain to large-scale fading, such as path loss and shadow fading, that are dominant when the receiver moves over distances greater than several tens of the carrier wavelength. Large-scale fading plays an important role in determining the cell coverage area, outage, and handoffs. On the other hand, small-scale statistical properties of the channel are related to small-scale fading that is caused by multipath propagation. This effect plays an important role in determining link level performance in terms of bit error rates, average fade durations, etc.

2.1.1 Large-Scale Statistics

Path loss is the attenuation in the transmitted signal as it propagates from the transmitter ($\mathrm{T_x}$) to the receiver ($\mathrm{R_x}$). This attenuation may be caused by effects such as free-space propagation loss in an LoS environment, while other mechanisms, such as diffraction, reflection, and absorption, can affect it in an NLoS environment.

The simplest path loss model assumes a line-of-sight (LoS) link between the Tx and Rx and propagation in free space. Under these assumptions, the received signal power is given as [76]

$$P_R = P_T G_T G_R \frac{\lambda^2}{4\pi d^2}, \tag{1}$$

where P_T is the transmitted power; G_T and G_R are the transmit and receive antenna gains, respectively; λ is the carrier wavelength, and d is the distance between the T_x and R_x. The signals in wireless communications, however, do not experience free space propagation. Therefore, several different models such as the Okumura-Hata, Lee, Walfish-Ikegami, etc., have been proposed to model path loss in different propagation environments such as urban, rural, and indoor areas [76]. A detailed description of different path loss models can be found in [76]. The path loss models described above assume that the path loss is constant at a given distance. However, the presence of obstacles such as buildings and trees results in random variations of the received power at a given distance. This effect is called shadow fading. Experimental results show that shadow fading can be modeled as a log-normal random variable. The shadow fading distribution is given by [76]

$$f_{\Omega_p}(x) = \frac{10}{x\sigma_\Omega\sqrt{2\pi}\ln 10}\ \exp\left[-\frac{(10\log_{10}x - \mu_{\Omega_p(\mathrm{dBm})})^2}{2\sigma_\Omega^2}\right], \tag{2}$$

where Ω_p denotes the mean squared envelope level, μ_{Ω_p} is the area mean expressed in dBm and σ_Ω is the standard deviation of the shadow fading. Typical σ_Ω values range from 5–10 dB.

The large-scale statistics of the channel are characterized by the parameters, γ, the path loss exponent, and σ, the standard deviation of shadow fading, that are obtained from the distance-domain measurements of path loss, where displacement is greater than several tens of λ. γ characterizes how rapidly path loss increases (or decreases) with increasing separation distance between the T_x and the R_x, while σ characterizes the variation in measured path losses.

A single-slope log-distance path loss model can be written as

$$PL(d) = 10\gamma\log_{10}\left(\frac{d}{d_0}\right) + PL(d_0) + X_\sigma, \tag{3}$$

where $PL(d)$ is the path loss in dB at the distance d, $PL(d_0)$ is the free-space path loss at the reference distance d_0, and X_σ represents the shadow fading that can be

modelled as a zero-mean Gaussian distributed random variable (in dB) with standard deviation σ.

More advanced statistical models can be devised from the measurements if the single slope model does not produce adequate fit. However, for THz indoor scenarios that are of interest in this thesis, the single-slope model has been found to provide sufficiently accurate fit to the measurements. The alternative approach is a deterministic approach (e.g. ray-tracing [35] and diffraction modeling [61]), which is expected to produce more repeatable results; however, it depends on the detailed and accurate description of all objects in the propagation space.

2.1.2 Small-Scale Statistics

The presence of local scattering objects often obstructs a direct wave path between the T_x and R_x. Then, a non-line-of-sight (NLoS) propagation path will exist between the T_x and R_x. As a consequence, the waves must propagate via reflection, diffraction, and scattering. At the receiver, waves arrive from many different directions and with different delays. The multiple waves combine vectorially at the receiver antenna (a phenomenon called multipath fading) to produce a composite received signal. Diffuse wave components arise under NLoS propagation due to the presence of scatterers in the environment. In the presence of such diffuse components, the fading is described by a Rayleigh distribution. However, when a specular component, i.e., LoS or a strong reflected path, also arrives at the receiver, the fading is described by a Rician distribution. The channel can be modeled by a linear time-variant filter that has the complex low-pass impulse response [76]

$$h(t,\tau) = \sum_{l=1}^{L} g_l(t)\delta(\tau - \tau_l), \tag{4}$$

where L is the total number of resolvable multipath components, $g_l(t)$ is the time-varying complex faded envelope associated with the l^{th} resolvable multipath component arriving with an average time delay τ_l. Each time-varying complex faded

envelope $g_l(t)$ is either Rayleigh or Rician faded.

Time selectivity and frequency selectivity are two important properties of the channel impulse response. Time selectivity refers to the property that the channel impulse response changes with time. This is caused by the motion of the T_x, the R_x, and/or the scatterers. When viewed in the frequency domain, time selectivity appears as Doppler shifts in the transmitted signal, causing a broadening of the transmitted signal spectrum. This effect is also called frequency dispersion. Based on the rate with which the channel impulse response changes relative to the signal transmission rate, channels may be classified as fast fading or slow fading. Fast fading implies that the channel changes within the transmitted symbol duration, while slow fading implies that the channel is approximately constant within a symbol duration. A good measure of channel selectivity is given by the channel coherence time, or equivalently, the Doppler spread, i.e., the time duration for which the channel can be considered as approximately time-invariant. Time selectivity is not relevant in this thesis since T_x and R_x as well as any scatterers in the channel are in movement (i.e., channel is time-invariant).

Frequency selectivity refers to the property that the channel impulse response changes with frequency. Multipath components that arrive with different time delays cause this frequency selectivity. Based on their degree of frequency selectivity, channels may be classified as frequency-flat or frequency-selective channels. If all the transmitted frequencies undergo approximately identical amplitude and phase changes, the channel is called frequency-flat. On the other hand, if all transmitted frequencies experience different amplitude and phase changes, the channel is termed frequency-selective.

The small-scale statistics result from this frequency selectivity of the channel. The variation of path loss about the mean value in frequency-domain translates to the number of multipaths in the delay domain through Fourier Transformation, i.e., the

more multipaths are detected, the more variation in the frequency response. It follows that the small-scale statistics of the channel are characterized by the parameter, τ_{rms}, or the RMS delay spread, which is a good estimate of how multipath-rich the channel is. RMS delay spread, in turn, is directly related to the coherence bandwidth ($B_c \propto \frac{1}{\tau_{rms}}$), i.e., the bandwidth over which the channel's frequency response remains constant. The channel can be considered frequency-flat only if the transmission is narrowband compared to the channel's coherence bandwidth. Otherwise, the channel is frequency-selective.

2.2 Deterministic Channel Modeling

Deterministic channel models aim to solve Maxwell′s equations in either an exact or an approximate way. Different propagation mechanisms that each ray experiences during its travel from the transmitter to the receiver are modeled separately in a deterministic fashion.

2.2.1 Reflection and Transmission

Reflection from, and transmission through, dielectric objects are important propagation mechanisms that show frequency dependence due to the frequency-varying dielectric properties of most materials that impacts the reflection and transmission coefficients of the considered objects. Moreover, the transmission through a dielectric layer is governed by the equation [77]

$$T = \frac{T_1 T_2 e^{-j\alpha(f)}}{1 + \rho_1 \rho_2 e^{-2j\alpha(f)}}, \tag{5}$$

where T and ρ represent the transmission and reflection coefficients, and the subscripts 1 and 2 indicate the medium air and the dielectric, respectively. $\alpha(f)$ is the frequency-dependent electrical length of the dielectric as seen by waves that are at an angle Θ_t with the layer

$$\alpha = \frac{2\pi}{c_0} f \sqrt{\epsilon_r} d_{layer} \cos\Theta_t, \tag{6}$$

where d_{layer} is the geometrical width of the layer. A more detailed analysis is given in [78], [79].

2.2.2 Diffraction

Another propagation mechanism, through which signals can reach the receiver in NLoS environment, is diffraction at the edge of a screen or a wedge. For diffraction by a half-plane, the complex-valued amplitude of the scattered field at the distance r with a sinusoidal incident field $x_i = A_0 \exp(j\omega t)$ is given by [80]

$$\begin{aligned} x(j\omega) = {} & A_0 e^{jkr\cos(\phi-\phi_0)} F\left(\sqrt{2kr}\cos(\phi-\phi_0)\right) \\ & \pm A_0 e^{jkr\cos(\phi+\phi_0)} F\left(\sqrt{2kr}\cos(\phi+\phi_0)\right), \end{aligned} \tag{7}$$

where $F(x) = (e^j(\pi/4))/(\sqrt{\pi}) \int_x^\infty e^{j\mu^2} d\mu$ and the plus and minus signs denote the **H** and **E** polarization of the incident field. ϕ_0 and ϕ are the incident and observation angles, respectively; $k = \omega/c_0$ is the wave number. A detailed mathematical framework for diffraction by screens as well as wedges and electrically large objects can be found in the book chapter [80].

2.2.3 Scattering on Rough Surfaces

When an incident ray impinges on a rough reflecting surface, a certain amount of the incident power is scattered diffusely. According to the Kirchhoff theory [81], the reflection coefficient of a rough surface, which also shows a strong dependence on frequency, can be expressed as

$$\rho_{rough}(f) = \rho_{smooth} \exp\left[-2\left(2\pi \frac{f}{c_0} \sigma_h \sin\phi_0\right)^2\right], \tag{8}$$

where σ_h is the standard deviation of the height distribution, ϕ_0 is the angle of incidence, and ρ_{smooth} is the reflection coefficient of the surface if it were smooth.

2.2.4 Deterministic Channel Models at THz band

Priebe et al. have developed an in-house Ray-Tracing (RT) simulation tool [35] that deterministically predicts the THz indoor channel behavior by modeling the propagation mechanisms at THz band. The details regarding the modeling of diffraction, reflection, and scattering, as well as the building material characterization at THz frequencies, can be found in [61], [82], [34], and [83], respectively. The RT simulation results are validated with 300 GHz indoor measurements in small office environment that features plaster walls, a wooden table, a door, a plastic wardrobe, and a glass window. The comparison between the simulated power delay profile and channel transfer function with the measured ones reveals that the RT model can either over or underestimate the amplitudes of the measured paths by up to 8 dB even with the slightest discrepancies in the alignment and positioning of the T_x and R_x as well as the office dimensions. Furthermore, due to the small wavelength of 1 mm at 300 GHz, these minute spatial inaccuracies also lead to discrepancies in times of arrival and phase errors that cause fading dips in the simulated transfer function to appear at different frequencies compared to the measurement. Furthermore, the propagation mechanism considered in the RT model is limited only to the specular reflections from specific angular ranges, with no regard to scattering on rough surfaces or diffraction that would increase the complexity and the time required for the simulation even more.

In summary, the precision of the deterministic predictions of the channel through Ray-Tracing heavily depends on the thorough knowledge of material parameters that are not always available a priori, and they need to be re-calculated even for the slightest changes in the environment in regards to the geometry or the materials of

the objects. Also, when multiple propagation mechanisms occur simultaneously, their correct modeling can be very difficult and further complicate the simulation.

2.3 Statistical Channel Modeling

For the simulation and testing of wireless systems, stochastic channel models are popular since they reflect the essential properties of propagation channels, without trying to emulate the exact behavior for each specific location.

2.3.1 Path Gain

The path gain in a narrowband system is conventionally defined as

$$G_{pr}(d) = \frac{E[P_r(d, fc)]}{P_t}, \tag{9}$$

where the expectation is taken over an area that is large enough to average out the large-scale fading due to shadowing as well as the small-scale fading due to multipaths, i.e., $E[\cdot] = E_{ls}[E_{ss}[\cdot]]$, where subscripts ls and ss indicate large scale fading and small scale fading, respectively.

In UWB channels, the path gain (i.e., negative of path loss) is a function of not only the distance, but also the frequency. Therefore, the frequency-dependent path gain (related to wideband path gain in [84], [85]) is defined as

$$G_{pr}(d, f) = E\left[\int_{f-\Delta f/2}^{f+\Delta f/2} |H(\widetilde{f}, d)|^2 d\widetilde{f}\right], \tag{10}$$

where $H(f, d)$ is the channel transfer function, and Δf is chosen, such that the material properties (e.g., diffraction coefficients, dielectric constants, etc.) can be considered constant within that bandwidth. The total path gain is obtained by integrating over the whole bandwidth of interest.

2.3.2 Multipath Propagation

It had been recognized in many channel investigations that multipath components (MPC's) tend to arrive in clusters. The most popular way to reflect this mathematically is the Saleh-Valenzuela (SV) model [64] and its modifications. SV describes the impulse response as

$$h(t) = \sum_{l=0}^{L} \sum_{k=0}^{K} a_{k,l} \exp(j\phi_{k,l}) \delta(t - T_l - \tau_{k,l}), \tag{11}$$

where $a_{k,l}$ is the tap weight of the k^{th} component in the l^{th} cluster, T_l is the delay of the l^{th} cluster, $\tau_{k,l}$ is the delay of the k^{th} MPC relative to the l^{th} cluster arrival time T_l . The phases $\phi_{k,l}$ are uniformly distributed i.e., for a bandpass system, the phase is taken as a uniformly distributed random variable in the range $[0,\ 2\pi]$. K is the number of MPC's within a cluster. L is the number of clusters; it can either be assumed fixed [86], or considered to be a stochastic variable [87], [88].

A number of different models have been proposed for the arrival times of MPC's within a cluster:

1. Regularly spaced arrival times: All MPC's lie on a regular grid $T_l + \tau_{k,l} = i\Delta$, where Δ is the sampling interval [89], [90].

2. Poisson arrival times: Arrival times within a cluster is a Poisson process. The probability density function for the arrival of k^{th} MPC, given the arrival time of the previous MPC, $\tau_{(k1),l}$, can be written as

$$p(\tau_{k,l}|\tau_{(k-1),l}) = \lambda_l \exp[-\lambda_l(\tau_{k,l} - \tau_{(k-1),l})],\ k > 0, \tag{12}$$

where $\tau_{0,l} = 0$.

3. Mixed Poisson process [91]:

$$\begin{aligned} p(\tau_{k,l}|\tau_{(k-1),l}) &= \beta\lambda_1 \exp[-\lambda_1(\tau_{k,l} - \tau_{(k-1),l})] \\ &+ (1-\beta)\lambda_2 \exp[-\lambda_2(\tau_{k,l} - \tau_{(k-1),l})],\ k > 0, \end{aligned} \tag{13}$$

where β is the mixture probability, and λ_1 and λ_2 are the ray arrival rates.

The most common model for the power delay profile that determines the shape of each cluster is a one-sided exponential decay

$$E[|a_{k,l}|^2] \propto \Omega_l \exp(-\tau_{k,l}/\gamma_l), \tag{14}$$

where Ω_l is the integrated energy of the l^{th} cluster, and γ_l is the intracluster decay time constant. The cluster powers, averaged over the large scale fading, in general follow an exponential decay

$$10\log(\Omega_l) = 10\log(\exp(-T_l/\Gamma)), \tag{15}$$

The intercluster decay time constant Γ is typically around 10 – 30 ns, while widely differing values (between 1 and 60 ns) have been reported for the intracluster constant γ, see, e.g., [87], [89], [92], [93], [94]. Like the inter-path arrival times ($1/\lambda$), the inter-cluster arrival times are also a Poisson process,

$$p(T_l|T_{l-1}) = \Lambda \exp\{-\Lambda(T_l - T_{l-1})\}, \tag{16}$$

where Λ is the cluster arrival rate (assumed to be independent of l), and $1/\Lambda$ is typically in the range of 10 – 50 ns [87], [92], [93], [95].

2.3.3 Amplitude Variations

The amplitude of the k^{th} MPC, $a_{k,l}$ in Eq. (11), varies over a small area due to the superposition of unresolvable MPC's. In narrowband systems, many MPC's fall

within each resolvable delay bin, such that the central limit theorem is applicable, and the amplitudes of the bins exhibit a Rayleigh distribution over time. In UWB systems, the width of each delay bin, and therefore, the number of superimposing MPC's is much smaller, and it has been empirically determined that alternative amplitude distributions must be used:

1. Nakagami distribution: Observed in [89], [94], [96], the pdf of Nakagami distribution is given by

$$\text{pdf}(x) = \frac{2}{\Gamma(m)} \left(\frac{m}{\Omega}\right)^m x^{2m-1} \text{exp}\left(-\frac{m}{\Omega}x^2\right), \tag{17}$$

   where $m \geq 1/2$ is the Nakagami m-factor; $\Sigma(m)$ is the gamma function, and Ω is the mean-square value of the amplitude. The m-parameter is often modeled as a random variable [89].

2. Rice distribution: The Rice distribution, which is used in [97] and [96], describes the envelope of a sum of one dominant component and many smaller components. Its pdf is given by

$$\text{pdf}(x) = 2(1+K)xe^{-K-(1+K)x^2} I_0\left(2x\sqrt{K(K+1)}\right), \tag{18}$$

   where K is the rician factor, which is the ratio of the strong specular power to the sum of smaller diffuse power, and $I_0(\cdot)$ is the zero-th order modified Bessel function of the first kind.

3. Lognormal distribution: Suggested for use in UWB by [98], the lognormal distribution is described by

$$\text{pdf}(x) = \frac{20/\ln 10}{x\sigma_x\sqrt{2\pi}} \text{exp}\left[-\frac{\left(20\log_{10}(x) - \mu_{dB}\right)^2}{2\sigma_x^2}\right], \tag{19}$$

where σ_x is the standard deviation of x, and μ_{dB} is the mean of the values of x expressed in dB. With this distribution, the small-scale and the large-scale fading statistics have the same form; the superposition of lognormal variables can also be well approximated by a lognormal distribution [76]. In [99], it has also been reported that the deviations of $|h(\tau)|^2$ around the PDP can be modeled as a lognormal process.

4. Weibull distribution: [100], [101] have suggested to either model the amplitudes, or the deviation of $|h(\tau)|^2$ around the PDP, respectively, using a Weibull distribution.

5. Rayleigh distribution: When the K factor in Eq. (18) approaches 0, or when the dominant component disappears, the amplitudes of the bins follow a Rayleigh distribution, even when the resolvable binwidth is very small. For example, [90] observed Rayleigh fading in an industrial environment with many metallic objects for a 7.5 GHz measurement bandwidth.

Several papers have also found that the fading depth increases with increasing delay [89], [97].

2.3.4 Stochastic Channel Models at THz band

A statistical indoor channel model at 300 GHz for a small office scenario has been proposed by Priebe et al. in [62], where the concepts of UWB channels, such as frequency-dependent path gain and the temporal amplitude decay according to the SV model are adopted to the THz band (275 GHz – 325 GHz). The model generates fast channel realizations based on statistical parameters collected through Ray-Tracing simulations in space-, time-, and frequency-domains.

The channel realizations are contrasted to Ray-Tracing simulations in terms of the CDF's of Rician factor, K, and the angular spread of Angle-of-Arrival's (AoA's),

σ_{AoA}. Both the RT simulation and statistical model predicts the K factor in the range 0.5 – 10, but the model slightly overestimates K on average. Also, σ_{AoA}'s in the range 1.5° – 25° and 1.5° – 55° are obtained in elevation and azimuth planes, respectively. In case of the elevation, the CDF's agree well with deviations of no more than a few degrees, whereas the azimuth angular spreads deviate by up to 10°. The underlying reason for these deviations is that all R_x positions have been incorporated in the derivation of the model parameters, whereas the channel conditions in the office are position-specific. Therefore, the randomized reflected amplitudes, number of reflections, and the AoA/AoD ranges, etc. can differ from RT predictions. Nevertheless, the authors conclude that the statistical model simplifies the channel realization greatly, while still reproducing the THz broadband spatio-temporal channel properties from ray tracing or measurements sufficiently well. While this work could confirm the validity of statistical approach for the generation of THz channel transfer functions in a small office environment, it does not provide insight into important statistics of the indoor THz channels, such as path gain exponent (γ), shadowing variance (σ), RMS delay spread (τ_{rms}), and channel coherence bandwidth (B_c). Especially, the small-scale statistics, i.e, τ_{rms} and B_c, associated with the power delay profile and frequency correlation function, respectively, enable wireless system designers to make informed decisions when choosing modulation, interleaving, and coding schemes at the transmitting end and the type of channel estimator and decoder at the receiving end.

CHAPTER III

300GHZ LINEARLY TAPERED SLOT ANTENNA DESIGN AND MEASUREMENTS

3.1 Overview

Antennas operating at THz band frequencies must have high gain and wide bandwidth. The former is required to compensate for the high path loss of THz channels, and the latter is necessary to take advantage of the wide range of frequencies available in THz band. In addition, a planar (2-D) structure with small dimensions is required for a THz antenna for integration and packaging purposes. Several antennas have been designed to satisfy either or both of these requirements. In [16]-[20], high-gain antennas are proposed by combining elliptical dielectric lenses and slots or dipole feeds. However, these antennas suffer from a very limited bandwidth and bulky 3-D structure that is not desirable for antennas operating at THz frequencies. To address the problem of narrow bandwidth, leaky lens antennas are proposed in [21]-[25], but they still have the 3-D geometry that prevents them from being easily integrated with the transceiver within a compact package. Another type of antenna that features a high-gain characteristic is the slotted waveguide antenna, and several different non-mechanical-machining-based techniques to fabricate them have been proposed in [26]-[28]. However, the antenna performance is compromised by fabrication accuracy, material losses, and process complexity. A SU-8-based slotted waveguide antenna designed to operate at 300 GHz has been proposed in [29]. Although the antenna presents a simple and cost-effective SU-8 technique, the multi-layered structure requires high precision micro-machining, where even a slight gap between the layers leads to significant power loss. Further, due to the resistive losses from the imperfect

joints between SU-8 layers, the measured gain of the antenna is only 5 dBi, which is insufficient for THz channels. Finally, the optimal type of antenna that fulfils all three requirements, namely, high-gain, wideband, and 2-D planar structure, is the linearly-tapered slot antenna (LTSA) or Vivaldi antenna, which only differs in the way the slot is tapered. The 300 GHz multilayer LTSA has been analyzed in [30]. However, this work is based only on simulation results, which presents the maximum LTSA gain of mere 6 dBi or a very wide 3 dB beamwidth of up to 170° with a maximum gain around 3 dBi.

In this chapter, a linearly tapered slot antenna (LTSA) that covers 305–320 GHz frequency range has been designed, simulated and fabricated. Simulations show that antenna has gain of 13 dBi and a return loss below 10 dB across the 300–320 GHz frequency range, which are verified experimentally. The LTSA has been fabricated using a standard PCB milling machine and the Rogers RT/Duroid 5880 material.

One of the main obstacles in designing THz communication systems is the cost of testing equipment. To overcome this problem, it is also shown here how pairing a relatively low-cost 305–320 GHz communication system with a 10 MHz–30 GHz vector network analyzer (VNA), and using additional signal processing, can be used to calculate the gain and return loss of a tested antenna.

The remainder of this chapter is organized as follows: Section 3.2 describes the LTSA design and fabrication. Section 3.3 presents the measurement setup, and Section 3.4 details the signal post-processing to obtain the gain and return loss of the measured antenna. Section 3.5 compares the simulated and measured results, and finally, Section 3.6 presents some concluding remarks.

3.2 Antenna Design and Fabrication

Figure 1 shows the layout of the proposed 300 GHz LTSA. The layout consists of 2 copper layers, each having a slot tapered from the top of the WR-3 waveguide to the

top of the antenna. The antenna has been simulated with CST [102] and fabricated on a 15 mil Rogers RT/Duroid 5880 R3 board using a standard PCB milling machine. The dielectric constant of the material is $\epsilon_r = 2.2$ and the copper thickness is 36 μm. The design parameters (i.e., initial slot width a, tapered end slot width b, slot length h, substrate thickness t, and the flare angle of the tapered slot θ) and their numerical values are summarized in Table 1.

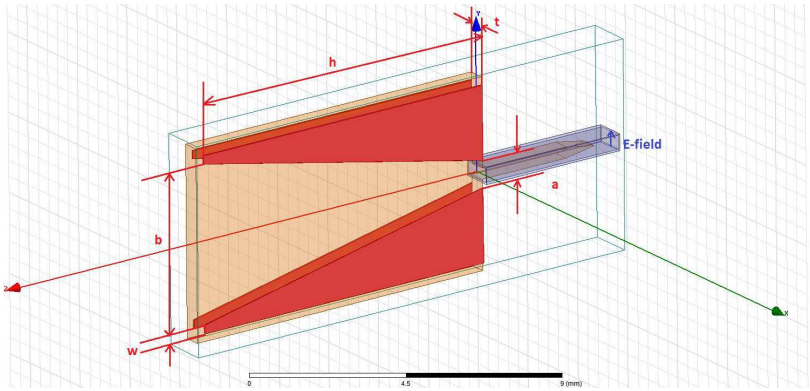

Figure 1: Linearly tapered slot antenna design.

Table 1: LTSA Design Parameters.

Parameter	Symbol	Value
Initial slot width	a	863.6 µm
End slot width	b	5 mm
Slot length	h	10 mm
Substrate thickness	t	381 µm
Flare angle	θ	11.7°

To connect our LTSA to the measurement system described in Section 3.3, we had to include a tail section that is inserted into the WR-3 waveguide as shown in Fig. 5. We have designed the tail in a way that it not only serves as the connection between the antenna and the waveguide, but it also helps reduce the reflections inside the waveguide. By introducing the tail section, the propagating wave does not experience an abrupt change of medium (from air to Duroid), which leads to smaller reflections at the waveguide-antenna interface. The CST simulation results are shown in Fig. 2.

We can observe that the average antenna gain is around 13 dBi and the return loss is below 10 dB across all frequencies.

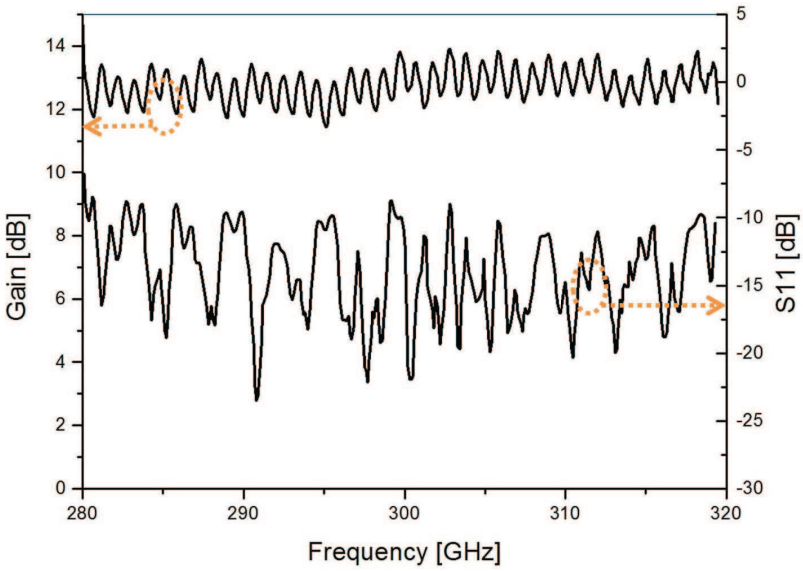

Figure 2: Simulated linearly tapered slot antenna gain and return loss.

3.3 Measurement Setup

The measurement setup consists of the N5224A PNA vector network analyzer (VNA), the VDI transmitter (Tx210) and the VDI receiver (Rx148). The N5224A VNA provides an input signal in the range 10 MHz–20 GHz. In the VDI Tx210 transmitter, the terahertz-range carrier signal starts out as a 25 GHz signal, which is generated by a Herley-CTI phase-locked dielectric resonator oscillator (DPRO with 100 MHz reference crystal oscillator) [103]. This signal is amplified and its frequency is doubled using a Norden N08-1975 [104], and then tripled using a VDI WR6.5X3 [105]. This signal is then fed to the sub-harmonic mixer that plays a dual role of doubling the carrier frequency and mixing it with the baseband signal (10 MHz–20 GHz, delivered by the VNA) [106]. The resultant terahertz-range signal is then transmitted by the horn antenna that has a gain of 23 dBi in the range 280–320 GHz. At the receiver side, the same components are used to down-convert the signal, except that the DPRO is tuned to 24.2 GHz, resulting in a down-conversion of the received RF signal

to an IF signal of 9.6 GHz. The upper sideband of the down-converted signal is then recorded by the VNA in the frequency range of 9.6–29.6 GHz. The corresponding block diagram is shown in Fig. 3. By recording the frequency dependent scattering parameter S_{21} for the test signal frequencies $f_{\text{test}} = 10$ MHz $-$ 20 GHz at the VNA, the channel transfer function at $f = 300$ GHz $+ \text{f}_{\text{test}}$ is measured.

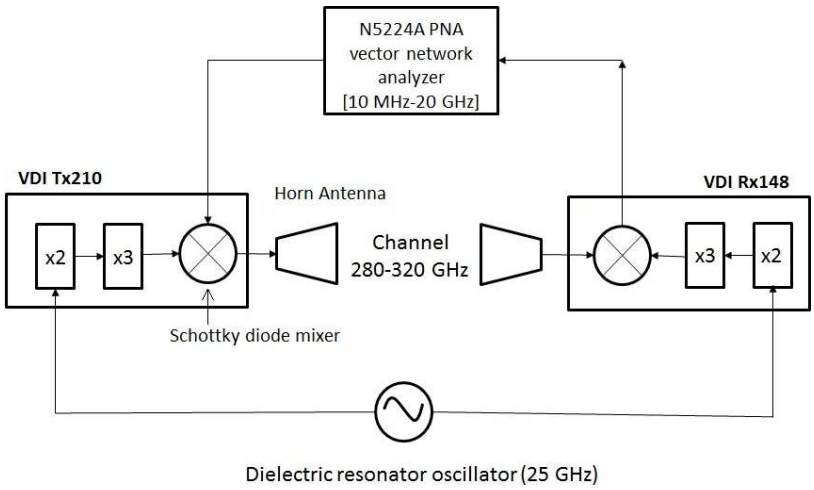

Figure 3: The 280–320 GHz measurement setup.

It has been found that the inherent loss in the transceiver is very high (40-50 dB) and that this loss has to be de-embedded from any S_{21} measurements to obtain true S_{21} transfer functions. The bandwidth of 15 GHz is used in all measurements to avoid the T_x amplifier distortions present in the range of 300–305 GHz. This provides a temporal resolution of 0.067 ns.

The start frequency is bound to a minimum of 10 MHz by the VNA and the stop frequency could not exceed the system limitations of 20 GHz. Due to input power restrictions of the mixers, a test signal with a power of -5 dBm is used, providing a dynamic range of approximately 90 dB for the chosen intermediate frequency filter bandwidth of $\Delta_{IF} = 10$ kHz. The number of sweep points is set to 801, and the maximum excess delay is 53 ns.

To obtain the gain and the return loss of the fabricated LTSA, two measurement

scenarios have been employed. First, the channel transfer function, S_{21}, is measured between the two identical horn antennas, one on the T_x and the other on the R_x module as shown in Fig. 4. This measurement setup is used to find the frequency dependent gain and return loss of the horn antenna.

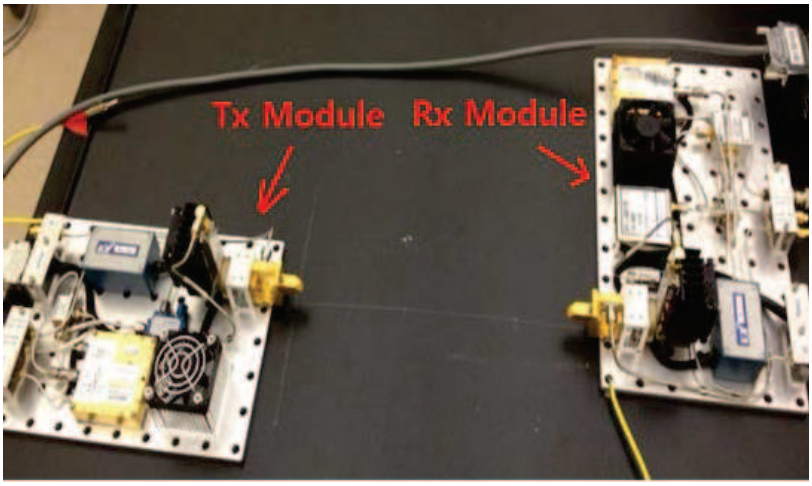

Figure 4: Photograph of the measurement scenario when the transfer function S_{21} is measured between two horn antennas.

Second, S_{21} is measured between the horn antenna on the T_x and the LTSA on the R_x side, as shown in Fig. 5, to find the frequency dependent gain and return loss of the LTSA. The post-processing of the measured data is described in Section 3.4.

3.4 Post-processing of Measured Data

This section describes the signal processing used to obtain the gain and the return loss of the LTSA. The steps of signal post-processing are as follows:

1. The transceiver loss is de-embedded from the measured S_{21}. This step is necessary because the system calibration can only be performed at the input and the output of the T_x and R_x modules, while the transceiver introduces significant frequency-dependent loss into the system.

2. The measured channel transfer function between two horn antennas is used to calculate the frequency dependent gain and S_{11} of the horn.

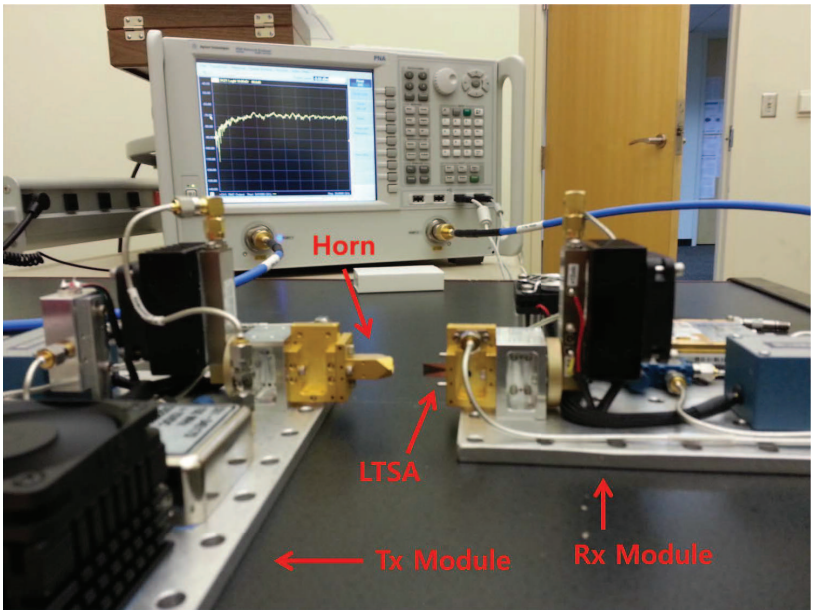

Figure 5: Photograph of the measurement scenario when the transfer function S_{21} is measured between the horn and the LTSA.

3. The obtained gain and S_{11} of the horn from Step 2 along with the measured S_{21} between the horn and LTSA are used to calculate the frequency dependent gain and S_{11} of the LTSA.

The following two subsections describe the detailed signal processing techniques used in steps 2 and 3.

3.4.1 Horn-to-Horn Measurement Scenario

Figure 6 shows the diagram of the horn-to-horn measurement scenario.

To obtain the frequency dependent gain of the horn antenna, we use the Friis equation [107]:

$$P_{out}\ [\text{dB}] = P_{in}\ [\text{dB}] + 2G_{horn}\ [\text{dB}] - PL\ [\text{dB}], \tag{20}$$

where $P_{out} - P_{in}$ is the measured transfer function S_{21}, G_{horn} is the frequency-dependent gain of the horn antenna, and PL is the free-space path loss, which can be theoretically calculated as [108]

$$PL = 20\log_{10}\frac{4\pi d}{\lambda}, \tag{21}$$

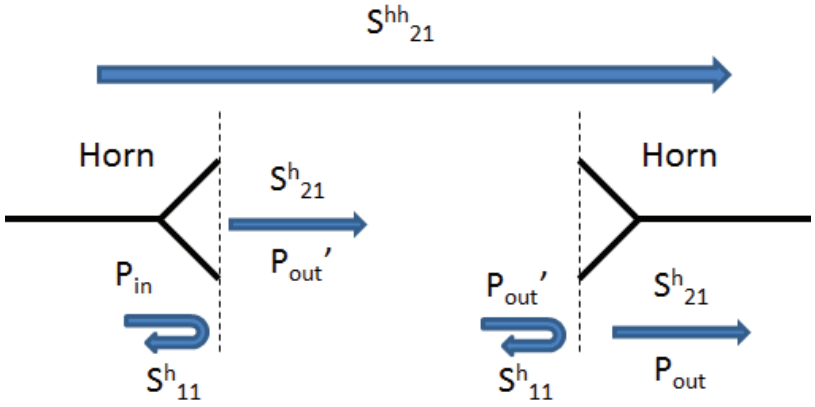

Figure 6: Diagram of the horn-to-horn measurement scenario.

where d denotes the distance between two horn antennas, and λ is the wavelength. In this measurement scenario, the distance between the horn antennas was $d = 10$ cm.

To find the S_{11} of the horn, we consider the diagram shown in Fig. 6. Here, the $\mathrm{T_x}$ and the $\mathrm{R_x}$ antennas have the same reflection and transmission coefficients, S_{11}^h and S_{21}^h, since two identical horn antennas are used. Assuming that the horn has 100% efficiency, the relationship between S_{11}^h and S_{21}^h can be defined as [109]:

$$|S_{11}^h|^2 + |S_{21}^h|^2 = 1. \tag{22}$$

The measured S_{21} includes path loss and twice the horn gain, which need to be compensated for to find the true channel transfer function. Therefore, S_{21}^{hh} in Fig. 6 is calculated as

$$S_{21}^{hh} = S_{21deembed} + PL - 2G_h, \tag{23}$$

where $S_{21deembed}$ refers to the measured S_{21} after the de-embedding of the transceiver loss, and G_h is the average of the frequency dependent horn gain. From Fig. 6, we can relate S_{21}^h and S_{21}^{hh} as follows:

$$|S_{21}^{hh}|^2 = |S_{21}^h|^2 |S_{21}^h|^2 \tag{24}$$

which leads to

$$|S_{21}^h|^2 = |S_{21}^{hh}|. \tag{25}$$

Finally, S_{11}^h can be found by substituting (25) into (22) as

$$|S_{11}^h| = \sqrt{1 - |S_{21}^{hh}|}. \tag{26}$$

The measured (i.e., post-processed) S_{11} and gain of the horn are shown in Fig. 7. They are also compared with simulated S_{11} and gain of the horn antenna to verify our approach. The comparison is further discussed in Section 3.5.

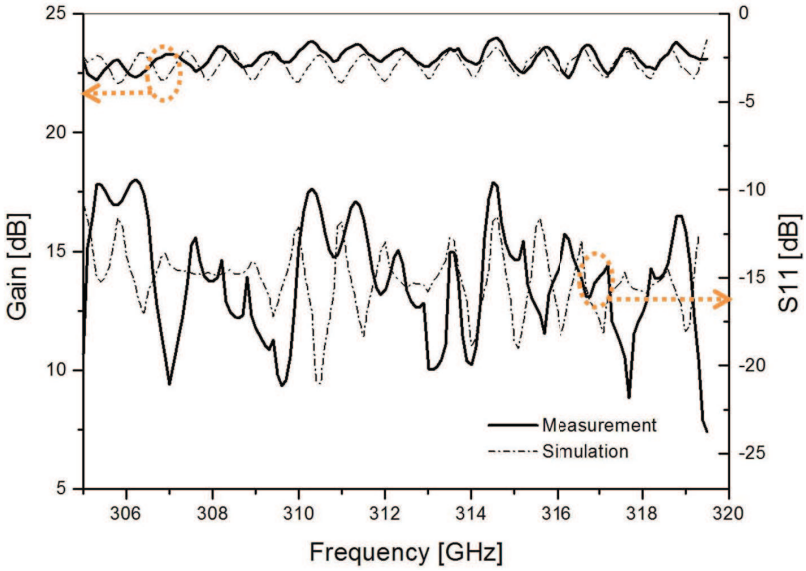

Figure 7: Simulated and measured horn antenna gain and S_{11}.

3.4.2 Horn-to-LTSA Measurement Scenario

The algorithm described in Section 3.4.1 is also used in the second measurement scenario to find the gain and the return loss of the LTSA. The only modification from the first scenario is that the R_x horn antenna is now replaced with the proposed LTSA, and the S_{11}^h and S_{21}^h on the R_x side, and S_{21}^{hh} in Figure 6 are substituted with S_{11}^l, S_{21}^l, and S_{21}^{hl}, respectively. Note that the separation distance of $d = 1.5$ cm has been chosen in this measurement scenario to ensure direct line of sight between the horn and LTSA, as illustrated in Fig. 5.

Following the similar reasoning as in the horn-to-horn measurement scenario, we

can observe that (24) can be rewritten as

$$|S_{21}^{hl}|^2 = |S_{21}^{h}|^2 |S_{21}^{l}|^2, \tag{27}$$

where S_{21}^{hl} is the de-embedded S_{21} between the horn and the LTSA that has been compensated for path loss and the gains of the two antennas, S_{21}^{h} is the S_{21} of a single horn that was found in the previous section, and S_{21}^{l} is the S_{21} of the LTSA that needs to be calculated. Rearranging (27) for $|S_{21}^{l}|^2$, and employing the relationship between S_{11}^{l} and S_{21}^{l} as in (22), we obtain

$$|S_{11}^{l}| = \sqrt{1 - \frac{|S_{21}^{hl}|^2}{|S_{21}^{h}|^2}}. \tag{28}$$

The measured S_{11} and gain of the LTSA are shown in Fig. 8. They are also compared with the simulated S_{11} and gain of the LTSA to verify our approach. The comparison is further discussed in Section 3.5.

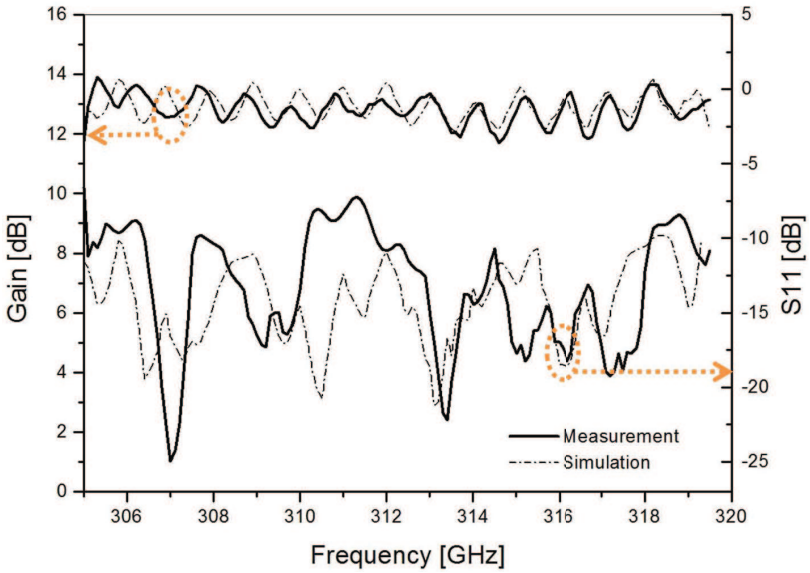

Figure 8: Simulated and measured LTSA gain and S_{11}.

3.5 Comparison Between Simulated and Measured Results

Figures 7 and 8 compare the simulated and measured gain and return loss of the horn and the proposed LTSA, respectively. For the simulated results, the measurement

scenarios described in Section 3.4.1 and 3.4.2 are simulated in CST [102], and the obtained S_{21}'s have been subject to the identical post-processing procedure described in Section 3.4. By replicating the measurement setup in the simulation space, a more fair and comparable results than those obtained from a single, isolated LTSA simulation have been achieved.

In Fig. 7 and 8, it is observed that the measured gain and S_{11} are quite comparable with the simulated ones for both the horn and LTSA. The ripples seen in the measured gain are confirmed by simulation, and it has been found that they are the result of multiple reflections between T_x and R_x hardware. The fabricated LTSA achieves a high gain of around 13 dBi, and below -10 dB S_{11} for most of the measured bandwidth of 305–320 GHz, as observed in Fig. 8. Although the measured results have been plotted for only the upper sideband with additional loss of 5 GHz due to amplifier distortion present in 300–305 GHz, simulation has proven that, in principle, the LTSA has a high gain and low S_{11} below -10 dB across the entire bandwidth of 280–320 GHz as shown in Fig. 2, confirming the wideband (13.3 % fractional bandwidth) characteristic of the proposed antenna. The slight discrepancies observed between measurement and simulation can be attributed to imperfections in fabrication, transitions between the waveguide and antenna, rough surfaces, etc. that would introduce additional losses not accounted in our post-processing algorithm. It can be expected that at such high frequencies, the slightest dimensional irregularity of the structure that is in direct contact with the propagating wave can result in considerable reflections.

3.6 Summary

A broadband linearly-tapered slot antenna with the average gain of 13 dBi across the 280–320 GHz range has been designed, fabricated, and tested. The LTSA has been fabricated using a standard PCB milling machine and the Rogers RT/Duroid

5880 material. To reduce testing cost, pairing of a relatively low-cost 300–320 GHz communication system with a 10 MHz–30 GHz vector network analyzer (VNA) and the use of signal processing has been proposed to extract the gain and return loss of the tested antenna. The results show that the measured average gain and return loss are in good agreement with the simulation results, suggesting that the fabricated LTSA has a high gain and wideband characteristics.

CHAPTER IV

STATISTICAL CHARACTERIZATION OF 300-GHZ PROPAGATION ON A DESKTOP

4.1 Overview

The first measurements and characterization of $300-310$ GHz desktop channels have been reported in [32], where Line-of-Sight free-space propagation as well as diffraction on an edge of a copper plate have been investigated. Also, in [35], the LoS and NLoS indoor measurements obtained from [32] have been compared with ray-tracing simulation with good agreement. While deterministic channel characterization is useful, it requires a priori, site-specific knowledge of the channel environment that cannot be generalized and large simulation time due to the model's adaptation to a new environment. Therefore, from the communications perspective, it is imperative to understand the large- (i.e., path loss, shadowing) and small-scale (i.e., multipath propagation) statistics of the channel that provide easy insight into the channel properties that govern communication at THz frequencies. To the best of author's knowledge, no statistical characterization of 300 GHz channel with 20 GHz of bandwidth has been reported so far.

The contributions of this work are:

1. Devised parameters for the single-slope path loss model with shadowing for LoS environment and analyzed the impact of different materials on path loss when there is no direct line-of-sight present. The results show that the path loss exponent is around 1.9 and the variations due to shadowing are similar across different frequencies and different bandwidths. Additionally, we find that metal objects in the propagation path cause multiple strong reflections leading to

higher path loss.

2. Analyzed the rms delay spread τ_{rms}, the mean excess delay τ_m, the maximum excess delay, the coherence bandwidth and power delay profiles for LoS and NLoS environments. In LoS environment, the mean values of τ_{rms} and τ_m are 428.4 ps and 90.21 ps, respectively, and the variances are 238 ps and 24.56 ps, respectively. The results show that the mean excess delay and rms delay spread increase with distance and that the rms delay spread in a desktop THz channel is much smaller than in typical indoor ultra-wideband channels. From power delay profiles, we have observed that the strong reflections from the transmitter and receiver electronics are present both in LoS and NLoS environments.

3. Performed statistical analysis of the measured signal amplitude in LoS and NLoS environments. For both LoS and NLoS propagation environment, it is found that lognormal distribution provides the best fit.

4. Analyzed the temporal correlation functions for LoS and NLoS environments. The results show that the correlation function drops below 0.2 after 0.15 ns. However, if the strong reflected paths are present in the channel, the correlation function can increase above 0.2 and the signals may get correlated again. This corresponds to the findings in power delay profile where strong reflected paths are present in the channel much after the first path has arrived due to reflections from the transmitter and receiver electronics.

The remainder of the chapter is organized as follows. Section 4.2 describes the measurement equipment, antennas used in the measurements, and the measurement sites. Section 4.3 presents the path loss, shadowing, and multipath propagation analysis of measured data. Finally, Section 4.4 provides some concluding remarks.

4.2 Measurement Setup

4.2.1 Equipment

The equipment and measurement setup used in this chapter is identical to those presented in Section 3.3 (Fig. 3).

By recording the frequency dependent scattering parameter S_{21} for the test signal frequencies $f_{\text{test}} = 10$ MHz $-$ 20 GHz at the VNA, the channel transfer function at $f = 300\text{GHz} + \text{f}_{\text{test}}$ is measured. The maximum allowable input power is 0 dBm (1 mW) which allows for communication at the maximum distances of about 1 m without additional optical lenses. Although propagation loss at terahertz frequencies is significant, high antenna gains would be sufficient to compensate for most of that loss and allow for longer distances. However, the loss in the transceiver is very high and antenna gain barely compensates for the losses in the system. To illustrate the transceiver losses, Fig. 9 shows the transfer function S_{21} of the system when the transmitter (T_x) and the receiver (R_x) are directly connected (without antennas). Since the system calibration could only be performed at the input and the output of the mixers, additional de-embedding is performed by correcting the amplitude of the measured transfer function for the losses in the transceiver.

The full available bandwidth of 19.99 GHz is used in all measurements which provides the spatial and temporal resolution of 1.5 cm or 0.05 ns. The start frequency is bound to a minimum of 10 MHz by the VNA and the stop frequency could not exceed the system limitations of 20 GHz. Due to input power restrictions of the mixers, a test signal with a power of -10 dBm is used, providing a dynamic range of approximately 90 dB for the chosen intermediate frequency filter bandwidth of $\Delta_{IF} = 20$ kHz. The number of sweep points is set to 801, and the maximum excess delay is 40 ns. All measurement parameters are summarized in Table 2.

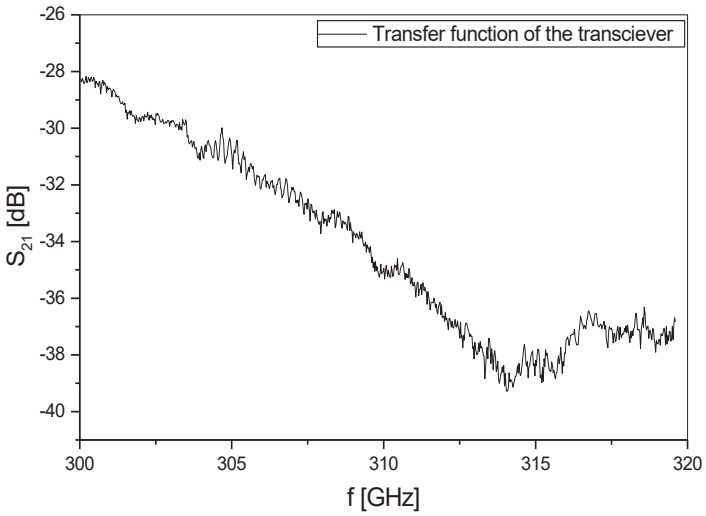

Figure 9: Amplitude response of the 300 GHz measurement system (without antennas).

Table 2: Measurement Parameters.

Parameter	Symbol	Value
Measurement points	N	801
Intermediate frequency bandwidth	Δf_{IF}	20 kHz
Average noise floor	P_N	-100 dBm
Input signal power	P_{in}	-10 dBm
Start frequency	f_{start}	10 MHz
Stop frequency	f_{stop}	20 GHz
Bandwidth	B	19.99 GHz
Time domain resolution	Δt	0.05 ns
Maximum excess delay	τ_m	40 ns

4.2.2 Antenna Characteristics and Site Description

For this measurement campaign, two horn antennas with 26 dBi gain are used. Both antennas are vertically polarized and mounted about 1.5 cm above the ground. The theoretical half power beam-widths (HPBW) are about 10° in azimuth and elevation. The measured return loss of the horn antenna used in the measurements is shown in Fig. 10. We can observe that the antenna has S_{11} lower than -10 dB in the range $300 - 320$ GHz. In the further analysis, the antennas are considered to be part of the

transfer function.

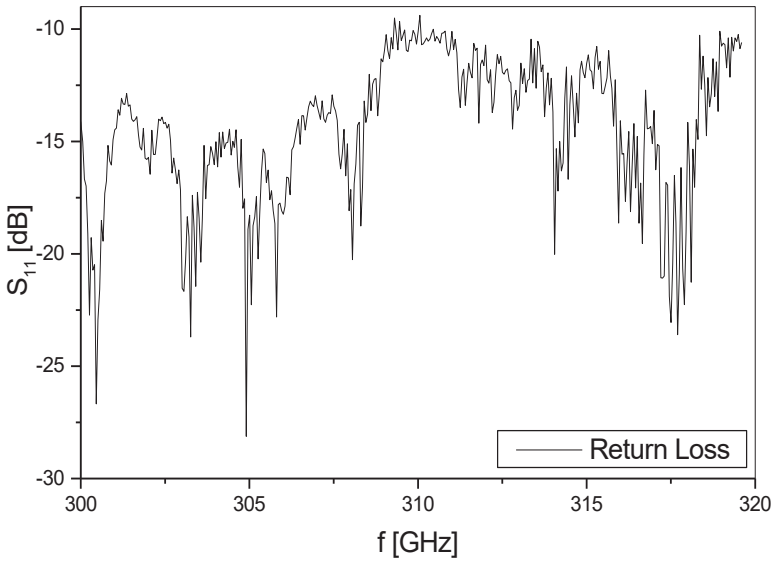

Figure 10: Measured S_{11} of the horn antenna as a function of frequency.

Typical line-of-sight (LoS) communication between devices on a desktop can be expected to operate at distances between 5 cm and 70 cm. Hence, in the first measurement scenario, we have collected channel transfer functions in this range of distances using the measurement setup shown in Fig. 11 (a) at the locations shown in Fig. 11 (b). The module spacing has been varied by moving the R_x and keeping the T_x fixed.

The second measurement scenario tests non-line-of-sight (NLoS) type of communication shown in Fig. 11 (c). The T_x and the R_x are positioned orthogonal to each other (i.e., the T_x antenna is parallel with y-axis and the R_x antenna is parallel with x-axis) with the equal distances from the T_x antenna to the center of the table and from the center of the table to the R_x antenna. These distances were 21.25 cm, i.e., the diagonal distance between the T_x and R_x antennas was $d = 30$ cm. Three types of material, FR4, metal, and plastic are placed at 45° degree between the T_x and the R_x, as shown in Fig. 11 (d). Note that the different materials used as obstacles have 10 cm height and were completely blocking the line-of-sight between the T_x and R_x

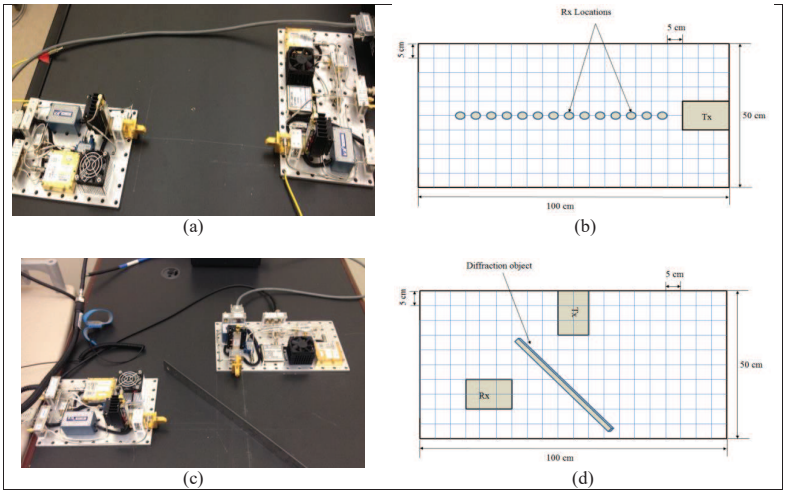

Figure 11: (a) Measurement setup for LoS channel characterization; (b) Measurement setup for NLoS channel characterization.

antennas, so the only possible way for communication is via diffraction or reflection.

The transfer function is recorded before different materials are placed between the T_x and the R_x and the S_{21} was near the noise level indicating that there is not communication between the T_x and the R_x. By using different objects to diffract the signal, communication was successfully established and the next section discusses the obtained results.

4.3 Statistical Characterization of the 300 GHz Channel

Site-specific prediction requires detailed knowledge of the propagation environments. When such information is not available, statistical models can be used to describe general channel properties which are useful for system design or for algorithm testing. Note that statistical characteristics of the measured channel will be dependent on antennas and their locations. This section presents the key statistical parameters extracted from all collected measurements.

4.3.1 Path Loss and Shadowing

We refer to measured path loss, PL, as the transmit power, P_t, multiplied by the transmit and receive antenna gains, G_t and G_r, respectively, and divided by the received power, P_r.

$$PL = \frac{P_t \cdot G_t \cdot G_r}{\bar{P}_r}. \tag{29}$$

The measured path loss is compared with the theoretical free-space path loss, $\tilde{PL}$, calculated with Eq. (21)

The mean of measured path loss, $\overline{PL}$, is obtained by averaging a swept continuous wave over time and frequency, i.e.,

$$\overline{PL(d)} = \frac{1}{MN} \sum_{i=1}^{N} \sum_{j=1}^{M} |H(f_i, t_j, d)|^2, \tag{30}$$

where $H(f_i, t_j, d)$ is the measured complex frequency response data matrix, N is the number of observed frequencies, M is the number of frequency-response snapshots over time, and d is the T-R separation distance in meters.

In the first measurement scenario, LoS communication between devices on a desktop is tested in a measurement setup shown in Fig. 11 (a). In these experiments, the number of observed frequencies was $N = 801$, the number of frequency-response snapshots over time was $M = 10$ (scatter plot in Fig. 14 shows that this is sufficient), and the distances were varied from 5 cm to 70 cm with step of 5 cm.

Figure 12 shows the measured path loss as a function of frequency for several distances between the T_x and the R_x, when the losses in the transceiver are not removed from the measured transfer function. We can observe that the path loss significantly increases with frequency and does not follow the path loss predicted by the Friis equation in (22). The reason for this discrepancy is the frequency dependent transfer function of the transceiver shown in Figure 9. When the additional de-embedding is performed, by correcting the amplitude of the measured transfer function for the

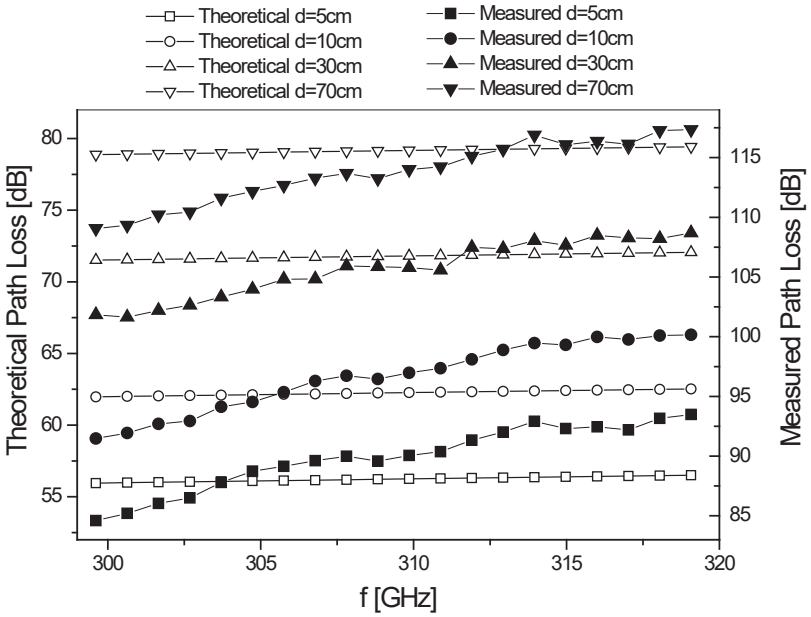

Figure 12: Measured and theoretical path loss as a function of frequency in LoS environment.

losses in the transceiver, better match is observed between the measured and theoretical path loss, as shown in Fig. 13. However, the path loss variation observed across the frequencies indicates that channel equalization across such a wide frequency range is not a straight forward task. In the remaining of the thesis, we will use de-embedded results to capture the true nature of the propagation environment.

Figure 14 shows the scatter plot of the path loss as a function of transmitter-receiver (T-R) separation on a desktop for an LoS environment. We can observe that except for 5 cm distance, the variation between different frequency-response snapshots over time is minimal. This is because there are no temporal or spatial variations nor additional clutter in the channel that would cause significant variations in the measured path loss. The variations in path loss at 5 cm or shorter distances are due to difficulty to achieve very precise alignment between two antennas. Note that this finding is significantly different from typical indoor measurements, where path loss significantly varies around the mean value. This finding leads us to conclude that

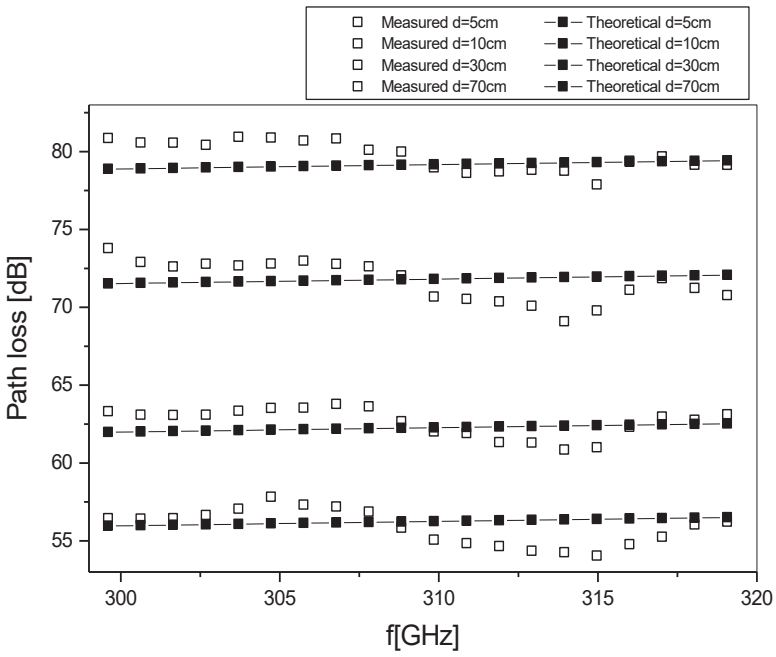

Figure 13: Deembeded measured and theoretical path loss as a function of frequency in LoS environment.

the number of frequency-response snapshots over time does not have to be large and we have found that 10 measurements are sufficient to capture all temporal variations in the signal. However, we still observe some shadowing in our measurements. This is caused by small variations in alignment between the Tx and Rx antenna. While this may not be a traditional shadowing process, it is a random process that causes variations of the received power at a given distance, as shown in Fig. 15.

To estimate the path-loss model parameters γ and σ(dB) in (3), we have performed the least-squares linear regression fitting through the scatter of measured path loss points in decibels such that the root-mean square deviation of path loss points about the regression line is minimized. The model parameters and standard deviations are estimated for the 20 GHz frequency bandwidth, as well as for 2.5 GHz bandwidth starting at $f = \{300, 305, 310, 315\}$ GHz, respectively. The reference distance is $d_0 =$ 1 m and the free-space path loss at the reference distance d_0 is $PL(d_0) = 81.97$ dB. The results are summarized in Table 3 and the fitting of the path loss scatter plot

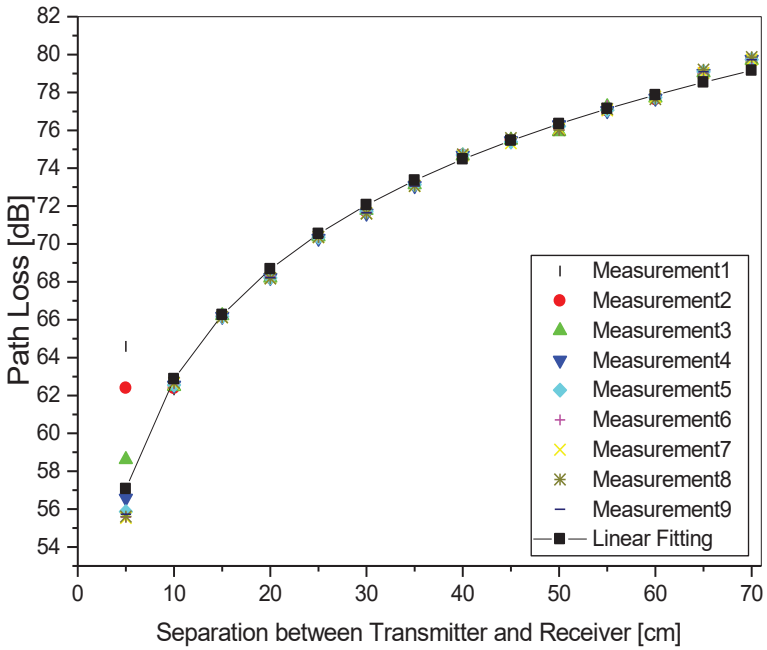

Figure 14: Scatter plot of the path loss versus T-R separation in LoS environment.

is shown in Fig. 14. The results show that the path loss exponent is around 1.9 and the variations due to shadowing are similar across different frequencies and different bandwidths. To confirm that shadowing can be modelled as a zero-mean Gaussian distributed random variable, we have compared the measured distribution of shadow fading with the Gaussian distribution in Fig. 15.

Table 3: Path Loss Parameters.

LoS Propagation				
Frequency [GHz]	Path loss exponent γ	Standard deviation	Variance σ[dB]	Standard deviation
300-320	1.927	0.058	0.67	0.173
300-302.5	1.916	0.045	0.67	0.17
305-307.5	1.886	0.06	0.715	0.185
310-312.5	1.93	0.061	0.737	0.19
315-317.5	1.95	0.056	0.71	0.18

The second measurement scenario assumes NLoS type of propagation. The number of observed frequencies was $N = 801$ and the number of frequency-response snapshots over time was $M = 10$. The T_x and the R_x are positioned orthogonal to each other with the diagonal distance between them set to $d = 30$ cm. FR4, metal, and plastic are placed at 45° degree between the T_x and the R_x, as shown in

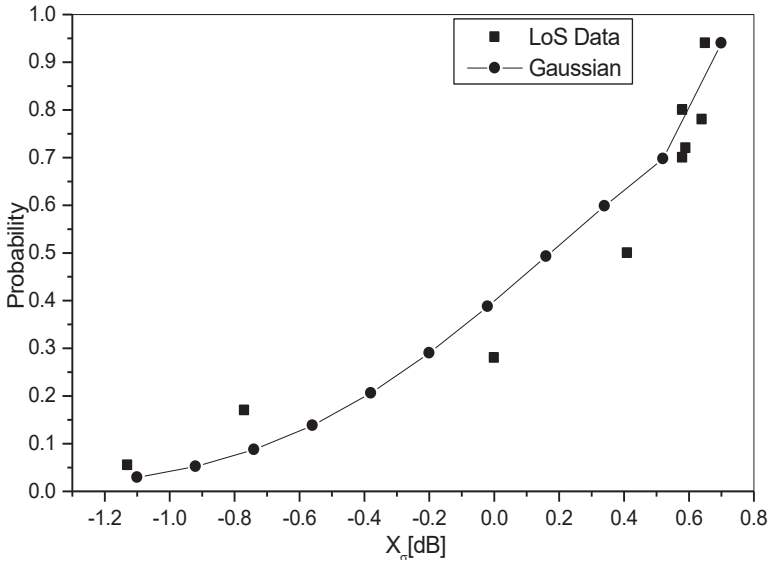

Figure 15: Confirming the log-normality of shadow fading in LoS environment.

Fig. 11 (b). Figure 16 compares the measured path loss as a function of frequency for signals diffracted by FR4, metal, and a plastic material with the theoretical free-space path loss. We can observe that the path loss of signals reflected from FR4 and plastic are oscillating around the theoretical free-space path loss. However, signals reflected from metal have additional 5 dB of loss. We have found that metal objects in the propagation path cause multiple strong reflections which is probably leading to higher path loss.

4.3.2 Multipath Characterization

Multipath propagation is the propagation mechanism manifested when the transmitted signal reaches the receive antenna along two or more paths. Such waves typically arrive at the receiver from many different directions and with different delays, and combine vectorially at the receiver antenna. Such channel impulse response can be characterized as [108]

$$h(t, \tau, d) = \sum_{k=1}^{L} a_k(t, d) \exp(j\theta_k(t, d))\delta(t - \tau_k), \tag{31}$$

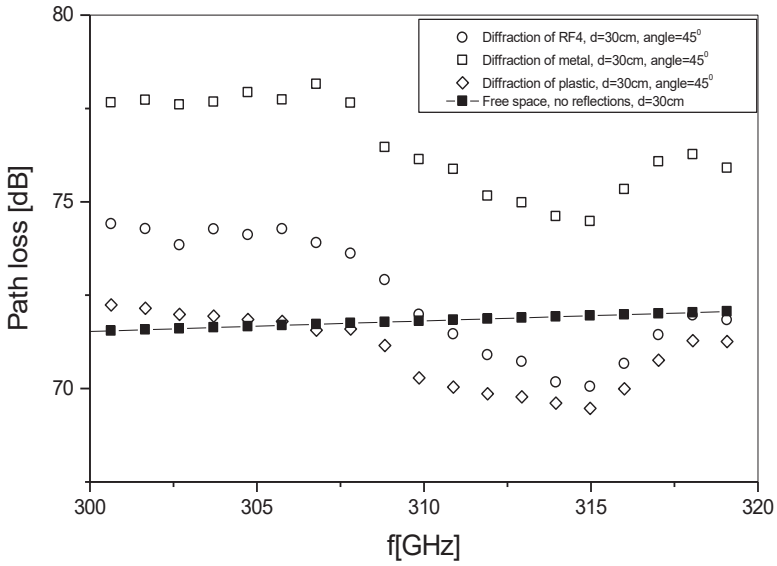

Figure 16: Measured diffracted path loss and theoretical free-space path loss as a function of frequency.

where N is the number of multipath components, a_k represents the amplitude of the k^{th} multipath component, θ_k is the associated phase, and τ_k is the excess delay of the k^{th} path relative to the first arrival, and $\delta(\cdot)$ denotes the Dirac delta function.

An estimate of the channel impulse response is made by taking the inverse discrete Fourier transform (IDFT) of the measured frequency response. The impulse response is then normalized such that the area under the squared magnitude of the power-delay response is equal to one. We refer to a normalized squared magnitude of the impulse response as the multipath intensity profile (MIP) at the single point in space. The noise floor of the MIP is set to 10 dB above the average receiver noise floor. Part of the MIP characterization is based on root mean square (rms) delay spread τ_{rms}, which is a measure of multipath spread within the channel. It is an important parameter for characterizing time dispersion or frequency selectivity. It is the square root of the second central moment of the MIP and is given by [108]

$$\tau_{rms} = \sqrt{\sum_{k=1}^{L}(\tau_k - \tau_m)^2 |h(t, \tau_k, d)|^2}, \tag{32}$$

where τ_m is the mean excess delay (the first moment of the MIP) and is defined as

$$\tau_m = \sum_{k=1}^{L} \tau_k \cdot |h(t, \tau_k, d)|^2. \tag{33}$$

For an LoS environment, Fig. 17 shows that the rms delay spread is normally distributed over all distances. The threshold level in decibels was chosen to be −30 dB from the maximum received power because approximately 99% of the power is captured with this threshold. The mean values of τ_{rms} and τ_m are 428.4 ps and 90.21 ps, respectively, and the variances are 238 ps and 24.56 ps, respectively. Figure 18 shows the path loss versus rms delay spread. The mean τ_{rms} and the mean path loss were obtained by averaging over 10 measured channel impulse responses. Note that similar results are obtained when averaging over 500 measured channel impulse responses. The results indicate an increase in τ_{rms} with increasing path loss. This is an anticipated result, since the paths with longer delays have also larger path loss values associated with them. Finally, the rms delay spread, the mean excess delay, the maximum excess delay, and the coherence bandwidth ($B_c = 1/(2 \cdot \pi \cdot \tau_{\text{rms}})$) are compared for different distances. A summary of these results is given in Table 4. The results show that the mean excess delay and rms delay spread increase with distance as expected. Furthermore, the results show that the rms delay spread in the desktop THz channel is much smaller than in typical indoor ultra-wideband channels. Finally, the results show that the coherence bandwidth significantly reduces with distance. For distances of 5 cm or shorter, the whole 20 GHz bandwidth can be used as a narrowband channel. However, for longer distances, the coherence bandwidth reduces to a couple hundred of megahertz.

For an NLoS environment, the rms delay spread, the mean excess delay, the maximum excess delay, and the coherence bandwidth are compared for different materials. A summary of these results is given in Table 5. Here, the threshold level in decibels was chosen to be −35 dB from the maximum received power. For plastic and FR4, 98.5% of the power was captured with this threshold, while for metal, 96.9% of the

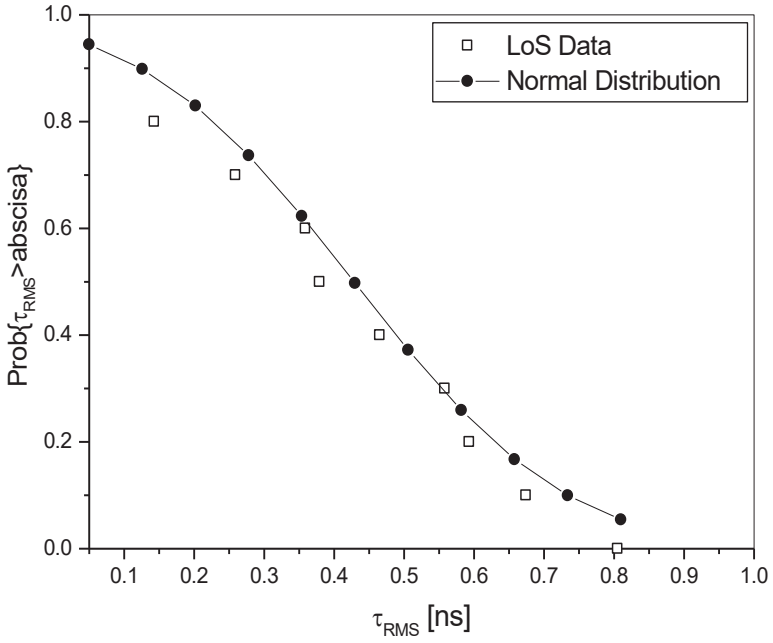

Figure 17: Cumulative distribution function of rms delay spread in LoS environment.

Table 4: Mean Excess Delay, RMS Delay Spread, Maximum Excess Delay, and Coherence Bandwidth for Different T-R Spacings.

Distance [cm]	τ_m [ps]	τ_{rms} [ps]	$\tau_{\max}$ [ns]	B_c [GHz]
5	50.76	4.35	0.1	36.6
15	63.73	127.79	1.45	1.24
25	74.61	215.05	2.15	0.74
35	100.44	326.01	2.75	0.488
45	123.05	365.69	3.9	0.435
55	158.39	424.15	4.2	0.375
65	176.46	484.94	4.65	0.328

power was captured with this threshold. The results show that diffraction of metal has slightly higher coherence bandwidth than diffraction of FR4 and plastic. Furthermore, we can observe that the mean excess delay, the maximum excess delay, and the coherence bandwidth for these three materials is comparable with those of LoS propagation with the T-R spacing of 25 cm – 30 cm.

Here, we also calculate the power delay profile (PDP) by averaging the magnitude squared of the channel impulse response over the number of frequency-response

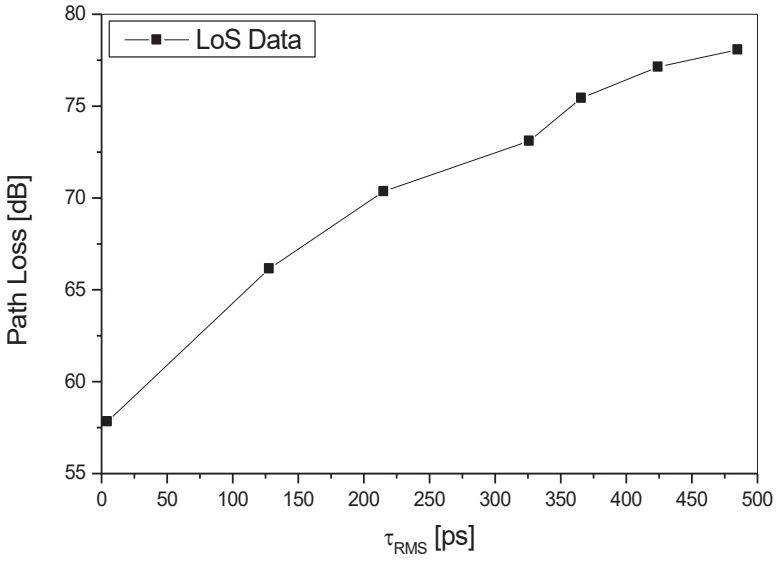

Figure 18: Path loss versus rms delay spread in LoS environment.

Table 5: Mean Excess Delay, and RMS Delay Spread for Different Diffraction Materials.

Material	τ_m [ps]	τ_{rms} [ps]	$\tau_{\max}$ [ns]	B_c [GHz]
FR4	70.53	210	2.65	0.757
Metal	67.07	187	2.5	0.85
Plastic	77.54	227	3.05	0.701

snapshots

$$P(\tau) = \frac{1}{M} \sum_{k=1}^{M} |h(t_k, \tau, d)|^2, \tag{34}$$

where t_k is the fixed observation instant of the k^{th} frequency-response snapshots and M is the total number of frequency-response snapshots.

For an LoS propagation environment, power delay profiles for distances $d = \{10,$ 15, 20, 40, 70 cm$\}$ between the T_x and the R_x are shown in Fig. 19. The significant part of the PDP is determined by discarding all parts that are more than 35 dB down from the strongest path, because approximately 99.5% of the power is captured with this threshold. The results show that in addition to the direct path, there is an additional strong reflection component. From the time of arrival, we can conclude that

this reflection is from the signal that was once reflected from the R_x electronics, then reflected from the T_x electronics and then received at the R_x. This conclusion is also verified experimentally by putting absorbers around the T_x and R_x antennas, blocking the paths toward the electronics. We have observed that the strong reflections would disappear from the power delay profile. This is an interesting observation that opens up the question of putting the absorbers around the antennas. We choose not to use the absorbers, because in practice, even if we manage to perfectly shield the T_x and R_x electronics, there might be objects in the vicinity or behind the T_x or R_x that can create similar propagation effects. This result also explains somewhat large rms delay spreads in Table 4.

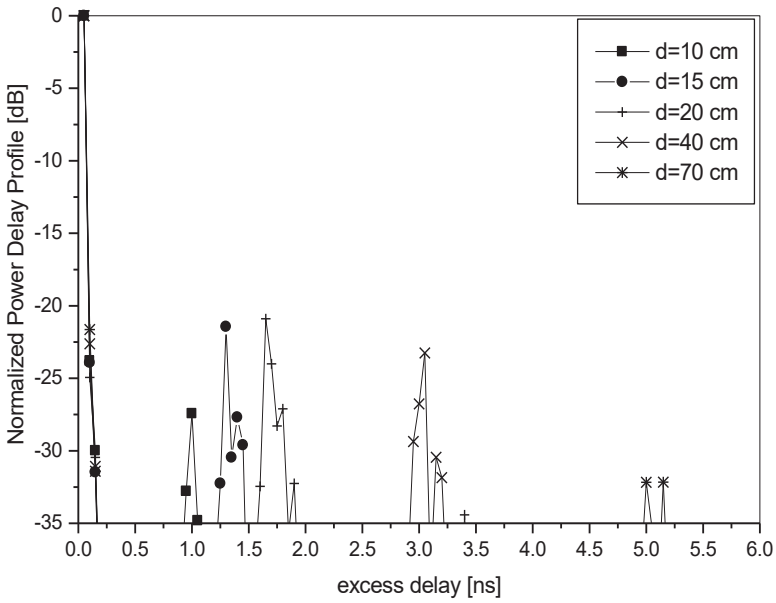

Figure 19: Normalized power delay profile in LoS propagation environment.

For an NLoS propagation environment, Figure 20 compares the normalized power delay profile of signals diffracted from FR4, metal, and plastic. The diagonal separation between the T_x and R_x antennas was 30 cm. The results show that there is a diffracted path, and somewhat surprisingly, there are several strong reflected paths. By examining the time of arrival, we have found that these reflections are multiple reflections from the R_x and T_x electronics. Furthermore, we can observe that

diffractions and reflections from metal have stronger multipath components and keep arriving with power higher than −40 dB for more than 7ns. This indicates that if rich multipath is present in the channel, there will be large number of paths arriving with significant amount of energy which would require sophisticated channel equalization schemes.

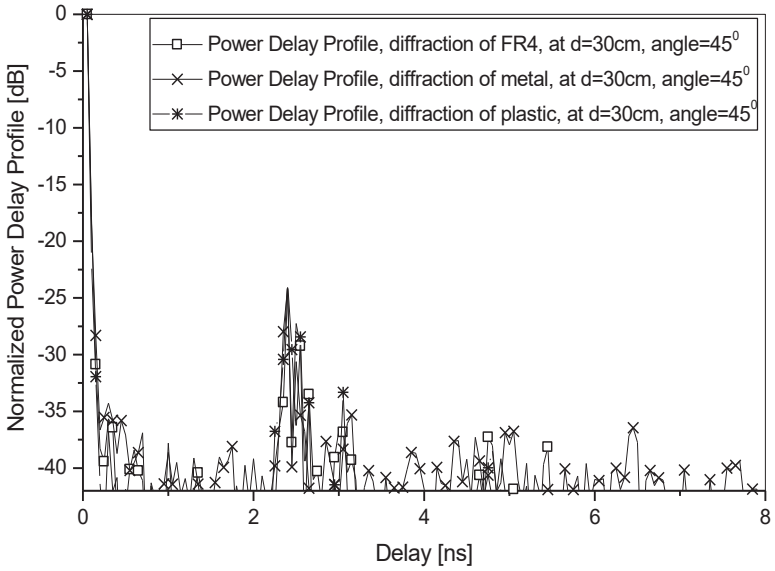

Figure 20: Normalized power delay profile in NLOS propagation environment.

To test the statistical behavior of measured channel amplitudes, the amplitude of each channel impulse response bin is fitted into several different distributions using the best fit procedure. It was difficult to visually make a conclusion as to which distribution is the best fit, so our conclusions are based on the maximum log-likelihood test and sum of squares due to errors (SSE) test. Five distributions are used to fit the measured data, including Gaussian, lognormal, Nakagami, Ricean, and Weibull distributions. For the LoS measurement scenario, we have tested statistical properties of the amplitude at distances ranging from 5 cm to 70 cm. For all tested amplitudes, the closest fit is observed between the measured data and a lognormal distribution. To illustrate these results, Figure 21 compares the inverse cumulative distribution function (i.e., quantile plot) of the measured received amplitude of the first bin at the

distance $d = 70$ cm with the inverse cumulative distributions of the Gaussian, lognormal, Ricean, Nakagami, and Weibull distributions. The results in Fig. 21 show that the best fit is between the measured amplitude and the lognormal distribution, which is further verified by having the highest log-likelihood. Similar statistical analysis is performed for the NLoS type of propagation where the distance between the T_x and the R_x was 30 cm. Similarly, the best fit is observed between the measured data and the lognormal distribution.

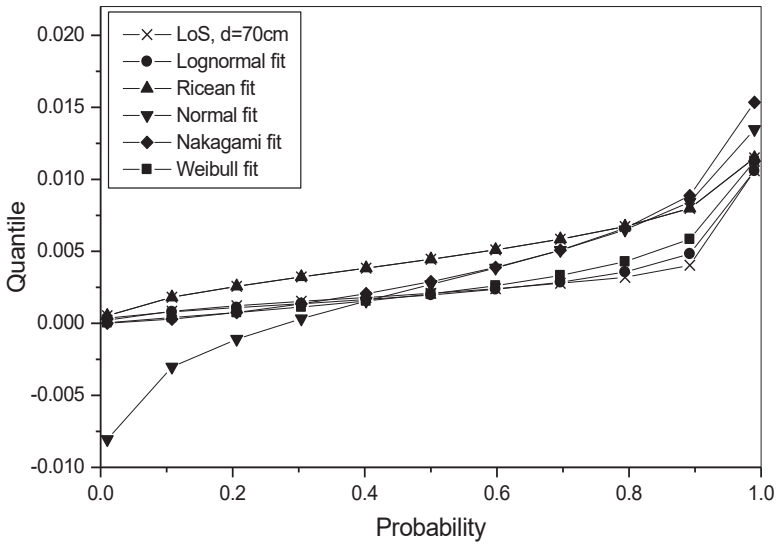

Figure 21: Theoretical and empirical inverse cumulative distribution functions of $a_1(t, d)$ in LoS propagation environment.

Finally, we also analyze the temporal correlation function in the LoS and NLoS propagation environments. The normalized temporal correlation function is calculated as

$$R(\tau) = \frac{\mathrm{E}\left[h(t)h(t+\tau)^*\right]}{\sqrt{\mathrm{E}[|h(t)|^2]\mathrm{E}[|h(t)|^2]}}, \tag{35}$$

where $(\cdot)^*$ denotes the complex conjugate operation and $\mathrm{E}[\cdot]$ is the statistical expectation operator.

Figure 22 shows the temporal correlation function in an LoS environment for

distances $d = \{5, 10, 40\}$ cm between the T_x and the R_x. The results show that correlation function drops below 0.2 after 0.15 ns for all tested distances. Figure 23 shows

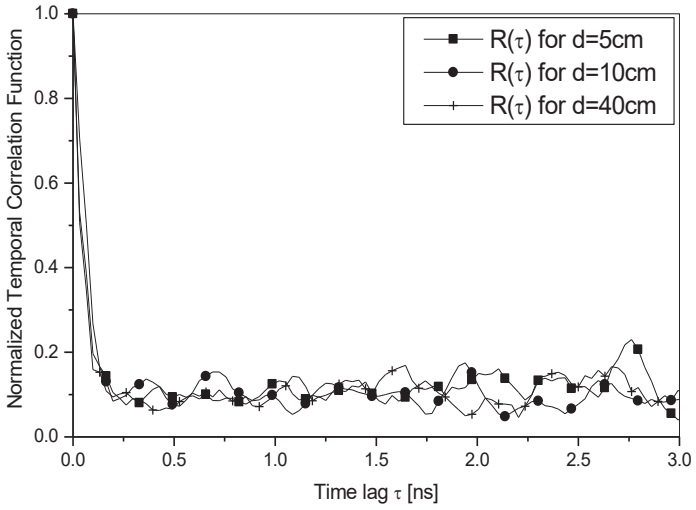

Figure 22: Normalized temporal correlation function in LOS propagation environment.

the temporal correlation function in the NLoS environment where signals are reflected of FR4, plastic and metal. The results show that similar to the LoS environment, the correlation function drops below 0.2 after 0.15 ns. However, if the strong reflected paths are present in the channel, the correlation function can increase above 0.2 and the signals may get correlated again. This corresponds to the findings in power delay profile where strong reflected paths are present in the channel much after the first path has arrived.

4.4 Summary

This chapter presented measurements and statistical characterization of 300 – 320 GHz desktop channels. The measurements were performed in LoS and NLoS environments. From the large set of LoS measured data, the parameters for single-slope path loss model with shadowing were devised. The results show that the path loss exponent is

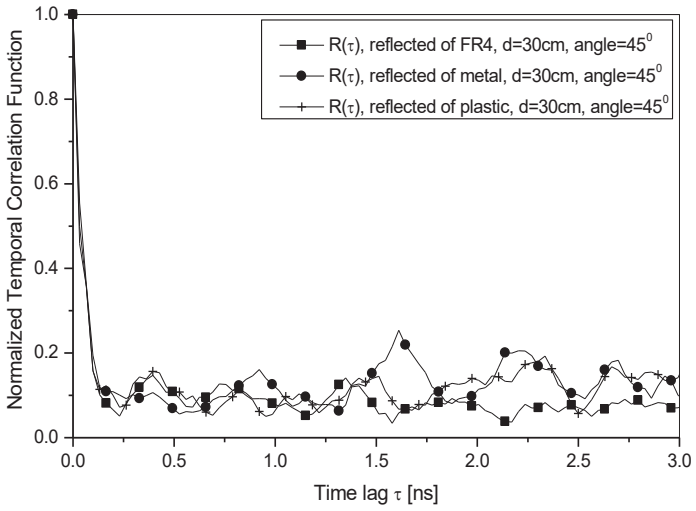

Figure 23: Normalized temporal correlation function in NLOS propagation environment.

around 1.9 and the variations due to shadowing are similar across different frequencies and different bandwidths. Furthermore, the impact of different materials on the path loss is studied in an NLoS environment. We have found that metal objects in the propagation path cause multiple strong reflections leading to higher path loss. Furthermore, the statistical analysis of multipath propagation is performed. We have calculated the rms delay spread, the mean excess delay, the maximum excess delay, and the coherence bandwidth for LoS and NLoS environments. The results show that the mean excess delay and rms delay spread increase with distance and that the rms delay spread in desktop THz channel is much smaller than in typical indoor ultra-wideband channels. In addition, the power delay profiles for LoS and NLoS environments are analyzed. We have found strong reflections from the transmitter and receiver electronics present both in LoS and NLoS environments. Finally, the statistical analysis of the measured signal amplitude in LoS and NLoS environments is performed. For both LoS and NLoS propagation environments, it is found that a lognormal distribution provides the best fit.

CHAPTER V

D-BAND CHANNEL MEASUREMENTS AND CHARACTERIZATION FOR INDOOR APPLICATIONS

5.1 Overview

While 60 GHz communications have limited bandwidth, 300 GHz channels are limited in range. As an alternative, the 60 GHz of spectrum between 110 GHz and 170 GHz, or the D-band frequencies, offers sufficient bandwidth and range required for ultra-fast and ultra-wideband data transmissions [110]. This frequency band is currently unregulated, and is typically used for atmospheric applications. However, its large bandwidth paired with high-speed wireless links also has the potential for precision positioning and velocity sensors [111], passive mm-wave cameras [112], and short- and medium-range Tbps wireless links. While D-band has been extensively used for microwave atmospheric sounding (e.g., [36]), to the best of the author's knowledge, no indoor D-band channel characterization based on measurements has been reported in the open literature. Although channel characterization at 120 GHz for an indoor office scenario has been reported in [37], this work only presents ray-tracing simulation results, where reflection is considered as the sole propagation mechanism, and the results are presented for a single frequency in D-band. While atmospheric absorption is the main focus of microwave atmospheric sounding, this loss plays a minor role in indoor propagation. Reflections, diffraction, and scattering are more prevalent propagation mechanisms in indoor D-band channels.

For a more complete characterization of D-band channels, characterization of path loss and multipath parameters in the entire spectrum of 60 GHz in LoS, Obstructed-Line-of-Sight (OLoS), and Reflected Non-Line-of-Sight (RNLoS) environments have

been performed. Furthermore, diffraction of D-band waves when obstructed by common objects of cylindrical shape (e.g., glasses, mugs) has been modelled with the Uniform Geometrical Theory of Diffraction (UTD) in desktop OLoS environments.

The remainder of this chapter is organized as follows: Section 5.2 describes the measurement equipment, antennas used in the measurements, and the measurement setup. Section 6.3.1 presents the path loss, shadowing, and multipath propagation analysis of LoS measured data. Section 5.4 presents the path loss, shadowing, and multipath propagation analysis of OLoS measured data, while Section 5.5 presents the path loss and multipath propagation analysis of RNLoS measured data. Section 5.6 shows UTD modelling of diffraction loss caused by the cylinder obstruction in OLoS scenarios, and finally, Section 5.7 provides some concluding remarks.

5.2 Measurement Setup

5.2.1 Equipment

The block diagram of the D-band measurement setup is shown in Fig. 24. The Agilent

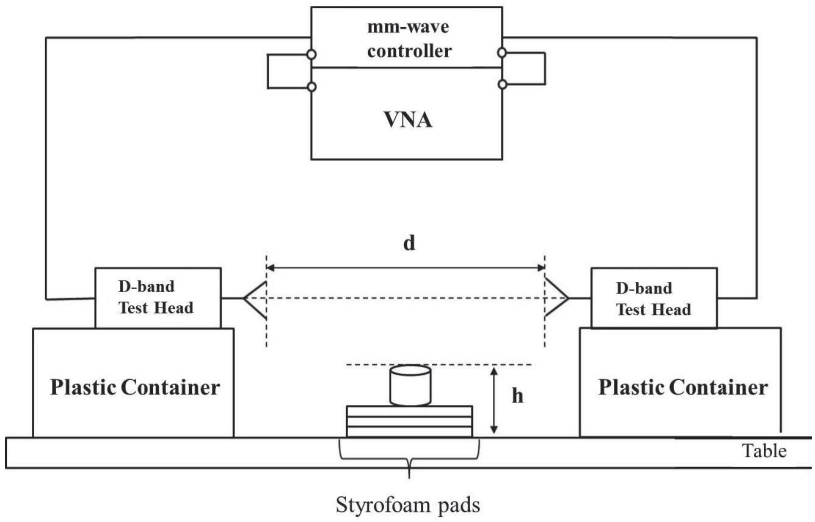

Figure 24: The 110–170 GHz measurement setup.

E8361C vector network analyzer is used for all measurements. The E8361C has a frequency range up to 67 GHz, therefore the N5260A (mm-Wave Controller) and OML

V06VNA2 (mm-Wave Test Head modules) are used to extend the range to the D-band (110 GHz–170 GHz). The N5260A mm-wave controller provides radio frequency (RF) and local oscillator (LO) signals to the mm-wave test head modules and returns the down-converted reference and test IF signals to the VNA for process and display. The OML V06VNA2 frequency extension module has an LO multiplication factor of 10, which up-converts the input LO frequency from 11 to 17 GHz, supplied by the mm-wave controller, to the D-band (110 to 170 GHz).

The full available bandwidth of 60 GHz is used in all measurements which provides the spatial and temporal resolution of 5 mm or 0.0167 ns. Due to input power restrictions of the mixers, a test signal with a power of 0 dBm is used, providing a dynamic range of approximately 90 dB for the chosen intermediate frequency filter bandwidth of $\Delta_{IF} = 100$ Hz. The number of sweep points is set to 801, and the maximum excess delay is 13 ns. All measurement parameters are summarized in Table 6.

Table 6: Measurement parameters.

Parameter	Symbol	Value
Measurement points	N	801
Intermediate frequency bandwidth	Δf_{IF}	100 Hz
Average noise floor	P_N	-85 dBm
Input signal power	P_{in}	0 dBm
Start frequency	f_{start}	110 GHz
Stop frequency	f_{stop}	170 GHz
Bandwidth	B	60 GHz
Time domain resolution	Δt	0.0167 ns
Maximum excess delay	τ_m	13 ns

5.2.2 Antenna Characteristics

The antenna used in the measurement is a pyramidal horn with gain that varies from 22 to 23 dBi from 110 GHz to 170 GHz, respectively. Both T_x and R_x antennas are vertically polarized and have theoretical half-power beamwidths (HPBW) of 12° and

13.5° in E-plane and H-plane, respectively, at 110 GHz. The E-plane and H-plane

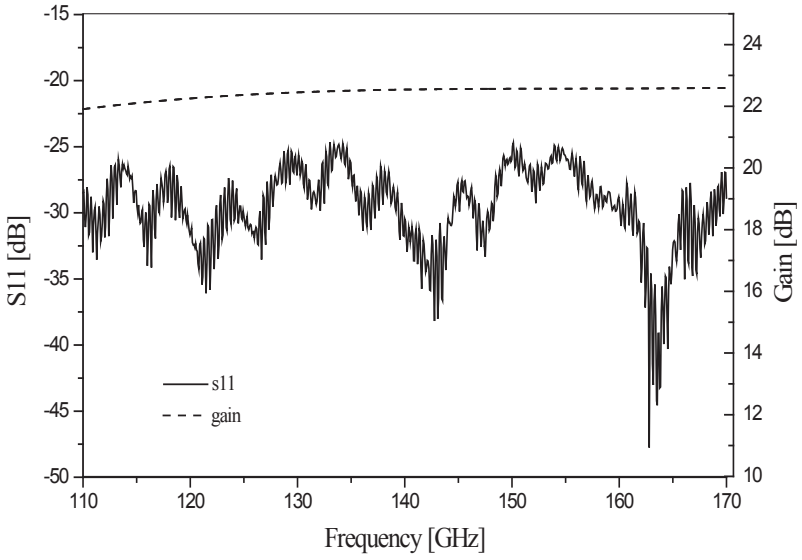

Figure 25: Reflection coefficient and gain of the horn antenna used in measurements.

beamwidths also decrease to 9° and 12°, respectively, towards higher frequencies. Furthermore, antennas have side-lobes that are at least 25 dB below the main beam and all possible reflectors on the sides of the channel have been covered with absorbers as shown in Fig. 26, to ensure that any paths resulting from the side-lobes are suppressed. The measured S_{11} and the frequency-dependent gain of the horn antenna are presented in Fig. 25. Note that the return loss shown here includes the reflections at the interfaces between cable and test head as well as test head and the antenna due to mismatches between them. Nevertheless, we can observe that the S_{11} is below -25 dB across the entire bandwidth. In further analysis, antennas are considered to be part of the channel impulse response, which is typically the case in wireless communication applications.

5.2.3 Measurement Scenarios

In this measurement campaign, three different scenarios have been considered: the LoS scenario shown in Fig. 26(a), an OLoS scenario shown in Fig. 26(b), and a Reflected NLoS scenario shown in Fig. 26(c).

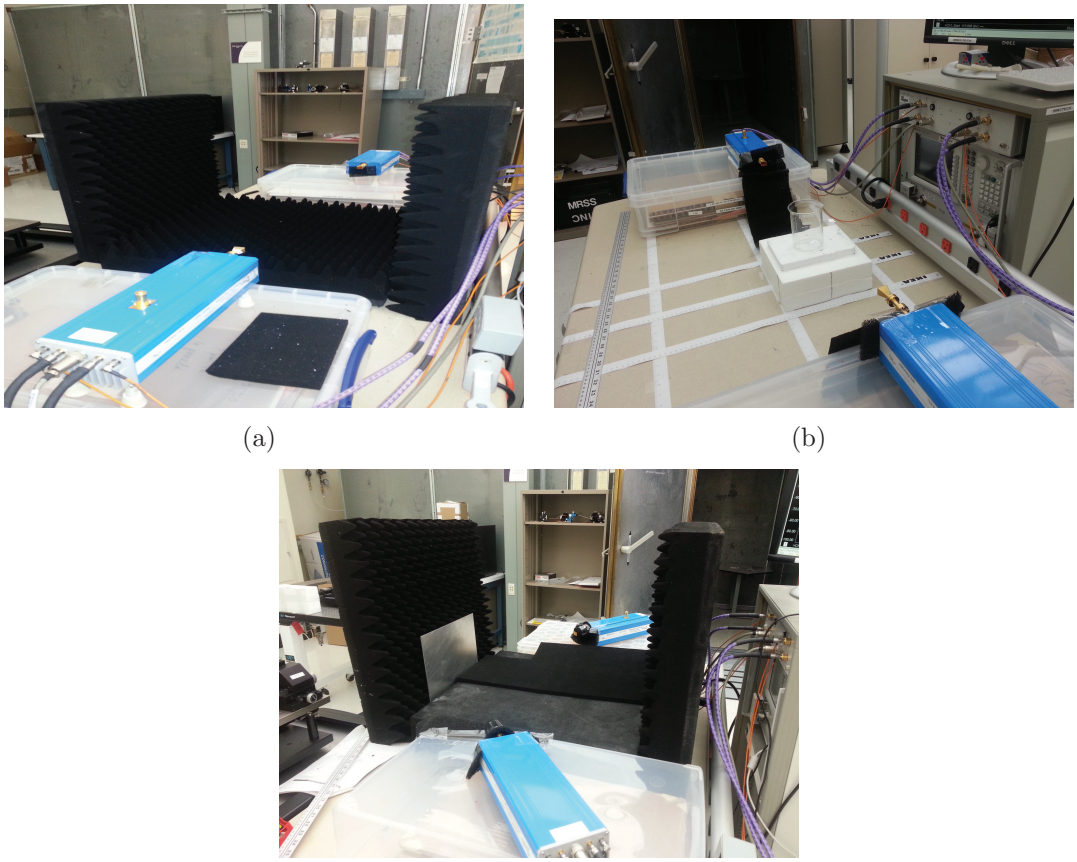

(a) (b)

(c)

Figure 26: Photographs of measurement scenarios: (a) LoS; (b) OLoS, glass as obstruction; (c) Reflected NLoS, aluminum plate as reflector.

Considering the short-range of D-band applications, the T_x-R_x separation distance, d, shown in Fig. 24, has been varied from 35.56 cm (14") to 86.36 cm (34") in 5.08 cm (2") increments, giving a total of 11 different distances for LoS scenario. Furthermore, to mitigate the reflections from the ground and the metallic transceiver cases, the T_x and R_x test heads have been placed on top of a supporting plastic container, and all possible reflecting surfaces, including the ground, the equipment rack cabinet, and the front faces of the test heads, have been covered with absorbers as shown in Fig. 26(a). For the OLoS scenario, obstructions of circular cylinder shape, i.e., cups, have been used as typical objects present on desk tops. To study the impact of different materials on propagation in D-band, three different types of material, i.e., glass, plastic (Polystyrene), and ceramic have been considered. The same 11 T_x-R_x separations as in the LoS scenario have been used for the OLoS scenario. Each obstruction is placed such that the cylinder's center coincides with the midpoint of the separation distance, and its top edge is 3.5 cm above the LoS path. Furthermore, to investigate the effect of obstruction height on path loss, we have varied the positions of the top rim of the cylinders, or h in Fig. 24, from 14.3 cm to 21.9 cm. The obstruction height has been varied by having a different number of Styrofoam pads (which have been tested to cause minimal reflections at the frequencies of interest) underneath the cylinder obstruction, as shown in Fig. 24. Note that the centers of the horn antennas are located 20.6 cm above the table. Finally, in the reflected NLoS scenario, we use reflection as the main mechanism of wave propagation. Two types of reflecting surfaces, aluminum plate and fiberboard, having different reflectivity and surface roughness, have been used. Furthermore, by varying the angular position of the R_x, while keeping the T_x position fixed, the range of R_x angular offsets at which the receiver can detect the reflected signal is studied. For RNLoS, the LoS separation distance was fixed to 76.2 cm.

5.3 Characterization of D-band LoS Channel

5.3.1 LoS Path Loss and Shadowing

Figure 27 compares the measured path loss with the theoretical path loss calculated using Eq. (21). We plot only five out of 11 separation distances to avoid clutter. We can observe that the measured path loss curves very closely follow the theoretical lines. The oscillations observed in the path loss curves have been found to be a result of multiple reflections between the front faces of the T_x and R_x test heads. Although they were covered with a layer of absorbing material, as shown in Fig. 26(a), it was apparently not thick enough to completely mitigate the reflections. This resulted in the constructive and destructive interference between the direct and reflected rays, which led to the oscillation in the measured S_{21}.

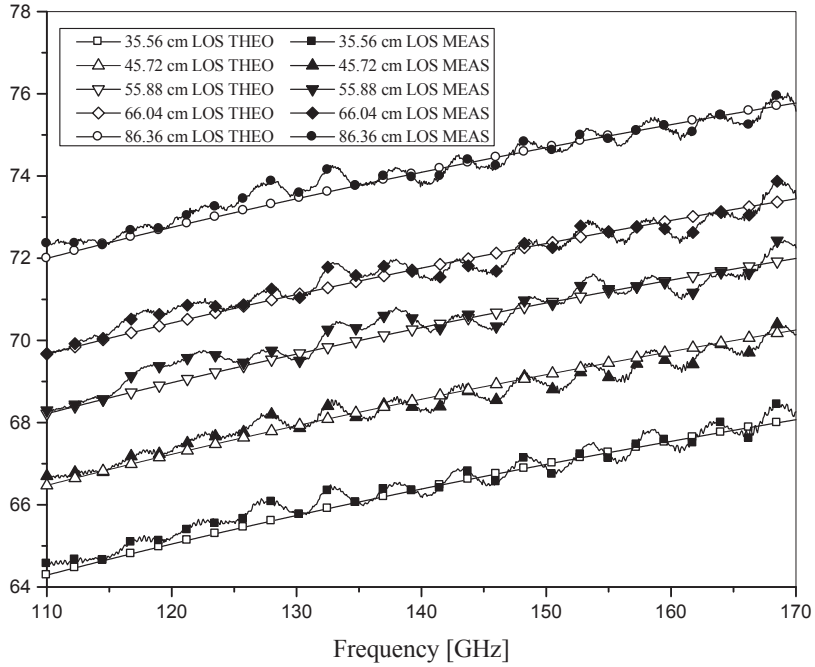

Figure 27: Measured and theoretical path loss for 5 separation distances.

Figure 28 shows the scatter plot of the mean path loss as a function of transmitter-receiver (T-R) separation on a desktop for a LoS environment. We can observe that the variation between different frequency-response snapshots over time is minimal. This is because there are no temporal or spatial variations nor additional clutter in the

channel that would cause significant variations in the measured path loss. Note that this finding is significantly different from typical indoor measurements, where path loss significantly varies around the mean value. This finding leads us to conclude that the number of frequency-response snapshots over time does not have to be large and we have found that 10 measurements are sufficient to capture all temporal variations in the signal.

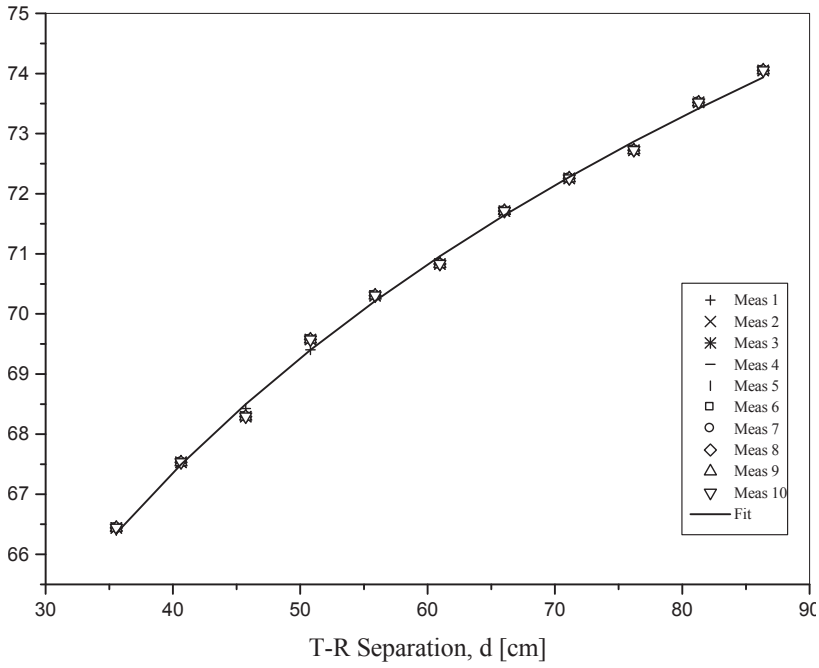

Figure 28: The scatter plot of the LoS path loss.

The path loss exponent obtained from the measured results is around 1.97 and the variations due to shadowing are around $\sigma = 0.12$ dB. The reference distance is $d_0 =$ 1 m and the free-space path loss at the reference distance d_0 is $PL(d_0) = 75.19$ dB. To confirm that shadowing can be modelled as a zero-mean Gaussian distributed random variable, Fig. 29 compares the measured distribution of shadow fading with the Gaussian distribution. This shadowing is due to misalignment between the T_x and R_x antennas. While this may not be a conventional shadowing process, it is still a random process that causes variations of received power at a given distance.

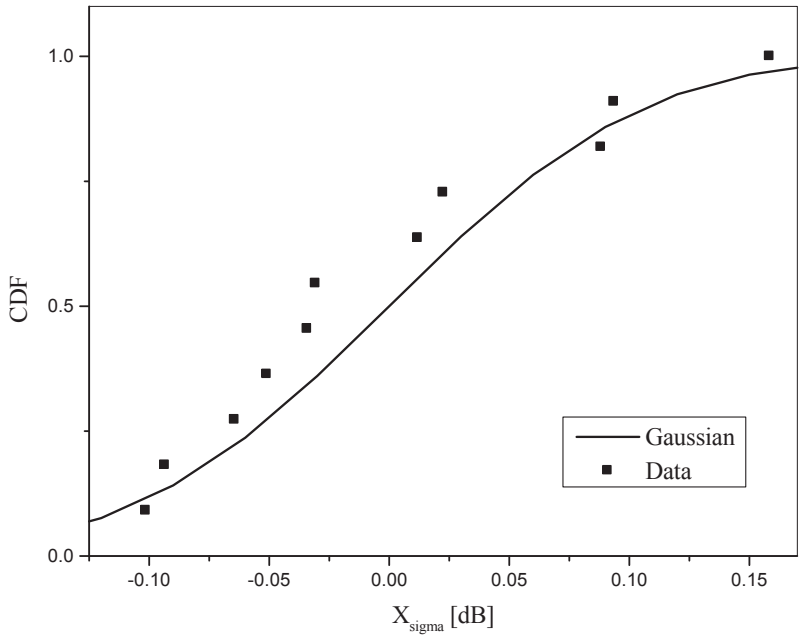

Figure 29: Confirming the log-normality of the shadow fading caused by variations in T-R alignment in LoS environment.

5.3.2 LoS Multipath Characterization

The rms delay spread, found with Eq. (4.3.2), mean excess delay, and the coherence bandwidth ($B_c = 1/(2 \cdot \pi \cdot \tau_{rms})$) for three separation distances with and without the absorbers are presented in Table 7. It is observed that the coherence bandwidths have almost doubled, or even tripled, when the absorbers are in place.

Table 7: Mean excess delay, RMS delay spread, and coherence bandwidth for different T-R separation distances.

d [cm]	Without Absorbers			With Absorbers		
	τ_m [ps]	τ_{rms} [ps]	B_c [GHz]	τ_m [ps]	τ_{rms} [ps]	B_c [GHz]
35.56	17.18	32.12	4.95	16.92	12.00	13.26
55.88	17.08	30.50	5.22	16.95	12.84	12.40
76.2	17.04	31.28	5.09	16.87	10.03	15.87

For the distance of 35.56 cm, the delay spread, τ_{rms}, is expected to be lower, or equivalently, the coherence bandwidth is expected to be higher than that of the 76.20 cm, but the opposite is observed in Table 7. This is because the distance of

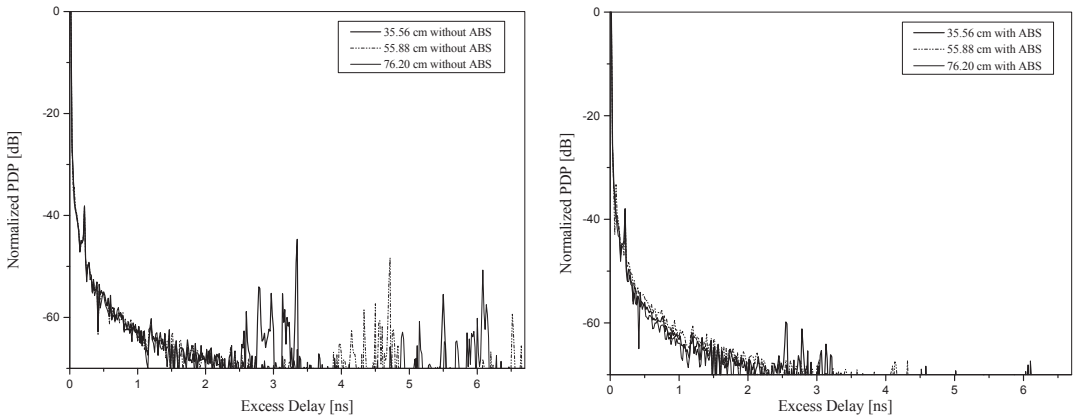

(a) (b)

Figure 30: Normalized power delay profiles for the 3 separation distances (a) *without* and (b) *with* absorbers.

35.56 cm is short enough for the second reflected path to be captured within the maximum excess delay of 6.67 ns. This detection of an extra reflected signal results in the increase in the delay spread, which leads to the decrease in the coherence bandwidth. When the absorbers are used to cover the T_x/R_x test head's front face, we can observe that, while the reflections are almost completely removed for 76.20 cm, there are still some weak reflections observed for 35.56 cm. This has again resulted in a slightly narrower coherence bandwidth for 35.56 cm then that for 76.20 cm. The power delay profiles (PDP) of the 3 separation distances in LoS environment with and without the absorbers that cover the T_x and R_x test heads are shown in Figs. 30(a) and 30(b). Note that all PDP's are normalized, and referenced to the path supporting the first incoming signal. We can observe that the later arriving signals caused by reflections off the metallic test head cases can be attenuated using the absorbers. It is also observed that the reflected paths have increasing excess delay, more delay spread, and decreasing signal power with increasing T-R separation as they travel further distances with more power spreading. In summary, the unwanted reflections from the transceiver electronics will have a profound impact on the channel, and attenuating these reflected signals below certain threshold could be an important

issue when building the transceiver systems.

5.4 Characterization of D-band OLoS Channel

5.4.1 OLoS Path Loss and Shadowing

The obstructed line-of-sight (OLoS) environment is created by placing a glass beaker, a plastic cup, and a ceramic mug in the midpoint of the separation distance, with its top edge 3.5 cm above the LoS path. The measured path losses for these three scenarios and three different separation distances are presented in Figs. 31(a), 31(c), 31(e), respectively. The measured results are compared with the free-space theoretical path loss obtained using Eq. (20). The plots show that the measured path loss is much higher than the free-space path loss, which is an expected result since the OLoS has higher losses due to obstructions in LoS. Furthermore, we can observe that the plastic cup introduces the least amount of attenuation compared to free-space path loss and that the variation of path loss across frequencies is minimal. The glass beaker introduces higher attenuation and as the distance increases, the path loss variations as the function of frequency become more pronounced. Finally, the ceramic mug introduces the highest attenuation and the path loss variations as the function of frequency become dominant. We can observe that ceramic material introduces similar attenuation as a glass at lower frequencies, i.e., 110 GHz − 130 GHz, but then the loss increases to over 100 dB in the range of 140 GHz − 160 GHz. We can also observe that the maximum of the path loss changes with the separation between the T_x and R_x.

Figures 31(b), 31(d), and 31(f) show the scatter plot of the path loss as a function of transmitter-receiver (T-R) separation for glass, plastic, and ceramic OLoS environments, respectively. All 11 distances are used for the scatter plot to obtain the best linear regression fit. As in the LoS case, there are minimal discrepancies among 10 consecutive measurements because the channel is quasi-static with no moving objects in the environment.

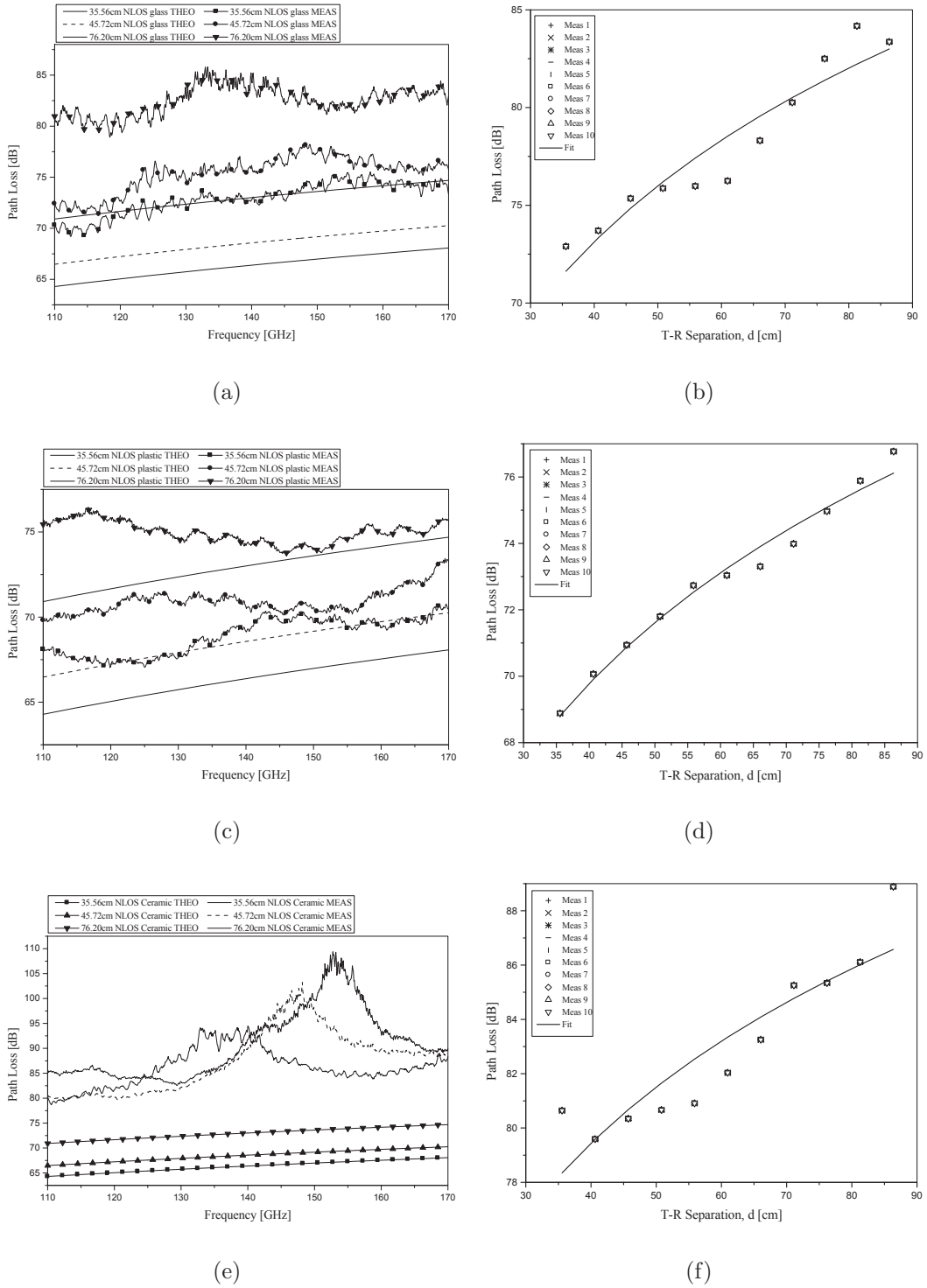

Figure 31: Measured path losses in OLoS environment as a function of frequency (left column) and of distance (right column), where the obstructions are (a),(b) a glass beaker, (c),(d) a plastic cup, and (e),(f) a ceramic mug.

Table 8: The Log-Distance Path Loss Model Parameters.

	OLOS		
	Glass Beaker	Plastic Cup	Ceramic Mug
Path Loss Exponent, γ	2.9519	1.8964	2.1356
Std. Deviation, σ	1.3418 dB	0.3757 dB	1.3746 dB
Path Loss at d_0=1m, PL_0	84.88 dB	77.32 dB	87.94 dB

To estimate the path-loss model parameters γ and σ(dB) in Eq. (3), we have performed a least-squares linear regression fitting through the scatter of measured path loss points and the results are shown in Figs. 31(b), 31(d), and 31(f) for glass, plastic, and ceramic, respectively. The path loss exponents (γ), standard deviations (σ), and the path losses at reference distance, 1 m, (PL_0) for all three obstruction materials are summarized in Table 8. We can observe that the path loss exponent for the plastic cup is the closest to the LoS path loss exponent value of 1.96, which is not surprising since plastic is very transparent at D-band frequencies. For glass and ceramic, due to the considerable blockage of the LoS path, the path loss exponents have increased above the free-space value of 2. In OLoS scenarios, shadow fading becomes more dominant because of the presence of obstructions. To confirm that shadowing can be modelled as a zero-mean Gaussian distributed random variable, we have compared the measured distribution of shadow fading with the Gaussian distribution in Fig. 32. Table 8 shows that standard deviation around the mean path loss is the smallest with the plastic obstruction and similar (but much higher) for glass and ceramic obstructions.

Figure 33 shows the variation in OLoS path loss with varying height of the obstruction, while the T-R separation is fixed at 86.36 cm. As described in Section 5.2.3, the LoS is 20.6 cm above the table, while h is varied from 14.3 cm to 21.9 cm. In Fig. 33, we can see that the path loss closely follows the theoretical free-space path loss curve when the LoS path is clear of obstruction, which corresponds to $h = 14.3$ cm in the figure. One interesting observation here is that the path loss curve for $h = 18$ cm is

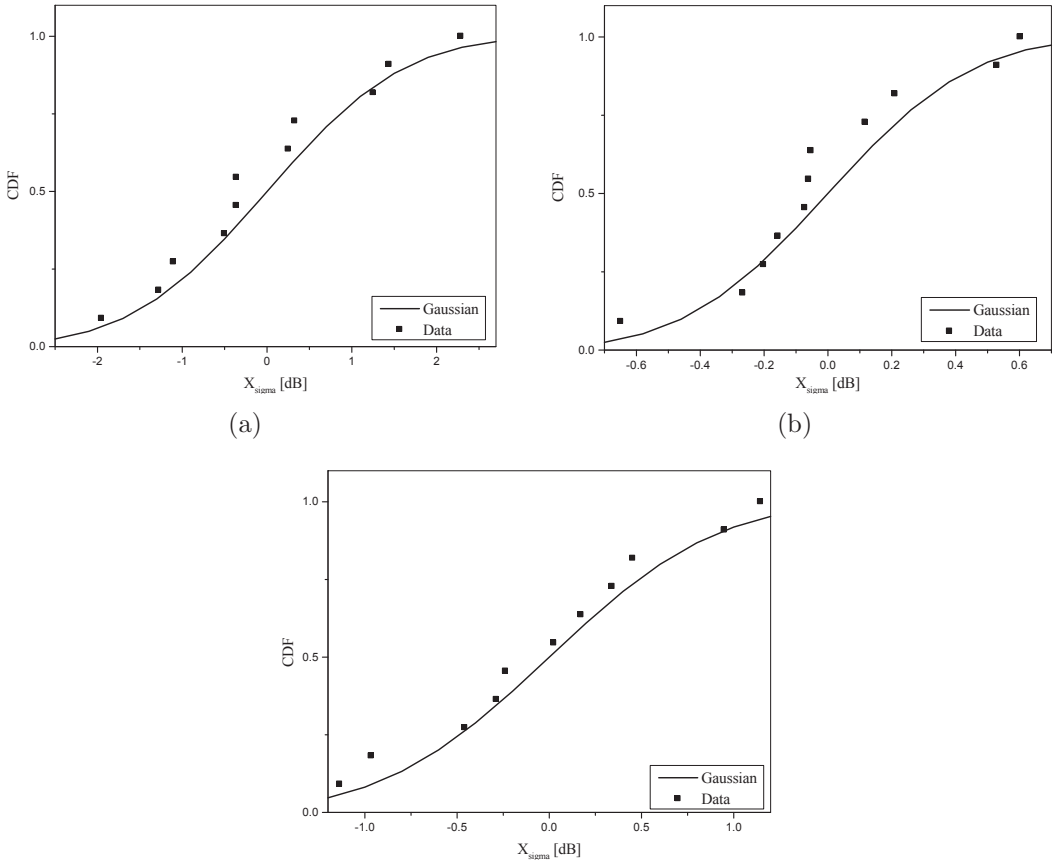

Figure 32: Zero-mean Gaussian distributed shadow fading and measured shadow fading for OLoS scenarios: (a) glass beaker; (b) plastic cup; (c) ceramic mug.

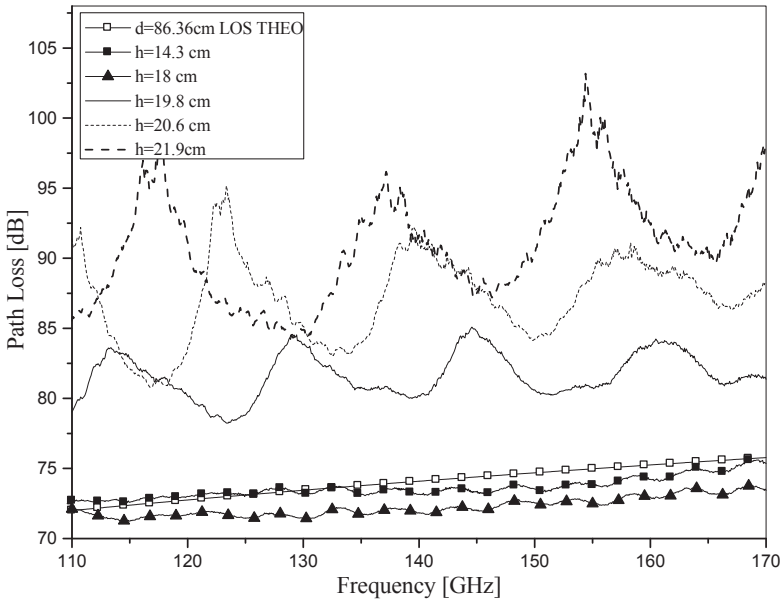

Figure 33: Variation in path loss with varying height of the ceramic mug obstruction.

about 2 dB below the free-space curve. Geometrical optics simulations reveal that the ceramic mug height of 18 cm at separation distance of 86.36 cm places the top rim of the mug on the boundary of the beam. This results in the second ray that reflects off the mug's top edge, which combines vectorially with the first LoS path, leading to a slight gain in the received power, and therefore slightly lower path loss than predicted by Eq. (20). On the other hand, as h increases, or as the mug obstructs more of the LoS path, it is observed that the path loss increases and becomes more frequency-dependent with higher peaks. For this case, our experimental results and an application of the Uniform Geometrical Theory of Diffraction (UTD) have revealed the presence of diffraction at the convex surface of the cylindrical obstruction. The creeping waves, or the surface-diffracted rays that travel around the cylinder in clock-wise and counter-clock-wise directions and their interference seem to be causing the variation in the measured S_{21}. Further characterization of this particular OLoS channel is one of our main future works.

5.4.2 OLoS Multipath Characterization

Figure 34 plots the power delay profiles for three obstructions: glass, plastic, and ceramics, respectively. We can observe that all three PDPs have two distinct segments: one where the reflection peak appears at the same time delay regardless of the T-R separation distance (shown as 1 in the figures), followed by the reflection peaks whose positions depend on the T-R separation distance (shown as 2 in the figures). Here we note that the difference between the first and the second arriving path is always equal to twice the cup diameter, regardless of the T-R separation distance, which explains why the multipath marked as 1 appears at the same excess delay for all distances. Furthermore, from the excess delay that corresponds to the first multipath (marked as 1 in the figures), we can conclude that this multipath corresponds to a ray that penetrated the cup, reflected off the wall closer to the R_x, reflected off the wall closer to the T_x and travelled outside the cup to the R_x. Although the higher order of reflections might be present, the receiver sensitivity is not high enough to detect them.

From Fig. 34, we can observe that the PDP for the plastic cup has weaker reflected paths compared to the glass and ceramic mugs because most of the energy goes through the plastics and does not stay trapped inside the obstruction. Furthermore, we can observe that the PDP for the ceramic mug has significant reflections only at the distance of 35.56 cm, whereas for 45.72 cm and 55.88 cm, it is difficult to identify them because the reflections are significantly attenuated due to material properties.

In the PDP section marked as 2 in Figs. 34(a), 34(b), and 34(c), we can observe that the position of the multipath peak depends on the T-R separation. From the excess delay that corresponds to the second multipath, we can deduce that the signal has travelled through the obstruction, was reflected from the R_x probe head, was reflected once more off the obstruction and then received by the receiver antenna. Alternatively, the signal was reflected off the obstruction, then reflected back from

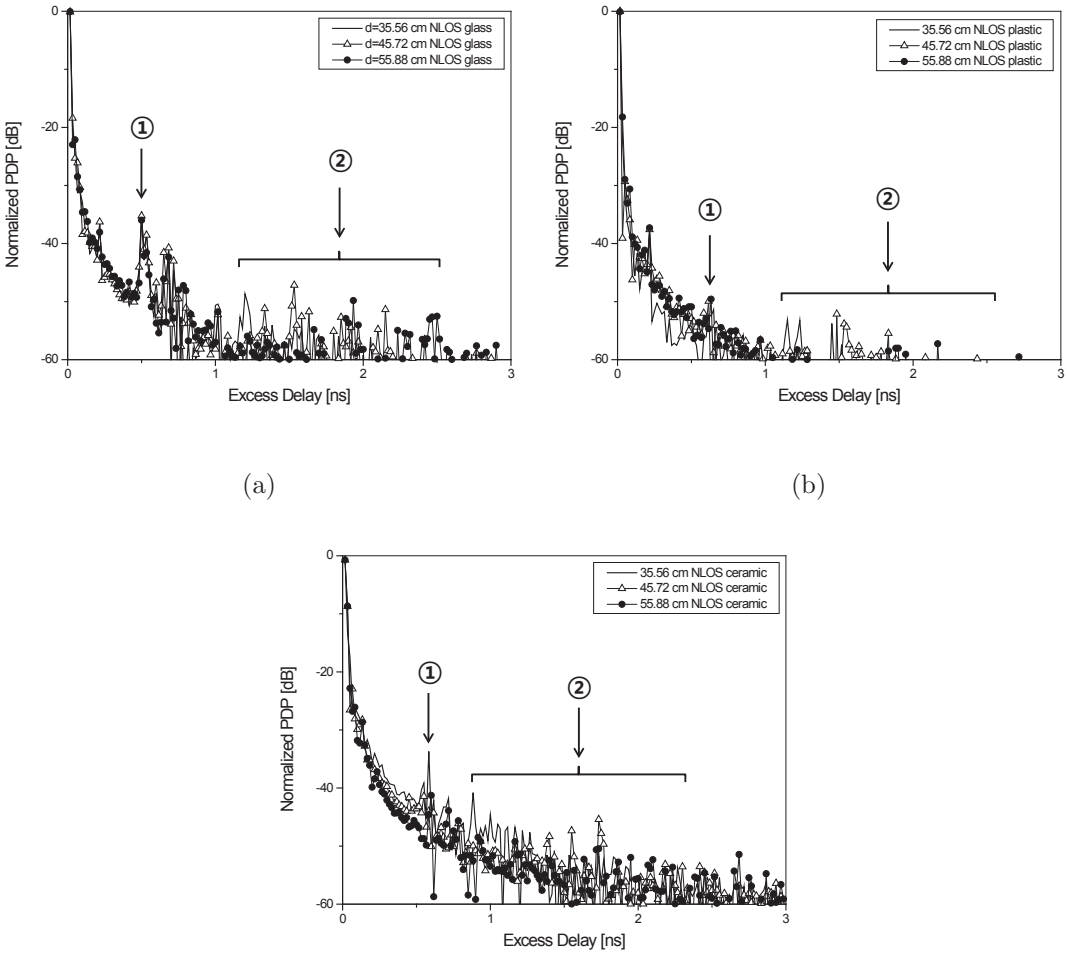

Figure 34: Power delay profiles for OLoS scenarios: (a) glass beaker; (b) plastic cup; (c) ceramic mug.

the T_x probe head, and then travelled through the obstruction to the receiver.

Note that the width of the main peak (first arriving path) is the widest for the ceramic mug, which is followed by the glass beaker and plastic cup, as observed in Fig. 34. This indicates that the ratio of the power associated with the strongest first arriving path to that of the following reflected paths is the highest for plastic, while the ratio is the lowest for ceramic. This agrees with the fact that glass is the most transparent to the waves, allowing most of the transmitted rays to pass through without multiple reflections. For ceramics, on the other hand, the transparency of the material is much lower than glass, which gives rise to more reflected paths that arrive with delays that are very close to each other. This high temporal proximity is manifested as a clustering of the reflected paths, which leads to pulse broadening as shown in Fig. 34(c).

Table 9: Mean excess delay, RMS delay spread, and coherence bandwidth for different obstruction materials.

d [cm]	Glass Beaker			Plastic Cup			Ceramic Mug		
	τ_m [ps]	τ_{rms} [ps]	B_c [GHz]	τ_m [ps]	τ_{rms} [ps]	B_c [GHz]	τ_m [ps]	τ_{rms} [ps]	B_c [GHz]
35.56	18.06	31.90	4.99	17.03	14.52	10.96	22.21	76.60	2.08
55.88	18.31	45.63	3.49	17.42	23.90	6.66	21.48	62.93	2.53
76.2	18.72	57.19	2.78	16.79	10.85	14.68	20.42	54.98	2.89

The multipath characterization parameters, τ_m, τ_{rms}, and B_c, in the OLoS environment with the three different obstructions for the three T-R spacings, 35.56 cm, 55.88 cm, and 76.2 cm, are summarized in Table 9. The OLoS channel obstructed by the plastic cup has the largest coherence bandwidth of almost 11 GHz at 35.56 cm, which is comparable with that of the LoS environment for the same distance. Meanwhile, much narrower coherence bandwidths below 5 GHz are observed for glass and ceramic mug obstructions.

5.5 Characterization of D-band Reflected NLoS Channel

Another possible way of communication is through reflected NLoS paths. Since the effectiveness of communication will depend on the reflectivity of the material, here we compare two different reflectors: aluminum plate and fiberboard. Furthermore, we investigate the effect of angular orientation of the receiver on the received power levels. The T_x is fixed at $\phi_T = 35°$, and the R_x is rotated between $\phi_R = 0°$ and $\phi_R = 90°$. The angles are measured from the direct LoS path. The T-R separation distance has been fixed at $d = 76.2$ cm. The measured and theoretical (free-space)

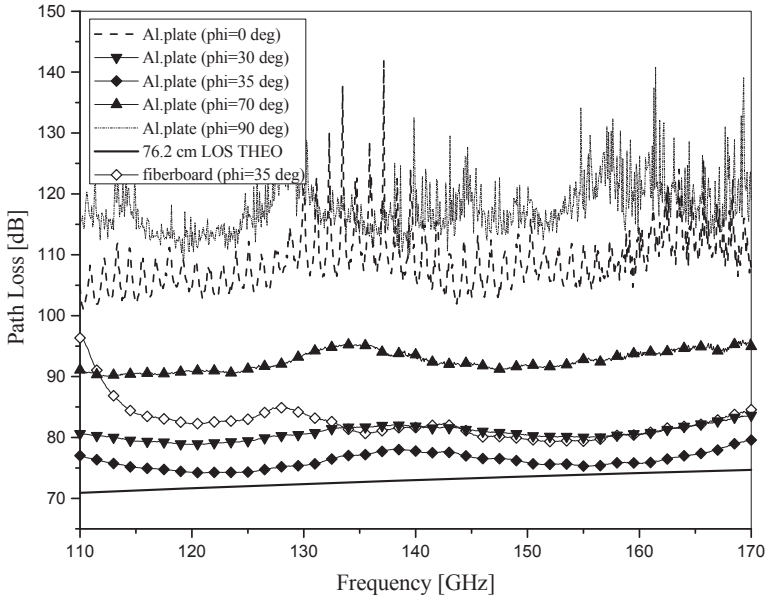

Figure 35: Measured RNLoS path loss for different R_x angles with aluminum plate, measured RNLoS path loss with fiberboard, and the theoretical free-space path loss for $d = 76.2$ cm.

path loss for several angles ϕ_R with aluminum plate and fiberboard as reflectors are shown in Fig. 35. It is evident from the figure that the level of received power is closest to the theoretical line-of-sight level when $\phi_R = \phi_T = 35°$, since the condition $\phi_R = \phi_T$ ensures that the maximum power is transferred through specular reflection. The slight discrepancy from the LoS level can be attributed to the reflection coefficient of the aluminum plate. As the receiver angle, ϕ_R, deviates from 35°, it is observed

that reception becomes weaker and the path loss significantly increases. At the two extremes, $\phi = 0°$ and $\phi = 90°$, we can observe that the communication is essentially lost. Furthermore, we can observe that the path loss is higher when the fiberboard is used as the reflector. This is not surprising result because the fiberboard has lower reflectivity and higher surface roughness.

The PDP's for the reflected NLoS channels with aluminum plate and fiberboard as the reflector for the angular positions, $\phi_R = 10°$ and $35°$ are presented in Fig. 36. The peaks that coincide at $\tau = 3.6$ ns represent the paths bouncing off the reflector, while an additional peak at $\tau = 2.7$ ns observed for $\phi_R = 10°$ is a result of the direct LoS path that arrives before the reflected path. Note that for the same receiver angle of $\phi_R = 35°$, aluminum plate and fiberboard produce similar PDP's with a single reflected path and no higher order reflections due to the high directivity of the antenna.

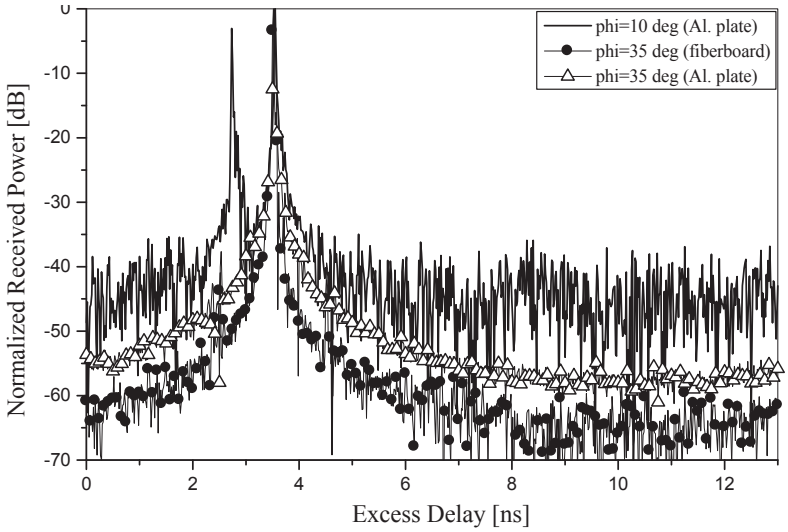

Figure 36: PDP for different R_x angles with aluminum plate and fiberboard as the reflecting surfaces.

Table 10 presents the mean excess delay, RMS delay spread, and coherence bandwidth for several receiver angular positions in RNLoS environment. As expected, we can observe the largest coherence bandwidth for $\phi_R = 35°$, at which maximum

Table 10: Mean excess delay, RMS delay spread, and coherence bandwidth for different receiver angular positions.

φ_R	Aluminum Plate			Cardboard		
	τ_m [ps]	τ_{rms} [ps]	B_c [GHz]	τ_m [ps]	τ_{rms} [ps]	B_c [GHz]
0º	65.72	312.89	0.51	-	-	-
10º	89.14	311.20	0.51	-	-	-
35º	17.07	9.36	17.00	18.18	36.84	4.32
60º	17.17	26.97	5.90	-	-	-
90º	132.36	678.48	0.23	-	-	-

power transfer occurs. At the same angle, when the reflecting surface is fiberboard, the coherence bandwidth is four times smaller. It is also observed that the coherence bandwidth reduces rapidly as the receiver angle deviates from 35°, dropping to MHz range at $\phi_R = 90°$.

5.6 UTD-based Diffraction Loss Modelling

5.6.1 Measurement Scenario

To measure the diffraction loss caused by the cylindrical obstruction in the OLoS environment, the measurement setup shown in Fig. 26(b) is used, where the cylinder obstruction of ceramic mug, initially blocking the LoS, is gradually moved away from the LoS along a trajectory perpendicular to the LoS in 2 mm increments. The separation distance between the T_x and R_x test heads is 86.36 cm, and the change in S_{21} with respect to that of the LoS is attributed to the effect of diffraction of D-band waves.

5.6.2 Comparison of Theoretical and Measured Results

Fig. 37(a) shows the projection of the problem onto 2-D Cartesian plane with a cylindrical coordinate system. As shown in the figure, sliding the cylindrical obstruction along a trajectory perpendicular to LoS is equivalent to the displacement of the source, P, and observation points, S, with the cylinder's center fixed at the origin. It follows that when the displacement of P, ΔP, and S, ΔS, is less than the outer radius of the

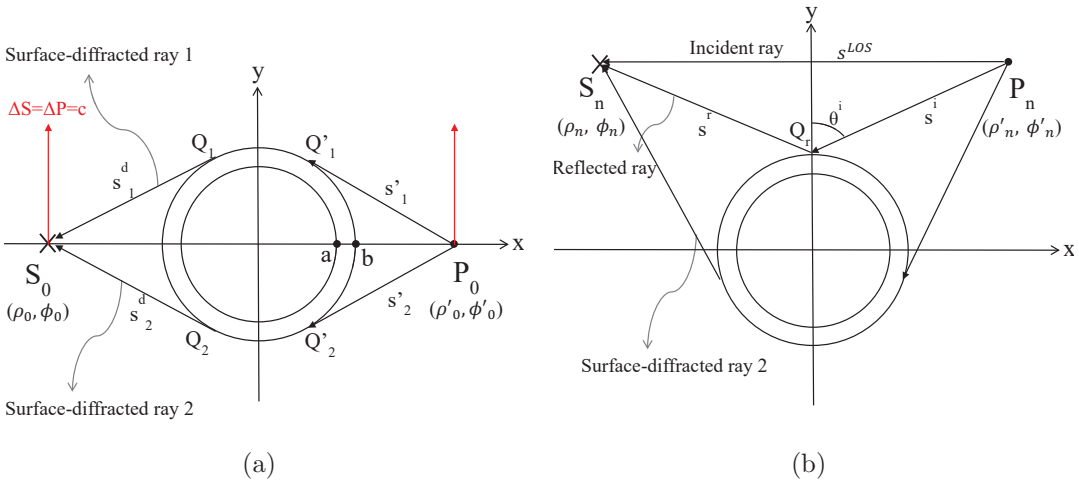

Figure 37: Ray components in (a) Shadow Region and (b) Lit Region.

cylinder (i.e., $c \leq b$ in Fig. 37(a)), S is in the Shadow Region, while, when it is greater (i.e., $c > b$), S is in the Lit Region. Applying UTD, in the Shadow Region, there are two surface-diffracted rays, travelling clock-wise and counter-clock-wise around the cylinder [113] as shown in Fig. 37(a), and therefore, the total E-field at the observation point, S_0, is determined by the sum of these two rays. In the Lit Region, on the other hand, the total field at the observation point, S_n, is determined by the superposition of the direct LoS ray, the reflected ray, and one of the surface-diffracted ray that travels along the far-side surface of the cylinder as shown in Fig. 37(b). The details of the mathematics of UTD formulation of each field component is presented in Appendix A.

Fig. 38 shows how the four field components, namely, the two surface-diffracted fields, direct incident field, and the reflected field, vary their magnitudes as the cylinder obstruction is moved away from LoS, or as c from Fig. 37(a) increases from 0 to 10 cm. Since the mug's outer radius, b, is 5 cm, the shadow boundary is located at $c = b = 5$ cm. In Fig. 38, it is observed that, initially, when the mug is totally blocking the LoS ($c = 0$ cm), the two surface-diffracted fields (E^{d1} and E^{d2}) have the same magnitudes, but as c increases, E^{d2} weakens, while E^{d1} increases. This is due to

the fact that the total distance the first surface-diffracted ray travels decreases, while the second surface-diffracted ray travels increasingly longer distance as the mug offset increases. It is also observed from Fig. 38 that when c reaches b ($c = b = 5$ cm), or the shadow boundary, the observation point now enters the Lit Region, and the first surface-diffracted ray (E^{d1}) now becomes the reflected ray (E^r) that starts decreasing with increasing c. Meanwhile, in this lit region, the direct LoS incident field (E^i) is also present, and the second surface-diffracted field (E^{d2}) still exists with small amplitude. Note that all field components shown in Fig. 38 are normalized to the incident LoS field strength. Finally, the calculated diffraction loss is plotted with respect to the mug offset distance, and compared with the measured one in Fig. 39. It is observed that the UTD modelled diffraction loss for the dielectric cylinder obstruction at D-band very closely predicts the measurement. The oscillation around 0 dB level is due to the constructive and destructive interference among the three rays present in the Lit Region, namely, the incident, reflected, and surface-diffracted rays as illustrated in Fig. 37(b). The excellent match achieved in Fig. 39 essentially confirms the existence of diffraction of D-band signals at the convex surfaces of the cylindrical obstruction as one of the propagation mechanisms present in this particular indoor OLoS scenario.

5.7 Summary

This chapter presents measurements and characterization of D-band indoor channels. The measurements are performed in LoS, OLoS, and RNLoS environments. For the OLoS scenario, cylindrical objects of different materials are used as obstructions. For RNLoS, different surfaces are used as reflectors. From the large set of LoS and OLoS measured data, the parameters for single-slope path loss model with shadowing are devised. Furthermore, the analysis of multipath propagation is performed. The rms delay spread, the mean excess delay, and the coherence bandwidth for LoS, OLoS,

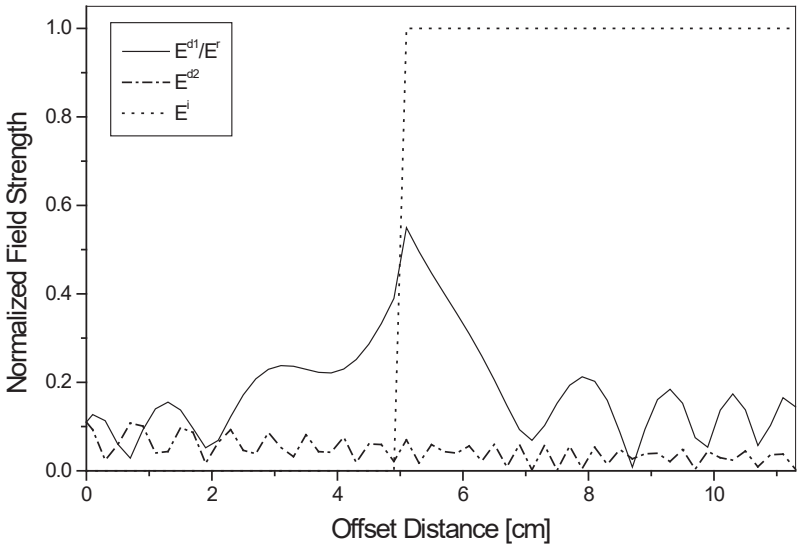

Figure 38: Comparison among field strengths of each ray component with respect to offset distance of the cylinder obstruction at $f = 140$ GHz.

and RNLoS environments are calculated. In addition, the power delay profiles for LoS, OLoS, and RNLoS environments are analyzed. The results show that strong multiple reflections from the transmitter and receiver electronics are present both in LoS and OLoS environments. Additionally, the results show that a ceramic cylinder in the propagation path produces two surface-diffracted rays that travel around the cylinder in clock-wise and counter-clock-wise directions, and their superposition leads to frequency-dependence in the path loss. Finally, the results show that the RNLoS measured path loss with aluminum plate as a reflector is very similar to free-space path loss when the angle of incidence and the angle of reflection are equal.

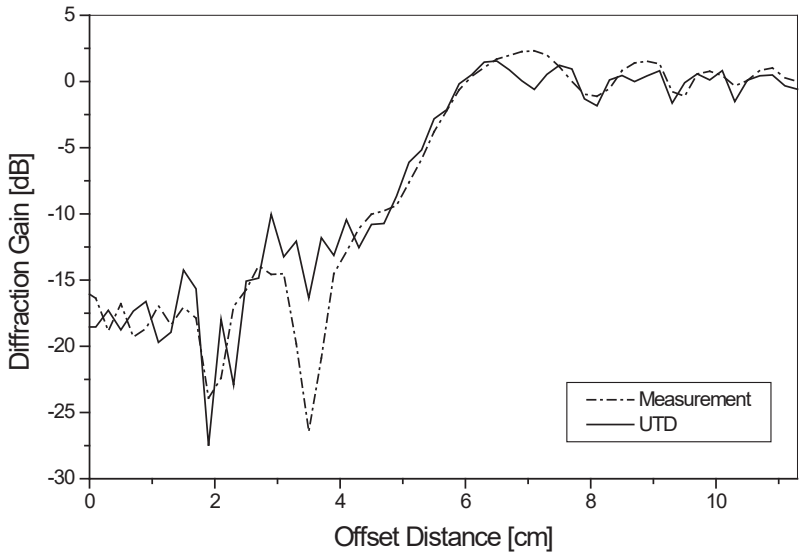

Figure 39: Measured and UTD modelled diffraction gain with the ceramic-mug-obstructed LoS channel at $f = 140$ GHz.

CHAPTER VI

CHARACTERIZATION OF 300 GHZ WIRELESS CHANNEL ON A COMPUTER MOTHERBOARD

6.1 Overview

Data communication between co-located computer systems, such as blades in a datacenter rack or units in a wireless base station controller, traditionally relies on either metal wires or guided (fiber) optics. Similarly, communication between components, such as processor and memory within a computer system, currently relies on metal wires and a transition to optical interconnects is expected in the future [38]. However, for system components, the number of pins or optical interfaces that a small chip package can have is limited, and sophisticated connections can also make component insertion (e.g. during assembly) and removal (e.g. to replace a failed component) more time-consuming and costly [40]-[42]. For communications between systems, cables (electrical or optical) require careful physical routing and "cable management" to allow good airflow (for system cooling), rapid servicing of failed computing blades/nodes, etc [43].

Wireless communication can alleviate such cable management, serviceability, and packaging constraints [43]-[54]. Integration of wireless transceivers and antennas into the chip package would provide communication bandwidth without adding pins or fiber connectors to the chip package [55]-[56]. A key challenge for wireless communication is that the required data rates in existing systems are already in the hundreds of gigabits per second. For example, a computer in a typical high-performance cluster gets 56 Gbits/s through an InfiniBand FDR X4 link [114], and this is expected

[115] to improve to 100 Gbits/s (InfiniBand EDR) and to 200 Gbits/s in 2017 (InfiniBand HDR). Achieving such per-link data rates is unlikely to be feasible for wireless communication at mm-Wave frequencies. As an example, WiGig [116] uses 60 GHz frequency range to provide up to 7 Gbits/s using OFDM, 64-QAM, and sophisticated coding.

A 300 GHz channel, on the other hand, can carry an ultra-high data rate, with much larger usable frequency band, over short-range with extremely narrow beamwidth, which makes it ideal for chip-to-chip wireless links, such as those on a computer motherboard, where propagation distance is typically less than 25 cm. The chip-to-chip channel environment is that of a very densely packed communications network, where LoS is a rare condition. Therefore, it is necessary to study the mm-Waves interaction with motherboard components by characterizing the path loss and multipath propagation in numerous channel environments found on a motherboard to test the feasibility of realizing Chip-to-Chip communication in the THz band.

To enable chip-to-chip THz wireless communications within a computer system, it is imperative to understand the propagation mechanisms that govern communication in its unique propagation environment at these high frequencies. While measurements on the computer motherboard have been reported at lower frequencies [57]-[59], to the best of our knowledge, no channel measurements in the computer motherboard environment at 300 GHz have been reported in the open literature. Therefore, we propose to graft the 300 GHz wireless channels onto the computer motherboard, where highly dense propagation environments produce different propagation scenarios, such as Line-of-Sight (LoS), Non-Line-of-Sight (NLoS), and Obstructed-Line-of-Sight (OLoS), with obstructing materials of varying reflectivity and surface roughness (e.g. FR4, metal, Silicon).

The remainder of this chapter is organized as follows: Section 6.2 briefly describes the equipment and the antennas used in the measurements. Section 6.3 describes

in detail the five measurement scenarios, and Section 6.4 presents the measurement results and analysis of the measured data for each scenario. Finally, Section 6.5 provides concluding remarks.

6.2 Measurement Setup

The block diagram of equipment setup and measurement parameters as well as the antennas used in this chapter are identical to those presented in Sections 3.3 and 4.2. (Fig. 3 and Table 2)

6.3 Measurement Scenarios

In this measurement campaign, five different scenarios have been considered:

1. Line-of-Sight (LoS) in the presence of a large ground plane
2. LoS with the height difference between the transmitter (T_x) and the receiver (R_x)
3. Reflected-Non-Line-of-Sight (RNLoS) link via reflection off the surfaces of vertically inserted components
4. Obstructed-LoS (OLoS) scenario where the EM waves travel through the metal parallel-plate structures
5. NLoS scenarios with a heatsink and a rotating fan as obstructions.

Figure 40 shows the chip locations that exemplify Scenarios 2, 3, and 4.

6.3.1 LoS over a Large Ground Plane

In contrast to a traditional LoS communication environment, where antennas are sufficiently elevated so that the ground plane has negligible impact on the measurements, in a chip-to-chip environment antennas are located very close to the motherboard (i.e., a large ground plane). Therefore, it is necessary to characterize LoS propagation in

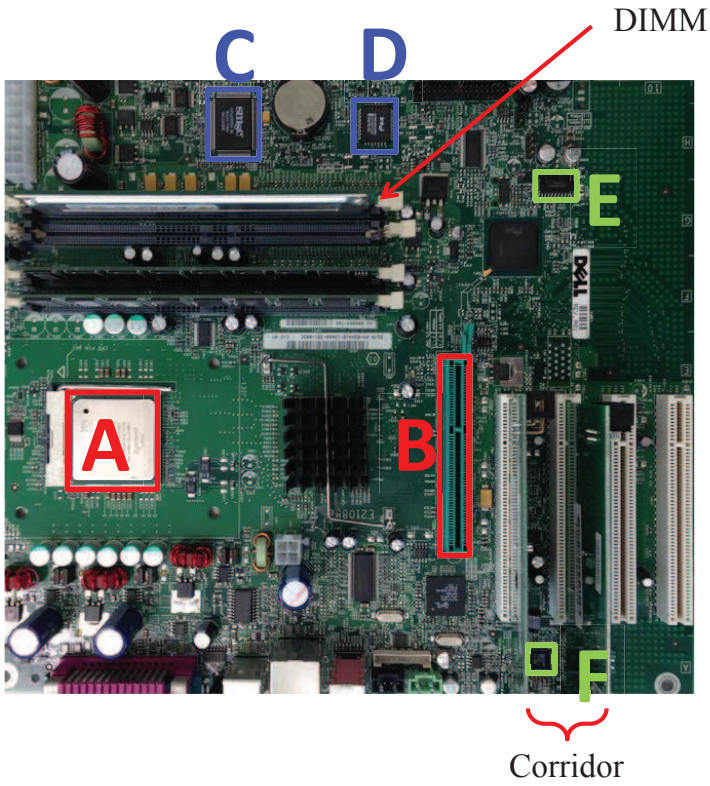

Figure 40: LoS CPU-AGP link (A-B), RNLoS link with DIMM as reflecting surface (C-D), and OLoS link through parallel-plate structures (E-F) on a motherboard.

the presence of a ground-reflected path. To separate the impact of the motherboard surface from that of other components on the board, we have used the backside of the motherboard and varied the T_x/R_x antenna height, h, to characterize the effect of the ground plane on the path loss. The measurement setup is presented in Fig. 41, where h is varied from 0 cm to 2.1 cm above the board. Please note that the antenna height of 0 cm refers to the case when the bottom edge of the horn touches the board surface, at which height, the phase center of the horn is 4.575 mm above the surface. Additionally, to test different materials that the motherboard surface consists of, we have measured the LoS path between T_x/R_x when signal travels over a more solder-pin-populated portion vs. flat FR4 surfaces. Finally, the material of the desktop, on which all measurement scenarios have been setup, is plywood.

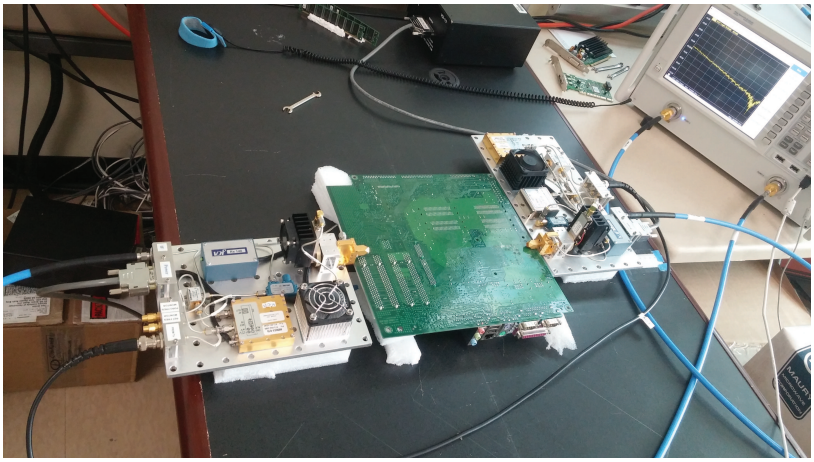

Figure 41: LoS propagation between the T_x and R_x over the motherboard.

6.3.2 CPU-AGP Link (Link A-B)

The LoS links on computer motherboards are prone to vertical misalignment between T_x and R_x antennas because of the chips that could be either located on the horizontal surface of the board or on vertical planes of the components that are vertically inserted into the slots. One example of such link is the CPU-AGP (Accelerated Graphics Port) link, or the Link A-B in Fig. 40, whose path loss has been measured using the setup presented in Fig. 42, where there exists 16.2 cm of T-R separation and 4.3 cm of vertical T-R misalignment. From Fig. 42, it can be also observed that, at farther distances from the CPU, there are other slots, i.e., PCI's (Peripheral Component Interconnects), where components can be inserted to form other vertical planes for the chips to be located on. Therefore, while maintaining the height difference of 4.3 cm, the T-R separation has been increased by moving the R_x module towards the PCI locations (i.e., increasing x in Fig. 42 in 2 cm increment from 16.2 cm to 26.2 cm).

Please note that it is not realistic to assume that manufacturer will always be able to align antennas for motherboard links. For example, when memory is a vertical card and processor is a horizontal chip, an antenna would have to be mounted on a plastic slot in which memory is inserted in order to be on the same height as the processor.

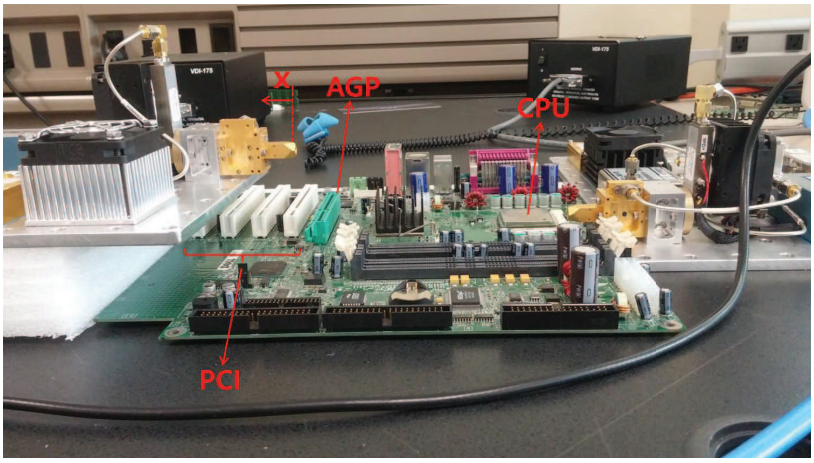

Figure 42: CPU-AGP Link (Link A-B) measurement setup with 4.3 cm of T-R height difference.

However, in that case, connection between the antenna and the memory card would be difficult. Even if the antennas between processor and memory are aligned, they would have to send signals through the plastic holder, which would significantly attenuate the signal. While tilting the antenna may seem as a simple solution for the propagation problem experienced with vertical misalignment between T_x and R_x as in a CPU-AGP environment, implementation of such a solution can be quite challenging, especially when planar antennas are required to facilitate integration with chips. Increasing the beamwidth of the antenna can be another solution to overcome the vertical offset between T_x and R_x, but the wider beamwidth would also increase delay spread, which, in turn, reduces the channel coherence bandwidth. Hence, a study of the extent of signal variation when antennas are misaligned in the vertical plane is important because it allows manufactures to estimate the performance vs. layout tradeoffs.

6.3.3 RNLoS Link with DIMM as Reflecting Surface (Link C-D)

Due to the densely populated environment on a motherboard, chip-to-chip links rarely have clear LoS paths. The vertically inserted components such as DIMM's and graphic/sound cards are major obstructions to chip-to-chip communications on

a motherboard. To study if these vertical components can be used as reflectors that enable Directed Non-Line-of-Sight links, we have measured Reflected Non-Line-of-Sight (RNLoS) paths between the chips C and D (see Fig. 40). It is observed that the LoS is obstructed by the metallic CMOS battery, which eliminates the possibility of clear LoS path. Therefore, this channel would have to rely on reflection off the DIMM surface. The reflective characteristics of these surfaces are studied using the experimental setup presented in Fig. 43, where the component (front) side of a DIMM is used as a reflecting surface. It is important to note that the measurement shown in Fig. 43 is not taken "on-board", but in an open setting, where the DIMM is the sole scatterer in the channel. Because of the high density of components on the computer motherboard, where the channel is affected by the scattering from multiple objects of different dimensions and material, it is necessary to factor out the effects of other components by re-constructing the local propagation environment of the channel in an isolated environment, such that complete individual assessment of each component's effect on propagation is possible. Furthermore, because the two sides of a DIMM (or card) consist of different materials and have different surface roughness, the front and back side are characterized as separate reflecting surfaces. Angles ϕ_T and ϕ_R marked on the figure represent the incident and reflection angles, respectively, and d is the distance between the T_x/R_x modules and the reflecting surface. The angle ϕ_R is varied from 34° to 50° in 2° increments, while the angle ϕ_T is kept fixed at 42° to study the range of angles at which specular reflection will exist. Additionally, the angles ϕ_T and ϕ_R have been varied from 20° to 80°, while keeping d constant ($d = 15.7$ cm), to obtain the magnitude of the reflection coefficient of each reflecting surface with respect to the incident angle. The incident and reflection angles, ϕ_T and ϕ_R, are set equal for the calculation of reflection coefficient to ensure specular reflection.

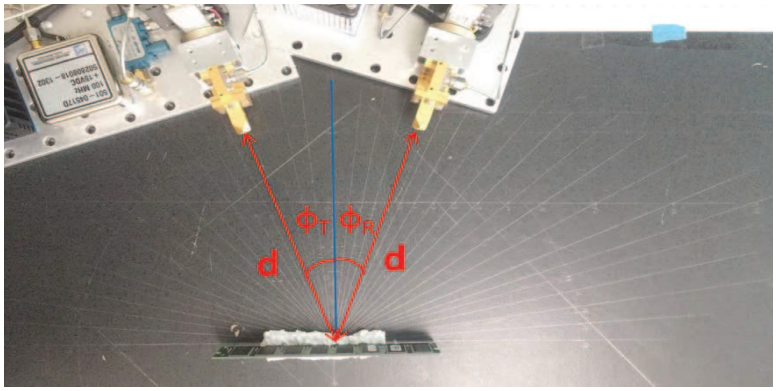

Figure 43: Measurement of a RLoS link using the component side of a DIMM as the reflecting surface.

6.3.4 OLoS Link through Parallel-Plate Structures (Link E-F)

Another important scenario for chip-to-chip communications is when the LoS link is perturbed by a parallel-plate structures, such as Link E-F in Fig. 40. Here, we have investigated whether these walls can act as parallel-plate waveguides or just introduce multipath propagation. The structural resemblance can also be found with the vertically inserted DIMMs. On the motherboard, due to its compact, highly dense configuration, it is difficult to differentiate the impact that one component has on the wave propagation from that of the other. For example, the effects of cylindrical capacitors present between the two DIMMs that would scatter or diffract the waves need to be differentiated from the wave-guiding effect of the DIMMs. Therefore, as shown in Fig. 44, we have isolated the local propagation environment of this particular chip-to-chip scenario and re-construct it on the backside of the motherboard. The figure also shows the corridor width, w, which has been varied from 1.7 cm to 5.2 cm to see how path loss changes with increasing or decreasing width.

6.3.5 NLoS Links

On a computer motherboard, there are numerous components other than DIMM's and cards that can obstruct the LoS path. While many of them directly block the signal, some of them such as a heatsink and a rotating fan have openings through

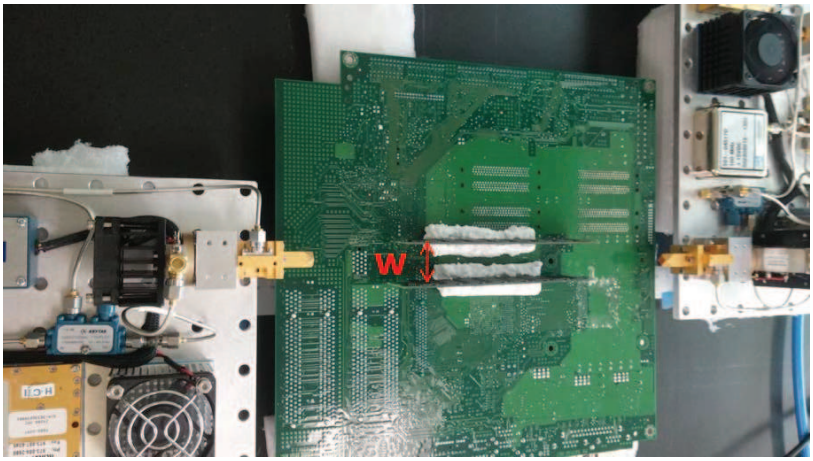

Figure 44: OLoS link through parallel-plate structure (DIMMs) on a motherboard.

which the signal may reach the receiver. Hence, we perform measurements in these environments as well, to estimate impact of the heatsink metal openings and fins of the rotating fan on the received signal. Figures 45(a) and 45(b) show the measurement setup for the heatsink and the rotating fan used as an obstruction, respectively. In the setup shown in Fig. 45(a), the heatsink with 7.7 cm of length is placed at the midpoint of four T-R separations, 11.7 cm, 16.7 cm, 21.7 cm, and 31.7 cm, which makes the distance from T_x to one end of heatsink (and from the other end to R_x) 2 cm, 4.5 cm, 7 cm, and 12 cm, respectively. Also, to investigate how the path loss changes when a wave passes through different sections of the heatsink, the T_x and R_x modules have been moved along the side of the heatsink, while their separation is fixed at 21.7 cm (i.e., x in Fig. 45(a) has been varied 0 mm, 2 mm, 5 mm, 7 mm, and 10 mm). For the fan obstruction shown in Fig. 45(b), the T-R separation distance has been varied from 10 cm to 30 cm in 10 cm increments.

6.4 Measurement Results and Analysis

6.4.1 Characterization of LoS Path Loss over a Large Ground Plane

Fig. 46 compares the measured and theoretically calculated path loss curves for the experimental setup described in Section 6.3.1, where T-R separation distance is 23.5 cm.

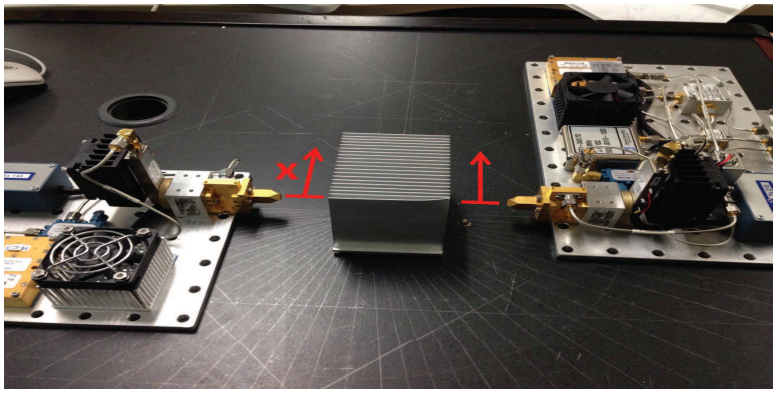

(a)

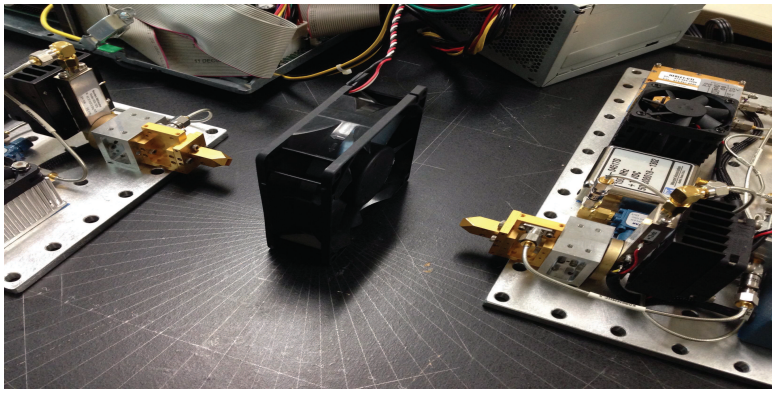

(b)

Figure 45: NLoS links with (a) a heatsink and (b) a rotating fan as an obstruction.

The oscillations observed in the measured path loss are the result of strong reflections that arrive at the receiver after reflecting off the T_x hardware. These multipaths that bounce between the T_x and R_x modules due to the narrow beamwidths of the antennas have also been observed in [67] for an LoS propagation environment. Furthermore, we can observe that the measured path loss when both the T_x and R_x are $h = 2.1$ cm above the ground plane follows the Friis formula prediction well. This is not a surprising result due to narrow beamwidths of the antennas and shows that the ground reflected paths do not reach the receiver at these antenna heights.

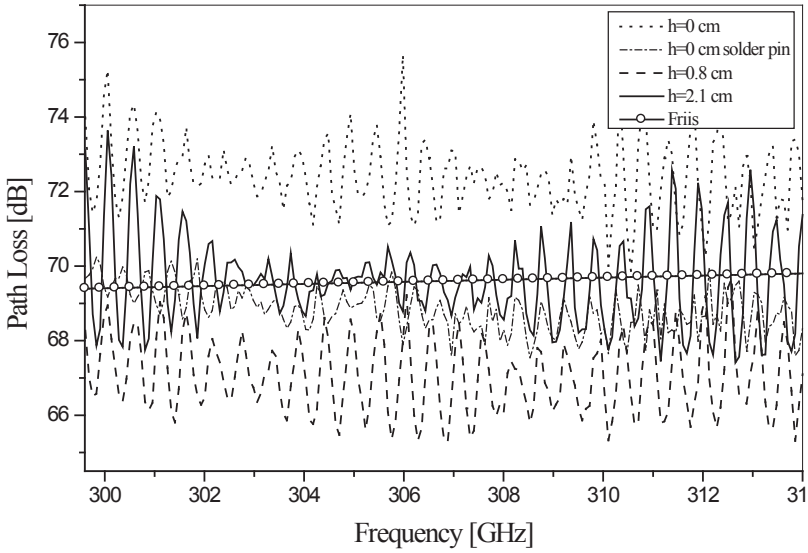

Figure 46: Measured and theoretical path loss curves for LoS link over the motherboard with T-R separation of 23.5 cm and varying T_x/R_x heights above the motherboard surface (in reference to measurement setup of Fig. 41).

It is also observed that, when antennas are positioned on the board surface (i.e., $h = 0$ cm), the ground reflections destructively interfere with the LoS path, resulting in about 3 dB higher path loss than what is predicted by the Friis formula. On the other hand, when the antennas are 8 mm above the board ($h = 0.8$ cm), the reflected and LoS paths constructively interfere, and the measured path loss actually becomes slightly lower than the theoretical free-space curve. To summarize, the oscillation in

measured path losses is due to the interference between the LoS and T_x-hardware-reflected paths that are in *different* delay bins, while the amplitude shift in the path loss arises from the constructive/destructive interference between the LoS and ground-reflected paths that fall within the *same* delay bin (i.e., their path length difference is smaller than the spatial resolution of the measurement system).

Table 11: Mean excess delays, RMS delay spreads, and coherence bandwidths for LoS link over the motherboard with different T_x/R_x heights.

	τ_m [ps]	τ_{rms} [ps]	B_c [GHz]
h=0 cm	7.35	118	1.35
h=0 cm solder pin	0.38	6.32	25.2
h=0.8 cm	10.3	137	1.16
h=2.1 cm	13.9	161	0.99

Another interesting observation from Fig. 46 is that for the same height of 0 cm, path loss is reduced by 3 dB when the antennas are placed over a section of the board that has higher solder pin density (refer to "$h = 0$ cm solder pin" in Fig. 46). This is because the amplitude and phase of the ground reflected signal are changed due to the higher reflectivity and surface roughness of the solder-pin-populated surface. Table 11 presents the measured RMS delay spread, mean excess delay, and the coherence bandwidth ($B_c = 1/(2 * \pi * \tau_{rms})$) for this measurement setup. It is observed that the coherence bandwidth decreases with the increasing height, and is significantly widened for the solder-pin scenario. This dramatic increase in the coherence bandwidth for the case of ground reflection off the solder-pin-populated surface is backed by the power delay profiles for this measurement setup (see Fig. 47). In the figure, the reflection from the T_x antenna back panel located at the excess delay of approximately 2 ns is clearly visible for each T_x/R_x height. A closer look at the profiles also reveals that the amplitude of the reflection is significantly reduced for the solder-pin scenario (marked with solid squares in Fig. 47) since the reflection is scattered, and therefore, weakened, by the obstructing pins. Also, multiple weaker reflections can be observed

in this case. Consequently, the RMS delay spread is dramatically reduced, which in turn resulted in much wider coherence bandwidth for this particular scenario.

These results indicate that the effect of ground reflections varies with the T_x/R_x height: a few millimeters of variation in T_x/R_x height off the board result in the increase or decrease in path loss by as much as 3 dB, depending on the nature of interference (i.e. destructive or constructive) between the LoS path and the ground-reflected path.

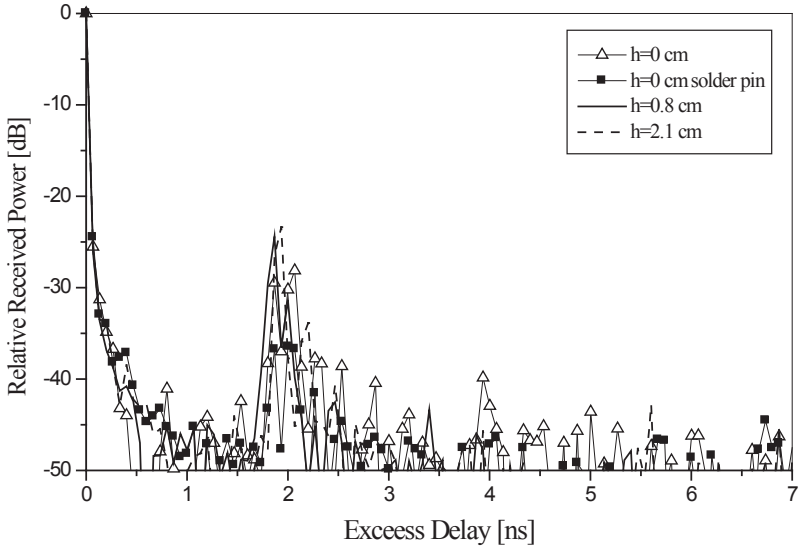

Figure 47: Normalized power delay profile for LoS link over the motherboard with different T_x/R_x heights above the motherboard surface (in reference to measurement setup of Fig. 41).

6.4.2 Characterization of CPU-AGP Link (Link A-B)

Link A-B, shown in Fig. 40, describes a typical link between the processor and the graphics card, where the T_x and R_x antennas are not on the same height. Fig. 48 shows the measured path losses for the setup presented in Fig. 42 as well as the corresponding theoretical values obtained from Eq.(22). We can observe that the path loss is higher for shorter distances, which may seem counter-intuitive. However, considering the geometrical structure, this is very possible. Note that the antennas have high directivity and narrow beamwidth and that height difference of 4.3 cm

creates very obstructed LoS propagation for short distances. On the other hand, as the distance increases, the T_x/R_x antennas start falling within each others' beamwidths, and more of the LoS power as well as the ground-reflected power is detected toward the receiver, which results in less path loss. However, note that even at maximum distance of 26.2 cm (i.e., size of the motherboard), the height difference of 4.3 cm still introduces a loss of about 15 dB with significant fluctuation in path loss. This result indicates that the A-B link is probably not a reliable channel, which raises the following question: how much of a height difference between T_x and R_x antennas can be tolerated?

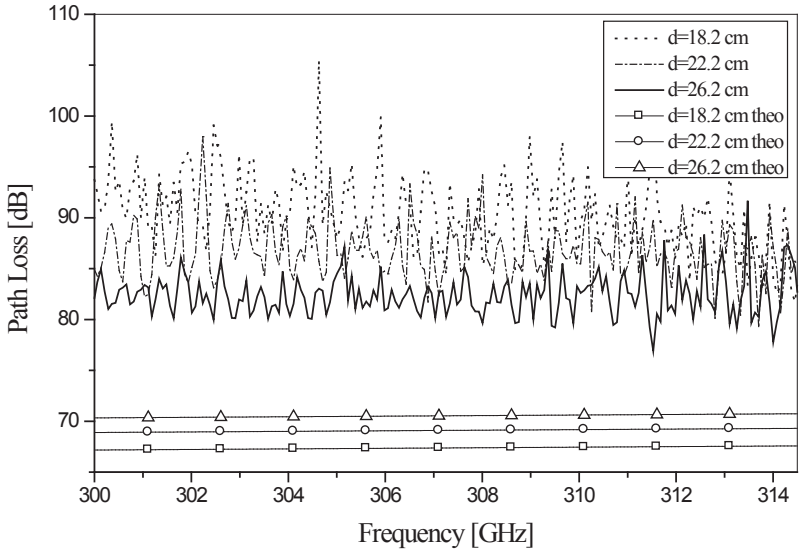

Figure 48: Measured and calculated path loss curves for CPU-AGP link (Link A-B) and CPU-PCI links with T-R height difference of 4.3 cm (in reference to measurement setup of Fig. 42).

Fig. 49 shows measured path loss curves for different heights of the R_x antenna when the T_x antenna is fixed at the height 2.1 cm from the board ($h_{T_x} = 2.1$ cm). The plot shows that for the height difference less than 1.3 cm, the measured path loss matches the theoretical values, while for greater height differences, measurements start to deviate from the Friis formula with greater fluctuation in path loss. From these results, we can conclude that the LoS chip-to-chip wireless channel on the

horizontal plane (on the motherboard surface) with minor T_x/R_x height difference is feasible, while the link between two chips, whose height difference is in the order of a few centimeters, such as Link A-B, will suffer from significant loss.

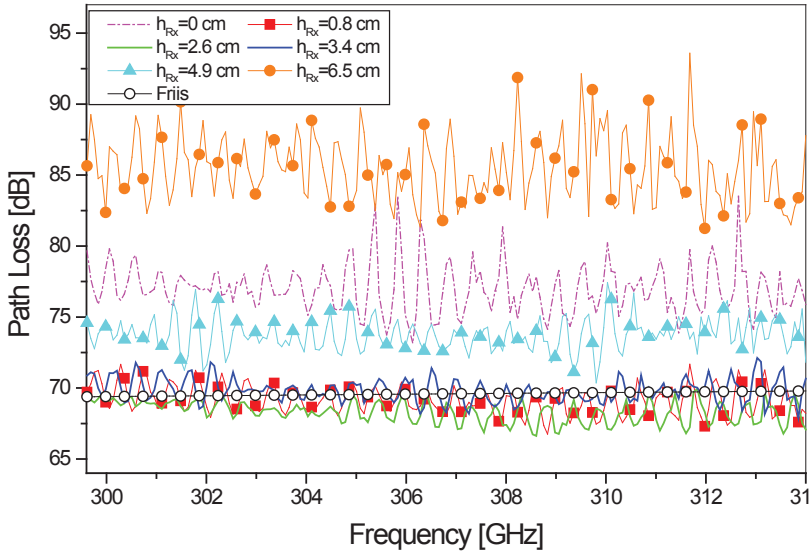

Figure 49: Measured and calculated path loss curves for A-B link with varying R_x antenna height when T_x antenna is fixed to $h_{T_x} = 2.1$ cm (in reference to measurement setup of Fig. 42).

Fig. 50 shows the scatter plot of the measured mean path loss for several distances as well as the regression fit through the measurements for a LoS link over the motherboard with 4.3 cm of height difference between T_x and R_x. From the regression fit, the path loss exponent is found to be $\gamma = -4.6302$; the path loss at the reference distance of 10 cm was $PL_0 = 102.384$ dB; and the standard deviation was $\sigma = 0.4179$ dB. Note that the negative path loss exponent found from Fig. 50 is the result of narrow-beam antennas as well as the presence of large ground plane.

It should be noted that, for motherboard channels with vertical T-R misalignment, there exists a trade-off between the path loss and the delay spread. When the antennas have wider beamwidth, more of the transmitted power will reach the vertically offset receiver, but more multipaths will also be created due to reflections from other motherboard components as well as the motherboard surface, increasing

the RMS delay spread, and therefore, reducing the channel coherence bandwidth. To verify this, a CST simulation has been performed, where two T_x/R_x horn antenna pairs with HPBW's of 10° and 26°, each separated by 16.2 cm with vertical offset of 4.3 cm as in CPU-AGP environment, are compared in terms of their S_{21} and RMS delay spread. The result has shown that an increase of 16° in HPBW results in a 20 dB increase in the received power and a 71.8 % reduction (from 606 MHz to 171 MHz) in coherence bandwidth. Therefore, selection of an appropriate antenna beamwidth that delivers enough power to all receiver locations, while minimizing delay spread, is critical for wireless channels on a computer motherboard.

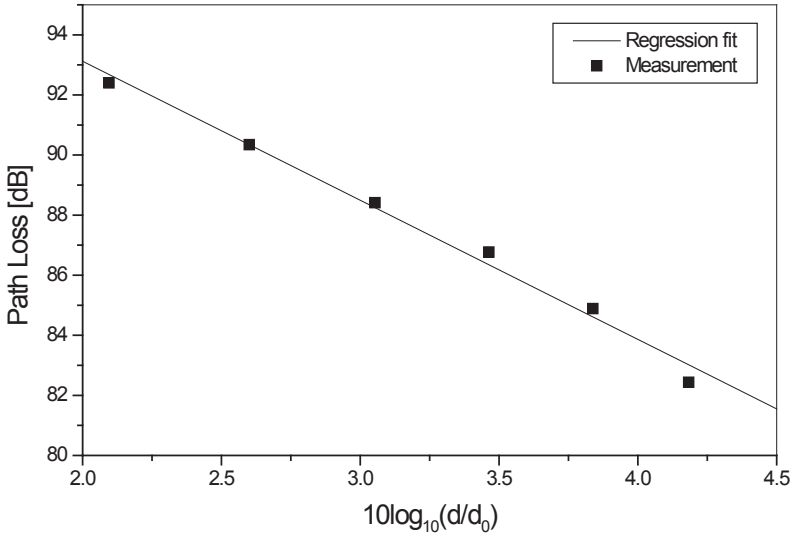

Figure 50: Measured mean path losses and regression fit for A-B link with 4.3 cm of height difference between T_x and R_x antennas ($d_0 = 10$ cm) (in reference to measurement setup of Fig. 42).

Fig. 51 presents the power delay profiles for several T-R separations when the difference between the T_x and R_x antenna heights is 4.3 cm. We observe that the reflections from the T_x arrive at the receiver with larger excess delay (i.e., $\tau = 1.8$ ns, 2.1 ns, and 2.4 ns) as the separation distance increases (i.e., $d = 18.2$ cm, 22.2 cm, and 26.2 cm, respectively) due to the longer path lengths that the reflected rays have to travel.

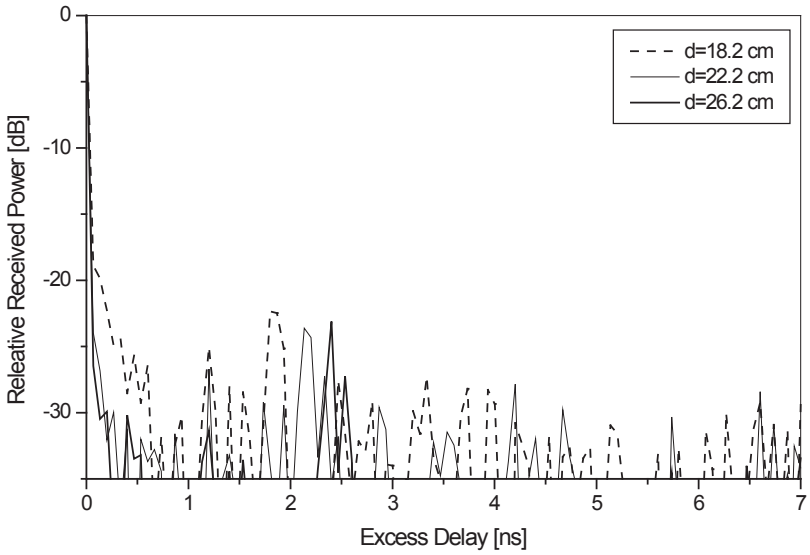

Figure 51: Normalized power delay profile for A-B link with height difference of 4.3 cm between T_x and R_x for different T-R separations (in reference to measurement setup of Fig. 42).

6.4.3 Characterization of RNLoS link with DIMM as Reflecting Surface (Link C-D)

In this section, we study if some of the components on the motherboard can be used as reflectors, i.e., we have analyzed Reflected Non-Line-of-Sight (RNLoS) paths using the measurement setup presented in Fig. 43, which is exemplified by the link between the chips C and D in Fig. 40.

Figure 52 shows the measured path loss plots with a DIMM as the reflecting surface, while the receiver angle ϕ_R is varied between 34° and 50° in 2° increments, while the transmitter angle ϕ_T is kept fixed at 42°. For both the front and back side of the DIMM, shown in Fig. 52(a) and 52(b), respectively, the measured path loss is the lowest for $\phi_R = 42°$, which means that maximum power transfer is occurring under the condition, $\phi_T = \phi_R$, for both sides of the reflective surface. The difference between them, however, is that, for the backside, the path loss increases linearly with the deviation from the specular reflection angle, 42°, while this is not necessarily the case for the front side of DIMM. For example, the second highest path losses are

for $\phi_R = 40°$ and 44°, then, the third highest path losses belong to $\phi_R = 38°$ and 46°, etc. For deviation greater than 6°, the path loss approaches noise level. On the other hand, for the front side of DIMM, the second highest path loss is for $\phi_R = 38°$, rather than 40° or 44°. Furthermore, it is observed that for receiver angles other than $\phi_R = 42°$ and 38°, the path loss curves are hard to distinguish. These results are closely related to the material inhomogeneity and surface irregularity of the DIMM's front side. The fact that its surface consists of more than one material of varying reflection coefficient and that it has high surface roughness creates diffuse reflections of random amplitudes, phases, delays, and propagation directions. Therefore, their vectorial sum at a specific point in space is also random.

Figures 53(a) and 53(b) present the PDPs for the front and the back sides of a DIMM, respectively. From the PDPs, it can be observed that a single cluster of later-arriving paths is detected for the front side of the DIMM (labeled 1 in Fig. 53(a)), while two such clusters are observed for the back side of the DIMM (labelled 1 and 2 in Fig. 53(b)). This is due to the different surface roughness and the reflectivity of the two sides. For the flat, highly reflective back side (Fig. 53(b)), there are three reflections: the first path at $\tau = 0$ is the one that starts at the T_x, reflects off the DIMM surface and arrives at the R_x (since there is no line-of-sight path); the reflection observed in Cluster 1 is the path that travels from the T_x, reflects off the DIMM surface, bounces off the back panel of R_x antenna, travels to the DIMM once again, and back to the R_x; the reflection observed in Cluster 2 is the path that travels from the T_x, reflects off the DIMM surface and the R_x back panel, travels back to the T_x through reflection off the DIMM, bounces off the T_x back panel and the DIMM surface, and finally reaches the R_x. For the front side of the DIMM (Fig. 53(a)), Cluster 2 is absent in the PDP since the surface is rougher and less reflective than the back side, so that it cannot produce a strong enough reflection that travels back to the T_x. Note that the trajectories of all of these multipaths have been identified

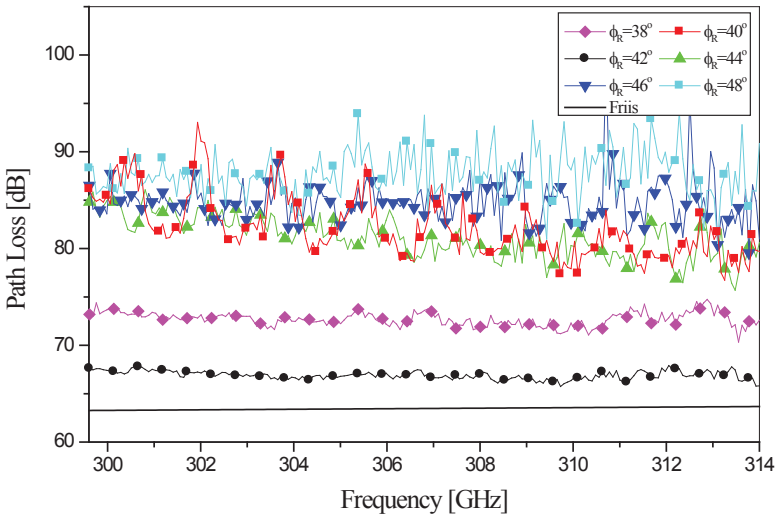

(a)

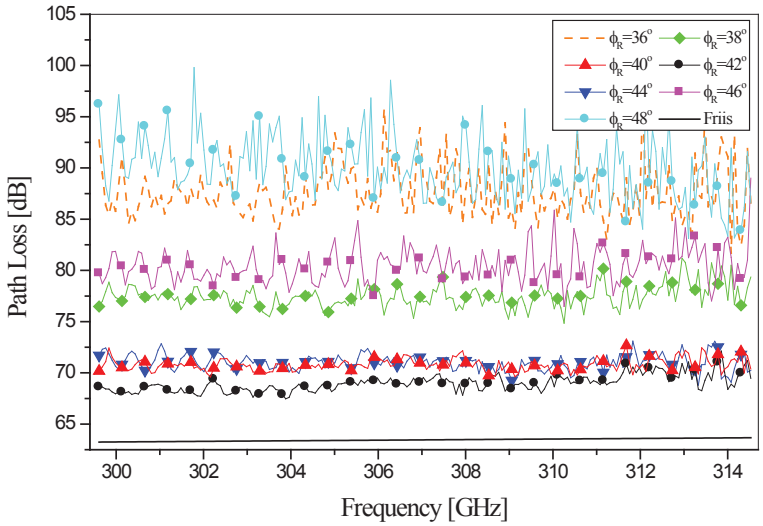

(b)

Figure 52: Measured and theoretically calculated path loss curves for RNLoS links with different receiver angles when the transmitter angle is fixed to $\phi_T = 42°$ and the DIMM is used as the reflecting surface (in reference to Link C-D and measurement setup of Fig. 43): (a) front side of DIMM; (b) back side of DIMM.

by computing the distance travelled with the excess delay of each path ($d = c \times \tau$). In Fig. 53(b), intuitively speaking, Cluster 2 should be weaker than Cluster 1 since it travels the longer distance. However, the Angle-of-Arrival (AoA) also impacts the power of the received signal. Especially, for such a narrow beam, the simulated radiation pattern of the horn reveals that the AoA of only 8° off the direction of maximum gain can lead to a 9 dB weaker detected signal. Therefore, even though Cluster 1 should have higher power than Cluster 2 (by 3.8 dB to be exact), the deviation of AoA from the maximum of the mainlobe can result in a 5 dB weaker power of Cluster 1 compared to Cluster 2.

The mean excess delays, RMS delay spreads, and the coherence bandwidths of this RNLoS channel with the three reflecting surfaces presented in Table 12 provide numerical verification of the qualitative analysis made from Fig. 53. It can be observed in Table 12 that the maximum coherence bandwidth is found for the DIMM back side for the angle of specular reflection, $\phi_T = \phi_R = 42°$, and as the receiver angle gets farther away from it, the coherence bandwidth decreases rapidly. Nevertheless, we can see that the coherence bandwidth stays in the GHz range up to 38° and 44°. For the DIMM front side, the largest coherence bandwidth is also found at $\phi_R = 42°$, but it is three times narrower than the coherence bandwidth of the back side. Additionally, other than $\phi_R = 38°$ and 42°, the coherence bandwidths significantly drop to the MHz range. It is also observed that the front side of a graphic card exhibits the lowest coherence bandwidth among the three surfaces due to its highest surface irregularity, while its maximum coherence bandwidth occurs at $\phi_R = 44°$, which is 2° off from the angle of specular reflection. Please note that the delay spreads presented in Table 12 are the values obtained in an "open" or "isolated" channel environment, and therefore, they cannot be directly related to more realistic motherboard environments. However, the purpose of this particular measurement campaign is to identify a 300 GHz wave's interaction with the common materials

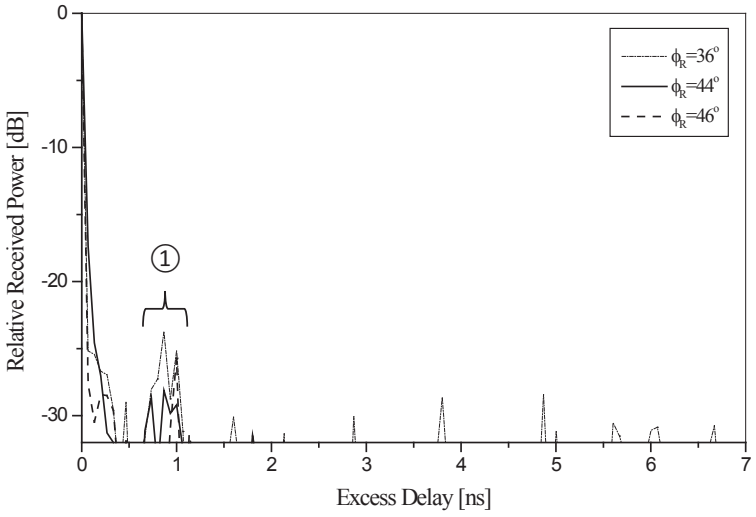

(a)

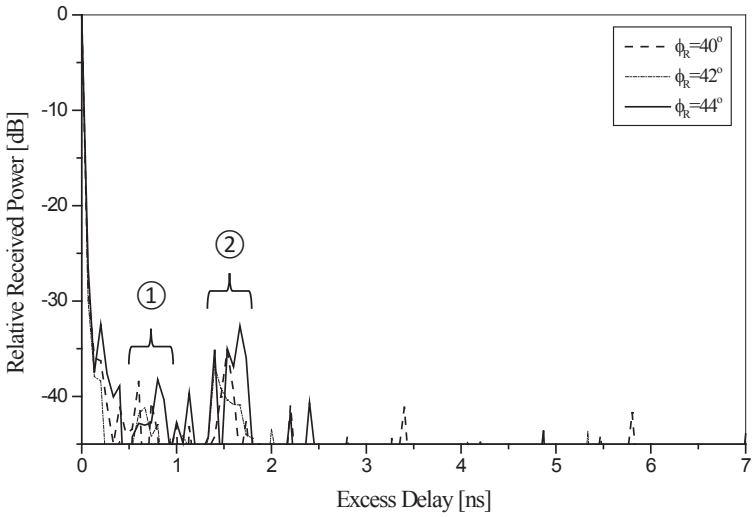

(b)

Figure 53: Normalized power delay profiles for RNLoS links with different receiver angles when the transmitter angle is fixed to $\phi_T = 42°$ and DIMM is used as the reflecting surface (in reference to Link C-D and measurement setup of Fig. 43): (a) front side of DIMM; (b) back side of DIMM.

found on the motherboard in terms of their penetration/reflection characteristics. In other words, the coherence bandwidths provided in Table 12 can be considered as the maximum possible values when no other components on the motherboard are obstructing the RNLoS path between two chips. Furthermore, in Table 12, we have shown how delay spread varies as the angular orientation of receiver deviates from that of the transmitter, which captures more practical aspects of RNLoS channels on a motherboard since it is not realistic to expect specular reflection for all antenna positions on a computer motherboard. Such information will be useful for layout designers and manufacturers.

Table 12: Mean excess delay, RMS delay spread, and coherence bandwidth for the RNLoS scenario with different reflecting surfaces.

ϕ_R	DIMM cmp side			DIMM back side			Card cmp side		
	τ_m [ps]	τ_{rms} [ps]	B_c [GHz]	τ_m [ps]	τ_{rms} [ps]	B_c [GHz]	τ_m [ps]	τ_{rms} [ps]	B_c [GHz]
34°	827.9	3245	0.049	761.2	2987	0.053	-	-	-
36°	523.7	2583	0.062	408.1	2256	0.070	-	-	-
38°	0.411	7.57	21.02	1.238	41.64	3.821	630.5	2813	0.056
40°	51.62	750.7	0.21	0.087	2.414	65.91	560.8	2672	0.059
42°	0.311	6.015	26.46	0.066	2.108	75.47	5.219	83.24	1.911
44°	28.06	463.9	0.34	1.163	39.17	4.062	1.257	31.47	5.057
46°	188.7	1546	0.103	17.81	250.1	0.636	1.541	36.01	4.419
48°	397.1	2164	0.074	713.1	2915	0.054	441.3	2382	0.066
50°	719.2	2899	0.055	929.5	3405	0.046	835.9	3284	0.048

Finally, Fig. 54 shows the magnitude of the reflection coefficients of the three surfaces (DIMM front side, DIMM back side, and graphic card front side) as a function of incident angle. The reflection coefficient is found from the reflection loss of each surface, i.e.

$$RL = -20log_{10}|\Gamma|, \tag{36}$$

where Γ is the reflection coefficient, and RL, reflection loss in dB, is calculated from the link budget equation:

$$RL = P_t - P_r + G_t + G_r - \tilde{PL} \ \ [\text{dB}], \tag{37}$$

where $\tilde{PL}$ is the theoretical free-space path loss calculated with Eq. (21).

The incident angle is measured from the surface normal, i.e., it is the angle $\phi_T (= \phi_R)$ in Fig. 43. From Fig. 54, it is observed that the reflection coefficient of the DIMM back side stays near 1 for all incident angles. This indicates that the back side of the DIMM serves as a good reflecting surface for all incident angles for a RNLoS link with minimal power loss. On the other hand, the component side of the DIMM, whose surface is rougher compared to the back side and consists of different materials (e.g. Silicon, FR4, metal), each having different reflection losses, shows a much more incident-angle-dependent reflection coefficient that fluctuates between 0.2 and 1. The same sensitivity to incident angle is observed for the front side of the graphic card as well, where, in general, the reflection coefficients are lower than those of the DIMM front side due to higher surface irregularity; even for a small incident angle of 20°, the reflection coefficient for a graphic card component side is less than 0.3. We can conclude that the back side of a DIMM is an excellent reflector for a reliable RNLoS link, whereas it would be much more difficult to predict the path loss of the RNLoS channel with the component sides as the reflecting surface.

6.4.4 Characterization of OLoS Link through Parallel-Plate Structures (Link E-F)

Another important scenario for chip-to-chip communications is when the LoS link is perturbed by a parallel-plate structure, such as Link E-F in Fig. 40. This channel has been replicated in an open measurement setup shown in Fig. 44, and the path losses measured are compared with the theoretically obtained path loss curves in Fig. 55 for different distances between the two DIMMs, w, when the T-R separation is 23.5 cm.

It is observed that the path loss increases considerably above the theoretical level

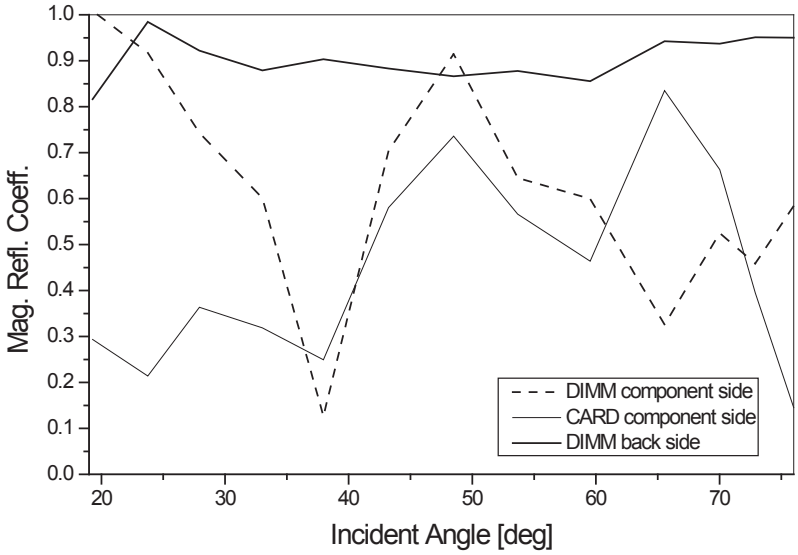

Figure 54: Magnitude of the reflection coefficients for three reflecting surfaces as a function of the incident angle (in reference to Link C-D and measurement setup of Fig. 43).

for $w = 2.3$ cm, while for $w = 3.3$ cm, the measured path loss is less than what is predicted by Friis equation. Finally, for $w = 5.2$ cm, the measured path loss returns to the theoretical level. These results indicate that there exist multipaths inside the corridor created by the two DIMMs: LoS and paths bouncing between the two DIMMs. The amplitude, phase, and delay of the bounced paths are determined by the width of the corridor, w. The results show that the interference among the multipaths is destructive when $w = 2.3$ cm, while they are superimposed in a constructive manner for $w = 3.3$ cm to yield much lower path loss. When $w = 5.2$ cm, the corridor width is now much wider than the antenna beamwidth, and the channel has only the LoS path, yielding measured path loss that follows the Friis formula. These results indicate that this channel can be used for chip-to-chip communications with careful selection of spacing between memory plates. Here, we also note that the oscillations in the measured path loss curves are still visible since the reflections between the T_x and R_x antenna back panels exist in the LoS channel. These strong reflections are clearly visible from the power delay profiles presented in Fig. 56. Note that the T_x/R_x

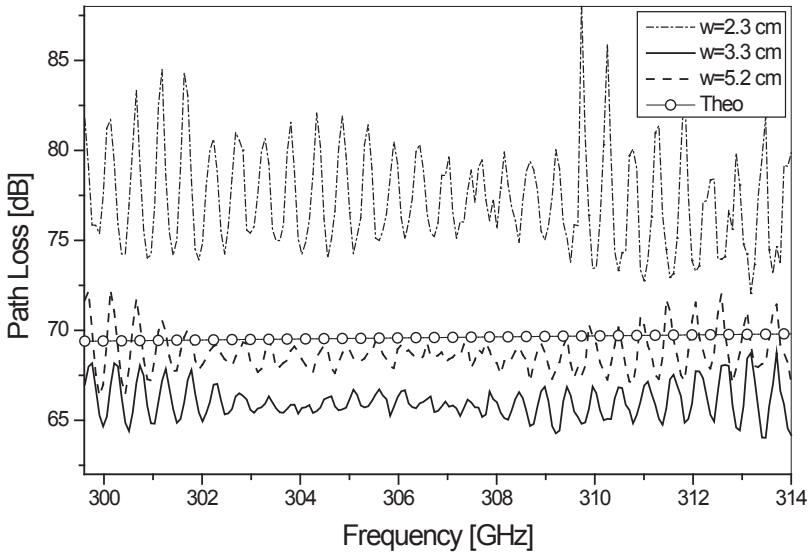

Figure 55: Measured and theoretically calculated path loss curves for OLoS link through parallel-plate structure with T-R separation of 23.5 cm and different spacing between the two DIMMs (in reference to Link E-F and measurement setup of Fig. 44).

antenna heights are set to 2.1 cm from the motherboard to ensure that the measured path loss is not affected by the ground reflection.

6.4.5 Characterization of NLoS Links

On a computer motherboard, there are numerous components other than DIMMs and cards that can obstruct the LoS path. In this section, the impacts of a heatsink and a rotating fan have been studied with the measurement setup shown in Fig. 45. Figure 57 presents the measured path losses along with the corresponding theoretical curves for different T-R separation distances for a heatsink-obstructed NLoS link. While some of the power is scattered or reflected by the metallic heatsink, most of the power still travels through the vertical gaps between the walls of the structure. Therefore, it is observed that the measured path losses are not significantly higher than the theoretical values. In fact, a heatsink is another type of metal parallel-plate structure that raises the possibility of constructive/destructive interference between the LoS path and the path bouncing between the plates.

To confirm this, Fig. 58 shows the path loss curves for a fixed T-R separation of

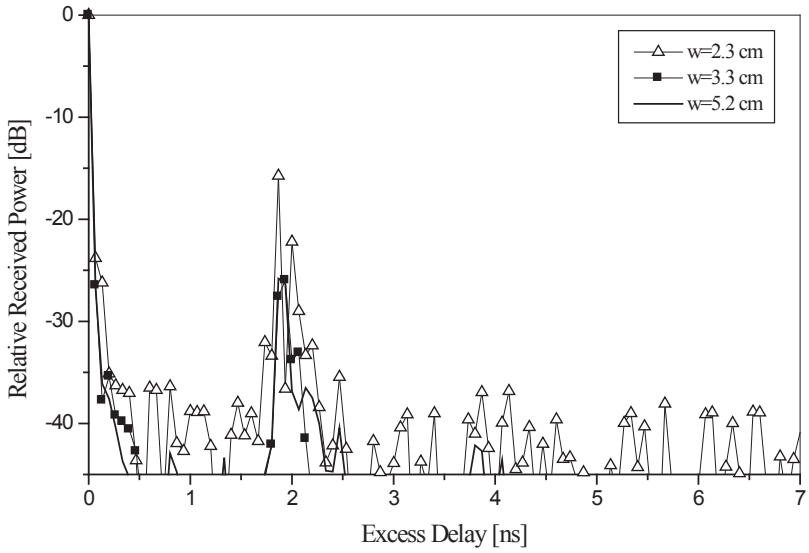

Figure 56: Normalized power delay profile for OLoS link through parallel-plate structure with different spacing between the two DIMM's (in reference to Link E-F and measurement setup of Fig. 44).

21.7 cm when the T_x/R_x antennas have been moved along the side of the heatsink (i.e., x is varied between 0 mm and 10 mm in Fig. 45(a)). Here, we observe a similar phenomenon as in Figs. 46 and 55, where the constructive interference between the LoS and bounced paths results in lower path loss than what is theoretically calculated (see $x = 2$ mm and $x = 10$ mm in Fig. 58). Further, it is also similarly observed that, at the T_x/R_x offset of 5 mm ($x = 5$ mm), path loss increases above the theoretical line due to the destructive interference. These results reveal that a heatsink-obstructed NLoS channel can actually be used for a chip-to-chip link with careful positioning of the antennas with respect to the geometry of the heatsink.

Fig. 59 shows the regression fit through the mean path losses measured at different T-R separations with the heatsink as obstruction. A path loss exponent of approximately $\gamma = 1.77$ is found, while path loss at the reference distance of $d_0 = 10$ cm and the standard deviation are found to be $PL_0 = 64.519$ dB and $\sigma = 0.9584$ dB, respectively.

The PDP for the heatsink-obstructed NLoS scenario is shown in Figs. 60, where it

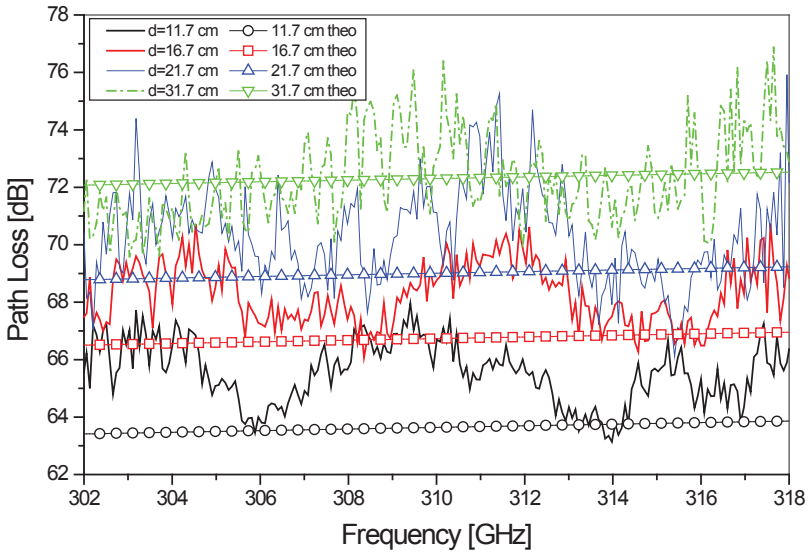

Figure 57: Measured and theoretically calculated path loss curves for heatsink-obstructed NLoS link with different T-R separation distances (in reference to measurement setup of Fig. 45(a)).

is observed that there exist second- and third-arriving multipath for each separation (i.e., located at $\tau = 0.4$ ns and 0.9 ns for $d = 11.7$ cm; $\tau = 0.6$ ns and 1.2 ns for $d = 21.7$ cm; and $\tau = 0.9$ ns and 1.9 ns for $d = 31.7$ cm). This result indicates that there are multiple reflections between the R_x antenna back panel and the surface of the heatsink.

Finally, for a fan-obstructed NLoS link, frequency-sweeping is not an appropriate measurement technique since the channel can no longer be considered quasi-static within the sweep time due to the rotating fan that constantly changes the macroscopic geometry of the channel. Therefore, for this scenario, continuous wave time-domain measurement at single frequency has been obtained. Similar time-domain analysis of DTV signal through wind turbines has been reported in [117]. The measured received power is presented in Fig. 61, where periodic fading is observed every 3.2 ms due to the blockage of the signal by the blades rotating at a constant speed. The result indicates that, for chip-to-chip wireless links through a rotating fan, a synchronization technique is needed, such that signal bit sequences are delayed during the times of

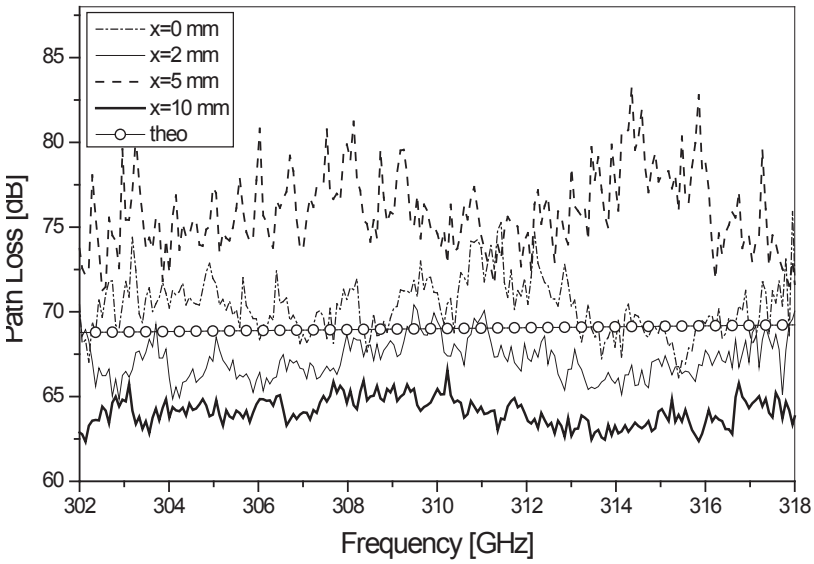

Figure 58: Measured and theoretically calculated path loss curves for heatsink-obstructed NLoS link with different orthogonal T_x/R_x offsets (in reference to measurement setup of Fig. 45(a)).

deep fades.

6.5 Summary

This chapter presented characterization of a 300 GHz wireless channel in a computer motherboard environment. Results indicate that the presence of the ground plane or parallel-plate structures in the channel introduces multipaths that if constructively superimposed may create path loss lower than the free-space propagation path loss. Additionally, our results show that the LoS channel over the motherboard with a few centimeters of height difference between the T_x and R_x antennas suffers from significant path loss, and has a negative path loss exponent. Furthermore, we have tested the possibility of using some of the vertical components as reflectors to alleviate the problem of no LoS communication paths. Our results show that the back side of a DIMM has an excellent reflecting surface with the widest coherence bandwidth and

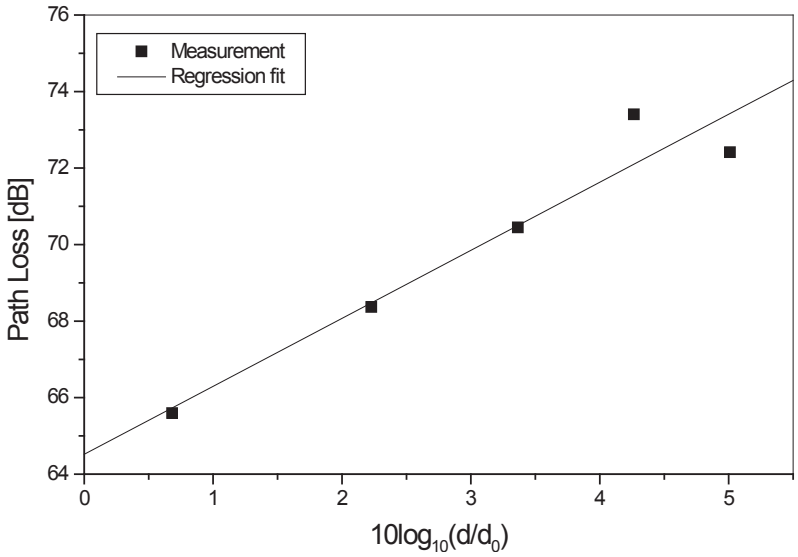

Figure 59: Measured mean path losses and the regression fit for NLoS link with a heatsink as obstruction ($d_0 = 10$ cm) (in reference to measurement setup of Fig. 45(a)).

highest reflection coefficient which can enable RNLoS links on a computer motherboard. Finally, we have investigated the impact of large objects that prevent LoS propagation on a motherboard. For the heatsink-obstructed NLoS link, it is found that the path loss exponent is 1.77, while the rotating fan causes periodic fading in the received power. For chip-to-chip wireless links through a rotating fan, therefore, a synchronization technique is necessary, such that signal bit sequences are delayed during the times of deep fades. All these results indicate that optimal communications can be achieved by carefully positioning the antennas with respect to the motherboard layout.

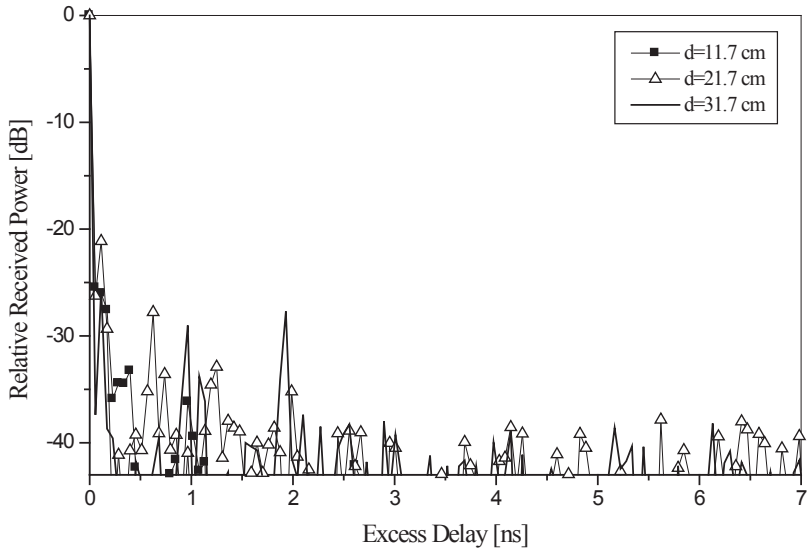

Figure 60: Normalized power delay profile for heatsink-obstructed NLoS link with different T-R separation distances (in reference to measurement setup of Fig. 45(a)).

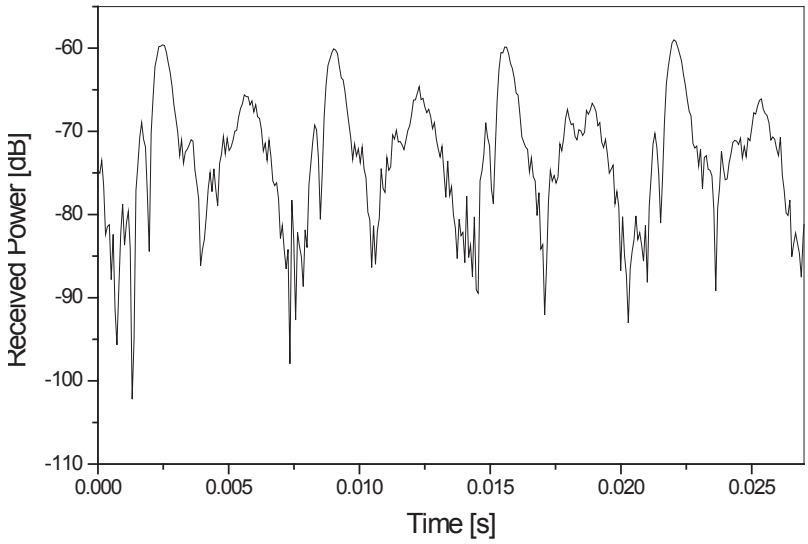

Figure 61: Time domain measurement of received power for NLoS link obstructed by a rotating fan ($f = 310$ GHz) (in reference to measurement setup of Fig. 45(b)).

CHAPTER VII

STATISTICAL MODELING AND SIMULATION OF SHORT-RANGE DEVICE-TO-DEVICE COMMUNICATION CHANNELS AT SUB-THZ FREQUENCIES

7.1 Overview

Deterministic THz channel models based on a ray-tracing method have been reported in the literature [35], where measurements obtained from a small office environment are compared with ray-tracing simulations. However, the accuracy of the ray-tracing model depends heavily on complete knowledge of material properties, such as reflection and scattering losses that vary with incident angle, dielectric constant, and surface roughness. Furthermore, precise modelling of propagation mechanisms, such as diffraction, which is highly affected by the shape and material properties of the obstruction, is required. The characterization of building materials for THz channels have been reported in [83], while the impact of reflections from these materials as well as the modelling of scattering and diffraction have been studied for indoor THz communication in [82], [34], and [61], respectively. However, it is quite difficult to have exact, a priori knowledge of the propagation environment and to deterministically model the randomly combining effects of different propagation mechanisms. Other THz indoor propagation models based on ray-tracing are found in [60], where the power of a single-reflected NLoS path is modelled by a summation of clusters with standard deviation statistics of amplitude and AoA (Angle-of-Arrival) that are pre-defined for a specific wall material (plaster) in [61]. Further, the model includes

reflection and scattering losses that need to be re-calculated for different polarization, dielectric constant, and Rayleigh roughness factor of the reflecting surface. As these material-specific parameters limit the practicality of ray-tracing-based channel models, for the cases when the number of multipath components is large, or when the geometry and dielectric properties of the propagation environment are unknown, we must use statistical approximations to characterize the propagation medium.

In [62], the first stochastic model for THz indoor channels is proposed. In the proposed model, frequency-dependent path gain model [63] and the indoor Saleh-Valenzuela model [64] are adapted for the THz frequencies, and ray-tracing simulation for an office environment is performed to extract the statistical parameters that are used for the generation of a large set of channel realizations. While this approach significantly simplifies channel simulations, it does not provide insight into statistical properties, such as the correlation function (i.e., function that characterizes how fast a wireless channel changes with time, movement, or frequency) and the power delay profile (i.e., the function that characterizes multipath propagation). These statistics enable the system designer to make informed decisions when choosing modulation, interleaving, and coding schemes at the transmitting end and the type of channel estimator and decoder at the receiving end. Further, the fact that ray-tracing has to be re-run for the adaptation of the model to a new environment due to the THz propagation's high dependence on materials can limit the time-efficiency of the channel model. Therefore, this chapter proposes a geometry-based statistical approach to the modelling of wireless channels at sub-THz frequencies, where the mathematical reference model for short-range sub-THz multipath fading channels is developed and compared with measurements collected around $110 - 170$ GHz (D-band) and $300 - 320$ GHz for validation. Furthermore, a sum-of-sinusoids based (SoS) simulation model is proposed to overcome the assumption of the reference model that there is an infinite number of scatterers at the T_x and the R_x. The statistical properties

of our simulation model are verified by comparison with the corresponding statistical properties of the reference model.

The remainder of this chapter is organized as follows: Section 7.2 introduces the 2-D geometrical concentric-sectors model and presents the parametric reference model that employs the geometry to develop the time-invariant transfer function for short-range THz multipath fading channels. Section 7.3 derives the FCF and the PDP for a 2-D isotropic scattering environment and provides a comparison between the measured and theoretical PDP's. Section 7.4 details the statistical SoS simulation model. Finally, a few concluding remarks are given in Section 7.5.

7.2 A Reference Model for Device-to-Device Wideband sub-THz Channels

The formulation of a reference model for short-range sub − THz device-to-device communication link between the stationary T_x and R_x is explained in detail in this section. Both the T_x and R_x are equipped with directional antennas, which is a requirement for sub-THz channels to compensate for the high path loss. The radio propagation in indoor environments is characterized by 2-D wide sense stationary uncorrelated scattering (WSSUS) with either LoS or NLoS conditions between the T_x and R_x.

Figure 62 shows the concentric-sectors model with LoS, SR, and DR rays. Concentric sectors are chosen to include antenna directionality and wideband channel characteristics into the model. In Fig. 62, A_T and A_R denote the locations of the T_x and R_x antennas and their separation distance is denoted by D. The scatterers are located along the arcs of the sectors centered at either A_T or A_R, with the radius R_t and R_r, respectively. The lower-bound of the R_t, R_{t1} is set in the far-field region of the T_x antenna, and the upper-bound, R_{t2} is set behind the R_x. Similarly, the lower-bound of the R_r, R_{r1} is set in the far-field region of the R_x antenna, and the upper-bound, R_{r2} is set behind the T_x. It is assumed that M fixed omnidirectional

scatterers occupy an area between the sectors of radii R_{t1} and R_{t2}. These M omni-directional scatterers lie on L arcs of radii $R_{t1} \leq R_t^{(l)} \leq R_{t2}$, where $1 \leq l \leq L$. To account for clustering effect, the l^{th} arc contains $M^{(l)}$ fixed omni-directional scatterers, and the $(l,m)^{th}$ scatterer is denoted by $S^{(l,m)}$, where $1 \leq m \leq M^{(l)}$. Similarly, Q scatterers lie on P arcs of radii $R_{r1} \leq R_r^{(p)} \leq R_{r2}$, where $1 \leq p \leq P$. The p^{th} arc contains $Q^{(p)}$ fixed omni-directional scatterers and the $(p,q)^{th}$ scatterer is denoted by $S^{(p,q)}$, where $1 \leq q \leq Q^{(p)}$.

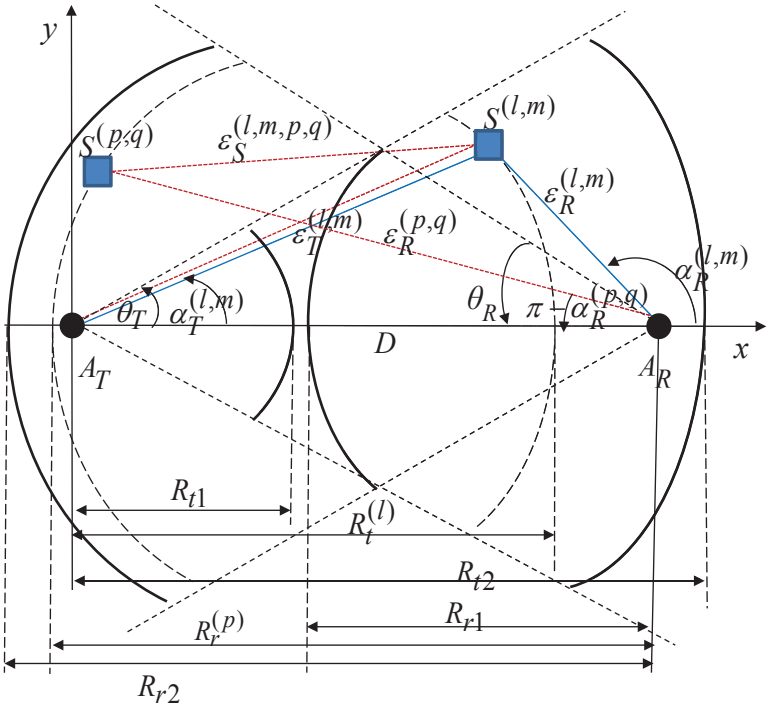

Figure 62: The concentric-sectors model with LoS , SR, and DR rays for a short-range wideband sub-THz device-to-device channel.

In Fig. 62, the angles θ_T and θ_R denote the half-beamwidths of the $\mathrm{T_x}$ and $\mathrm{R_x}$ antennas, respectively, relative to the x-axis. The propagation path lengths $\epsilon_T^{(l,m)}$, $\epsilon_R^{(l,m)}$, $\epsilon_S^{(l,m,p,q)}$, and $\epsilon_R^{(p,q)}$ correspond to the distances $A_T - S^{(l,m)}$, $S^{(l,m)} - A_R$, $S^{(l,m)} - S^{(p,q)}$ $S^{(p,q)} - A_R$, respectively, as shown in Fig. 62. Finally, the symbol $\alpha_T^{(l,m)}$ represents the angle of departure (AoD) of the ray that impinges on the scatterer $S^{(l,m)}$, while $\alpha_R^{(l,m)}$ denotes the angle of arrival (AoA) of the ray that reflects off $S^{(l,m)}$. On the other hand, the AoA of the ray that arrives after bouncing off $S^{(l,m)}$ and $S^{(p,q)}$, i.e., the

double-reflected ray, is denoted by $\alpha_R^{(p,q)}$. All the parameters used in the geometrical model are summarized in Table 13.

Table 13: Definition of the Parameters used in the Concentric-Sectors Geometrical Model.

D	Distance between the centers of Tx and Rx sectors
$R_t^{(l)}$	Radius of the lth sector with its center at Tx.
$R_r^{(p)}$	Radius of the pth sector with its center at Rx.
θ_T, θ_R	Half-beamwidths of the Tx and Rx antennas in the x-y plane (relative to x-axis), respectively.
R_{t1}, R_{t2}	minimum and maximum radii of the sectors with centers at Tx
R_{r1}, R_{r2}	minimum and maximum radii of the sectors with centers at Rx
$\alpha_T^{(l,m)}, \alpha_T^{(p,q)}$	Azimuth angels of departure (AAoD) of the waves that impinge on the scatterers $S^{(l,m)}$and $S^{(p,q)}$, respectively.
$\alpha_R^{(l,m)}, \alpha_R^{(p,q)}$	Azimuth angels of arrival (AAoA) of the waves scattered from the scatterers $S^{(l,m)}$ and $S^{(p,q)}$, respectively.
$\varepsilon_T^{(l,m)}$	Distance $d(A_T, S^{(l,m)})$
$\varepsilon_R^{(l,m)}$	Distance $d(S^{(l,m)}, A_R)$
$\varepsilon_R^{(p,q)}$	Distance $d(S^{(p,q)}, A_R)$
$\varepsilon_S^{(l,m,p,q)}$	Distance $d(S^{(l,m)}, S^{(p,q)})$

It is observed from the 2-D geometrical model in Fig. 62 that there exist three ray components in the channel: a ray that traverses directly from the T_x to the R_x antenna (LoS component), a ray that impinges upon the scatterers $S^{(l,m)}$ in the R_x sector area before arriving at the R_x antenna (Single-Reflected component), and/or a ray that reflects off the scatterers $S^{(l,m)}$ in the R_x sector area and, subsequently, scatters from the scatterers $S^{(p,q)}$ in the T_x sector area before arriving at the R_x antenna (Double-Reflected component). Hence, the time-invariant input delay-spread function of the link A_T - A_R can be written as a superposition of the LoS, SR, and DR rays, viz.

$$h(t,\tau) \;=\; h^{SR}(t,\tau) + h^{DR}(t,\tau) + h^{LoS}(t,\tau). \tag{38}$$

Note that the channel considered in this thesis is stationary, and therefore, t in (38) will be omitted in further equations.

The single-reflected component of the input delay-spread function is

$$h^{SR}(\tau) \;=\; \sqrt{\frac{\eta_{SR}}{K+1}} \lim_{M\to\infty} \frac{1}{\sqrt{M}} \sum_{l=1}^{L} \sum_{m=1}^{M^{(l)}} A_{l,m} e^{j\phi_{l,m}} \delta(\tau - \tau_{l,m}), \tag{39}$$

where $A_{l,m}$, $\phi_{l,m}$, and $\tau_{l,m}$ are the amplitude, the phase, and the time delay of the multipath components and they are defined as in [75]. Parameter K is the Rice factor (ratio of LoS to scatter received power).

The double-bounced component of the input delay-spread function is defined as

$$h^{DR}(\tau) = \sqrt{\frac{\eta_{DR}}{K+1}} \lim_{M,Q\to\infty} \frac{1}{\sqrt{MQ}} \sum_{l,m=1}^{L,M^{(l)}} \sum_{p,q=1}^{P,Q^{(p)}} A_{l,m,p,q} e^{\phi_{l,m,p,q}} \delta(\tau - \tau_{l,m,p,q}), \quad (40)$$

where $A_{l,m,p,q}$, $\phi_{l,m,p,q}$, and $\tau_{l,m,p,q}$ are the amplitude, the phase, and the time delay of the multipath components and they are defined as in [75]. The parameters, η_{SR} and η_{DR} in (39) and (40), quantify the relative powers allocated to the Single- and Double-Reflected rays, respectively, such that their sum equals 1 (i.e., $\eta_{SR} + \eta_{DR} = 1$). It is assumed that the angles of departure, $\alpha_T^{(l,m)}$, the angles of arrival, $\alpha_R^{(p,q)}$, and the radii, $R_t^{(l)}$ and $R_r^{(p)}$, are independent random variables. Furthermore, it is assumed that the phases, $\phi_{l,m}$, $\phi_{p,q}$, and $\phi_{l,m,p,q}$, are uniform random variables on the interval $[-\pi, \pi)$ and are independent from the angles of departure, the angles of arrival, and the radii of the sectors. Note that, for double-reflected rays, the AoA's, $\alpha_R^{(p,q)}$, are independent from the AoD's, $\alpha_T^{(l,m)}$ [108], while single-reflected rays have AoA's, $\alpha_R^{(l,m)}$, that are dependent on the AoD's, $\alpha_T^{(l,m)}$, and vice versa.

The LoS component of the input delay-spread function is

$$h^{LoS}(\tau) = \sqrt{\frac{K}{K+1}} A_{LoS} e^{j\phi_{LoS}} \delta(\tau - \tau_{LoS}), \quad (41)$$

where the LoS amplitude, A_{LoS}, and the LoS time delay, τ_{LoS}, are defined as in [75].

Finally, we observe that the distances $\epsilon_T^{(l,m)}$, $\epsilon_R^{(l,m)}$, $\epsilon_S^{(l,m,p,q)}$, and $\epsilon_R^{(p,q)}$ can be expressed as functions of the random variables $\alpha_T^{(l,m)}$, $\alpha_R^{(p,q)}$, $R_t^{(l)}$, and $R_r^{(p)}$ as follows:

$$\epsilon_T^{(l,m)} = R_t^{(l)} \quad (42)$$

$$\epsilon_R^{(l,m)} = \frac{R_t^{(l)} \cos\alpha_T^{(l,m)} - D}{\cos\left[\tan^{-1}\left(-\frac{R_t^{(l)} \sin\alpha_T^{(l,m)}}{D - R_t^{(l)} \cos\alpha_T^{(l,m)}}\right) + \pi\right]}, \quad (43)$$

$$\epsilon_S^{(l,m,p,q)} = \Bigg[\left| R_t^{(l)} \sin\alpha_T^{(l,m)} - R_r^{(p)} \sin\alpha_R^{(p,q)} \right|^2 + \left| R_t^{(l)} \cos\alpha_T^{(l,m)} - R_r^{(p)} \cos\alpha_R^{(p,q)} - D \right|^2 \Bigg]^{1/2}, \quad (44)$$

$$\epsilon_R^{(p,q)} = R_r^{(p)}. \quad (45)$$

The derivations of (43) and (44) are presented in Appendix B.

Since the locations of scatterers within an antenna radiation sector are equally probable, we assume uniformly distributed scattering in the concentric-sectors model and to characterize it we use the joint probability density function (pdf)

$$f(R,\alpha) = \frac{2R}{(\alpha_2-\alpha_1)(R_2^2-R_1^2)}. \quad (46)$$

The radii, $R_t^{(l)}$ and $R_r^{(p)}$, are uniformly distributed between R_{t1} and R_{t2}, and R_{r1} and R_{r2}, respectively. Similarly, the AoD's, $\alpha_T^{(l,m)}$, and the AoA's, $\alpha_R^{(p,q)}$, are uniformly distributed between $(2\pi-\theta_T)$–θ_T and $(\pi-\theta_R)$–$(\pi+\theta_R)$, respectively. Such a distribution implies that the scatterers in the horizontal plane will have a uniform density between the concentric-sectors, if the scattering is isotropic in the horizontal plane.

To simplify further analysis, we use the time-invariant transfer function instead of the input delay-spread function and we normalize the gain patterns of the antenna elements to unity, although other gain patterns can be accommodated at this point. The time-invariant transfer function is the Fourier transform of the input delay-spread function [108] and can be written as

$$T(f) = \mathcal{F}_\tau\{h(\tau)\} = T^{SR}(f) + T^{DR}(f) + T^{LoS}(f), \quad (47)$$

where $T^{SR}(f)$ is the SR, $T^{DR}(f)$ is the DR, and $T^{LoS}(f)$ is the LoS component of the time-invariant transfer function. The expressions for $T^{SR}(f)$, $T^{DR}(f)$, and $T^{LoS}(f)$ are derived in Appendix C.

7.3 Frequency Correlation Function and Power Delay Profile of the Reference Model

The correlation function is an important statistic in designing communication links that characterizes how fast a wireless channel changes with time, movement, or in frequency. For example, if the correlation stays high for a long time, in a case of strong channel attenuation, multiple symbols will be similarly affected implying that error correction codes will not be able to repair damage. These statistics enable the system designer to make informed decisions when choosing modulation, interleaving, and coding schemes at the transmitting end and the type of channel estimator and decoder at the receiving end. The specific correlation function that is of interest in this chapter is the frequency correlation function (FCF), which measures the channel's frequency selectivity. In other words, the FCF is a useful indicator of dependencies as a function of difference in frequency (Δf), and it can be used to access the required frequency difference between sample points for the values to be effectively uncorrelated.

The normalized frequency auto-correlation function of the time-invariant transfer function is defined as

$$R(\Delta f) = \frac{E[T(f)^* T(f+\Delta f)]}{\sqrt{\mathrm{Var}[T(f)^*]\mathrm{Var}[T(f+\Delta f)]}}, \tag{48}$$

where $(\cdot)^*$ denotes the complex conjugate operation, E$[\cdot]$ is the statistical expectation operator, and Var$[\cdot]$ is the statistical variance operator.

Since $T^{SR}(f)$, and $T^{DR}(f)$ are independent zero-mean complex Gaussian random processes, (48) can be simplified to

$$R(\Delta f) \;=\; R^{SR}(\Delta f) + R^{DR}(\Delta f) + R^{LoS}(\Delta f), \tag{49}$$

where $R^{SR}(\Delta f)$, $R^{DR}(\Delta f)$, and $R^{LoS}(\Delta f)$ denote the normalized FCFs of the SR,

DR, and LoS components, respectively, and are defined as

$$R^{SR}(\Delta f) = \frac{\mathrm{E}\left[T^{SR}(f)^{*}T^{SR}(f+\Delta f)\right]}{\Omega}, \tag{50}$$

$$R^{DR}(\Delta f) = \frac{\mathrm{E}\left[T^{DR}(f)^{*}T^{DR}(f+\Delta f)\right]}{\Omega}, \tag{51}$$

$$R^{LoS}(\Delta f) = \frac{\mathrm{E}\left[T^{LoS}(f)^{*}T^{LoS}(f+\Delta f)\right]}{\Omega}, \tag{52}$$

where $\Omega = D^{-\gamma/2}\sqrt{G_T G_R}\lambda/4\pi$.

Since the number of local scatterers in the reference model described in Section 7.2 is infinite, the discrete AoD's $\alpha_T^{(l,m)}$, AoA's $\alpha_R^{(p,q)}$, and radii $R_t^{(l)}$ and $R_r^{(p)}$ can be replaced with continuous random variables α_T, α_R, R_t, and R_r with probability density functions (pdf) $f(\alpha_T)$, $f(\alpha_R)$, $f(R_t)$, and $f(R_r)$, respectively.

Substituting (88) into (52), the $R^{LoS}(\Delta f)$ becomes

$$R^{LoS}(\Delta f) = \frac{K}{K+1}\, e^{-j\frac{2\pi}{c_0}\Delta f D}. \tag{53}$$

Similarly, substituting (86) into (50) and (87) into (51), the $R^{SR}(\Delta f)$ and $R^{DR}(\Delta f)$ can be written as (54) and (55) (appearing on page 121), respectively. Note that the FCFs for the SR and DR components of the time-invariant transfer function must be evaluated numerically because the integrals in (54) and (55) do not have closed-form solutions. While it is difficult to obtain closed-form solutions, we show in Appendix D how the $R^{SR}(\Delta f)$ and the $R^{DR}(\Delta f)$ expressions can be approximated by

$$\begin{aligned} R^{SR}(\Delta f) \approx\ & \frac{2}{(\alpha_{T2}-\alpha_{T1})(R_{t2}^2-R_{t1}^2)}\frac{\eta_{SR}}{K+1}\int_{R_{t1}}^{R_{t2}} R_t\, e^{-j\frac{2\pi}{c_0}\Delta f(R_t+D)} \\ & \times \int_{\alpha_{T1}}^{\alpha_{T2}} \frac{1}{1+\gamma\frac{R_t}{D}(1-\cos\alpha_T)} e^{-j\frac{2\pi}{c_0}\Delta f R_t\cos\alpha_T} d\alpha_T\, dR_t, \end{aligned} \tag{56}$$

$$\begin{aligned} R^{DR}(\Delta f) \approx\ & \frac{4}{(\alpha_{T2}-\alpha_{T1})(\alpha_{R2}-\alpha_{R1})(R_{t2}^2-R_{t1}^2)(R_{r2}^2-R_{r1}^2)}\frac{\eta_{DR}}{K+1} \\ & \times \int_{R_{r1}}^{R_{r2}} R_r\, e^{-j\frac{2\pi}{c_0}\Delta f R_r}\int_{\alpha_{R1}}^{\alpha_{R2}} e^{-j\frac{2\pi}{c_0}\Delta f R_r\cos\alpha_R}\int_{R_{t1}}^{R_{t2}} R_t\, e^{-j\frac{2\pi}{c_0}\Delta f R_t} \\ & \times \int_{\alpha_{T1}}^{\alpha_{T2}} \frac{e^{j\frac{2\pi}{c_0}\Delta f(R_t\cos\alpha_T)}}{1+\gamma\left(\frac{R_t}{D}(1-\cos\alpha_T)+\frac{R_r}{D}(1+\cos\alpha_R)\right)} \\ & \times d\alpha_T dR_t d\alpha_R dR_r, \end{aligned} \tag{57}$$

$$R^{SR}(\Delta f) = \mathrm{E}\left[\frac{\eta_{SR}}{K+1}\frac{D^{\gamma}}{\left(R_t + \frac{R_t\cos\alpha_T - D}{\cos\left[\tan^{-1}\left(-\frac{R_t\sin\alpha_T}{D-R_t\cos\alpha_T}\right)+\pi\right]}\right)^{\gamma}}\ e^{-j2\pi\Delta f\tau_{SR}}\right]$$

$$= \frac{\eta_{SR}}{K+1}\int_{R_{t1}}^{R_{t2}}\int_{\alpha_{T1}}^{\alpha_{T2}}\frac{D^{\gamma}}{\left(R_t + \frac{R_t\cos\alpha_T - D}{\cos\left[\tan^{-1}\left(-\frac{R_t\sin\alpha_T}{D-R_t\cos\alpha_T}\right)+\pi\right]}\right)^{\gamma}}e^{-j2\pi\Delta f\tau_{SR}}$$

$$\times\ f(R_t)f(\alpha_T)d\alpha_T\ dR_t$$

$$= \frac{2D^{\gamma}}{(\alpha_{T2}-\alpha_{T1})(R_{t2}^2-R_{t1}^2)}\frac{\eta_{SR}}{K+1}\int_{R_{t1}}^{R_{t2}}\int_{\alpha_{T1}}^{\alpha_{T2}}\frac{R_t}{\left(R_t + \frac{R_t\cos\alpha_T - D}{\cos\left[\tan^{-1}\left(-\frac{R_t\sin\alpha_T}{D-R_t\cos\alpha_T}\right)+\pi\right]}\right)^{\gamma}}$$

$$\times\ e^{-j\frac{2\pi}{c_0}\Delta f\left(R_t+\frac{R_t\cos\alpha_T - D}{\cos\left[\tan^{-1}\left(-\frac{R_t\sin\alpha_T}{D-R_t\cos\alpha_T}\right)+\pi\right]}\right)}d\alpha_T\ dR_t, \tag{54}$$

$$R^{DR}(\Delta f) = \frac{\eta_{DR}}{K+1}$$

$$\mathrm{E}\left[\frac{D^{\gamma}e^{-j2\pi\Delta f\tau_{DR}}}{\left(R_t + R_r + \sqrt{|R_t\sin\alpha_T - R_r\sin\alpha_R|^2 + |R_t\cos\alpha_T - R_r\cos\alpha_R - D|^2}\right)^{\gamma}}\right]$$

$$= \frac{\eta_{DR}}{K+1}\int_{R_{r1}}^{R_{r2}}\int_{R_{t1}}^{R_{t2}}\int_{\alpha_{R1}}^{\alpha_{R2}}\int_{\alpha_{T1}}^{\alpha_{T2}}$$

$$\frac{D^{\gamma}e^{-j2\pi\Delta f\tau_{DR}}f(R_t,\alpha_T,R_r,\alpha_R)}{\left(R_t + R_r + \sqrt{|R_t\sin\alpha_T - R_r\sin\alpha_R|^2 + |R_t\cos\alpha_T - R_r\cos\alpha_R - D|^2}\right)^{\gamma}}$$

$$\times\ d\alpha_T\ d\alpha_R\ dR_t\ dR_r$$

$$= \frac{4D^{\gamma}}{(\alpha_{T2}-\alpha_{T1})(\alpha_{R2}-\alpha_{R1})(R_{t2}^2-R_{t1}^2)(R_{r2}^2-R_{r1}^2)}\frac{\eta_{DR}}{K+1}\int_{R_{r1}}^{R_{r2}}\int_{R_{t1}}^{R_{t2}}\int_{\alpha_{R1}}^{\alpha_{R2}}\int_{\alpha_{T1}}^{\alpha_{T2}}$$

$$\frac{R_tR_r}{\left(R_t + R_r + \sqrt{|R_t\sin\alpha_T - R_r\sin\alpha_R|^2 + |R_t\cos\alpha_T - R_r\cos\alpha_R - D|^2}\right)^{\gamma}}$$

$$\times\ e^{-j\frac{2\pi}{c_0}\Delta f\left(R_t+R_r+\sqrt{|R_t\sin\alpha_T - R_r\sin\alpha_R|^2+|R_t\cos\alpha_T - R_r\cos\alpha_R - D|^2}\right)}$$

$$\times\ d\alpha_T\ d\alpha_R\ dR_t\ dR_r. \tag{55}$$

respectively.

To validate assumptions used to obtain the approximated FCFs in (56) and (57), we compare these equations with the numerically obtained FCFs in (54) and (55). Figures 63 and 64 compare the exact and approximated frequency correlation functions for SR and DR components. Two different scatterer positions defined by the parameters, R_{t1}, R_{t2}, R_{r1}, R_{r2}, and θ_T (or θ_R) have been selected: the scenario, $R_{t1} = R_{r1} = 0$ m, $R_{t2} = R_{r2} = 0.11$ m, and $\theta_T = \theta_R = 45°$, is shown in Fig. 63; and the scenario $R_{t1} = R_{r1} = 0.2$ m, $R_{t2} = R_{r2} = 0.3$ m, and $\theta_T = \theta_R = 30°$ is shown in Fig. 64. The T-R separation distance, D, is set to 0.3 m for both scenarios.

The mismatch between exact and approximated frequency correlation functions observed in Fig. 63 and 64 comes from the discrepancy between the exact (Eq. (43), (44)) and approximated (Eq. (89), (90)) expressions for the path lengths, i.e., $\epsilon_R^{(l,m)}$ and $\epsilon_S^{(l,m,p,q)}$ (please refer to Appendix D). Specifically, for SR rays, the criterion that can approximate (43) with (89) is

$$\frac{R_t \sin\alpha_T}{D - R_t \cos\alpha_T} << 1 \tag{58}$$

Therefore, the accuracy of the approximation, for SR rays, depends on the degree to which the condition (58) is true. For Fig. 63, the maximum value of $\frac{R_t \sin\alpha_T}{D - R_t \cos\alpha_T}$ is 0.35. While it is smaller than 1, the value is still not small enough to satisfy (58), which is why there exists mismatch between the exact and approximated correlation functions in Fig. 63. On the other hand, in the case of Fig. 64, the maximum value of $\frac{R_t \sin\alpha_T}{D - R_t \cos\alpha_T}$ is 3.7321, which does not satisfy the condition at all. As a result, we can observe that the approximated correlation function for SR component has a completely different shape compared to the exact one in Fig. 64. Meanwhile, for DR rays, the assumption that approximates (44) with (90) is

$$|R_t^{(l)} \sin\alpha_T^{(l,m)} - R_r^{(p)} \sin\alpha_R^{(p,q)}|^2 = 0, \tag{59}$$

such that the first term of (44), which is the projection of $\epsilon_s^{(l,m,p,q)}$ onto y-axis, cancels

out. In Fig. 63, the geometry of the scenario described by the parameters, $R_{t1} = R_{r1} = 0$ m, $\mathrm{R_{t2}} = \mathrm{R_{r2}} = 0.1$ m, and $\theta = 45°$, allows for a margin of error since there exists a chance that $|R_t^{(l)} \sin \alpha_T^{(l,m)} - R_r^{(p)} \sin \alpha_R^{(p,q)}|^2 > 0$ due to large beamwidth ($\theta = 45°$). This explains the slight mismatch between the exact and approximated correlation functions for DR component in Fig. 63. On the other hand, in Fig. 64, where the parameters are $R_{t1} = R_{r1} = 0.2$ m, $R_{t2} = R_{r2} = 0.3$ m, and $\theta = 30°$, smaller beamwidth forces the y-projections of $\epsilon_s^{(l,m,p,q)}$ closer to 0. Therefore, the degree to which (59) is true is much higher in this case, and consequently, a much better match between the exact and approximated correlation functions is observed for DR component in Fig. 64, compared to that in Fig. 63. Note that the benefit of the approximated expressions for correlation functions is a quick estimate of channel's frequency selectivity, and the exact correlation functions can be numerically obtained if more precise results are needed.

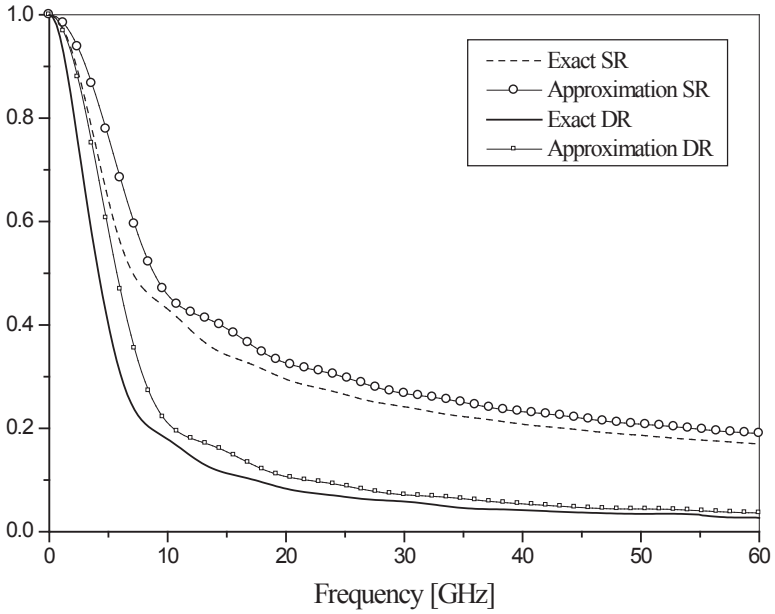

Figure 63: The exact and approximated frequency correlation functions for SR and DR components when $R_{t1} = R_{r1} = 0$ m, $R_{t2} = R_{r2} = 0.11$ m, $\theta_T = \theta_R = 45°$.

The power delay profile (PDP) of the proposed model can be obtained by taking

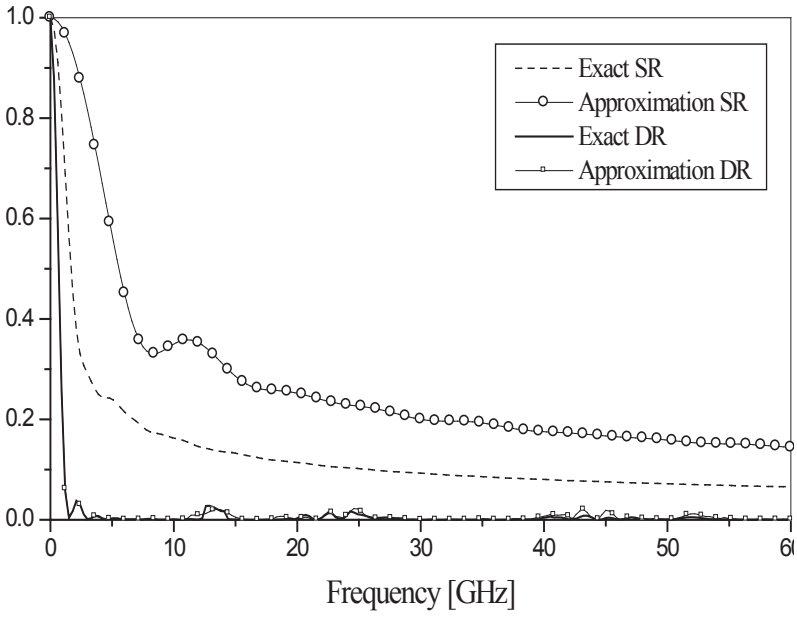

Figure 64: The exact and approximated frequency correlation functions for SR and DR components when $R_{t1} = R_{r1} = 0.2$ m, $R_{t2} = R_{r2} = 0.3$ m, $\theta_T = \theta_R = 30°$.

the Inverse Fourier Transform of the FCF [108], i.e.,

$$P(\tau) = \mathcal{F}_{\Delta f}^{-1}\{R(\Delta f)\}. \tag{60}$$

The significance of PDP is that it gives the intensity of a received signal as a function of time delay, and is useful in identifying multipaths in the channel. Also, PDPs are used to extract important parameters, such as RMS delay spread (and coherence bandwidth of the channel), which is a measure of time dispersion or frequency selectivity, and tell system designer how long it has to wait before next symbol can be sent to avoid inter-symbol interference.

To verify the validity of the proposed model, the theoretical PDPs are compared to the measured ones. The measurement data has been collected at two sub-THz frequency ranges, i.e., at $f_c = 300$ GHz with 20 GHz of bandwidth [67], [73] and at D-band ($110 - 170$ GHz) [69]. Specifically, measurements at 300 GHz are analyzed for LoS desktop scenarios [67], realistic desktop environments with objects, such as

books, cell phones, and laptops, and a computer motherboard environment with a RAM module. Also, in D-band, measurements for an NLoS desktop scenario with a cylindrical obstruction [69] are used to validate the proposed model.

For the 300 GHz desktop LoS measurement campaign [67], two T-R separation distances, D, of 30 cm and 40 cm have been considered, and the T_x and R_x were equipped with horn antennas with beamwidths of 10°, i.e., $2\theta_T = 2\theta_R = 10°$. The T_x and R_x, as well as any surrounding objects, were stationary, meaning the channel was quasi-static with no time-dependence. Although the channel environment was free of local scatterers, the metallic surfaces of the T_x and R_x test heads, on which the horn antennas are attached, acted as reflectors. Consequently, the signal transmitted from the T_x travelled the separation distance, D, got reflected off the R_x test head, travelled back the distance, D, towards the T_x, reflected again off the T_x test head, and finally, arrived at the R_x after traversing the distance, D. This implies that even though no scatterers were present in the environment, multiple rays have been reflected off the metallic transceiver box and created multiple scattering rays in the channel, introducing double-reflected rays in addition to the direct LoS ray. The arrivals of these double-reflected paths are apparent in the measured PDPs shown in Figs. 65(a) and 65(b). The excess delays of the double-reflected rays correspond to the rays that travelled double the separation distance, which is why the peaks in the PDPs shift to the right as the distance increases.

In the reference model, parameter K is estimated using the method in [118] to be 0.4 for all distances. Since there are no single reflections in the channel, setting the parameters η_{SR} and η_{DR} was straight forward, i.e., $\eta_{SR} = 0$ and $\eta_{DR} = 1$. The parameters R_{t1}, R_{r1}, R_{t2}, and R_{r2} are estimated using method in [119] as: $R_{t1} = R_{r1} =$ 32 cm and $R_{t2} = R_{r2} = 33$ cm for $D = 30$ cm (Fig. 65(a)), and $R_{t1} = R_{r1} = 42$ cm and $R_{t2} = R_{r2} = 43$ cm for $D = 40$ cm (Fig. 65(b)), respectively.

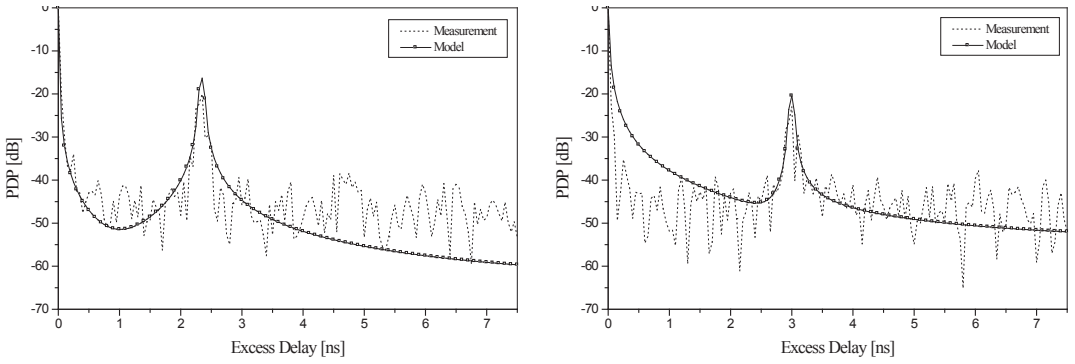

Figure 65: The normalized theoretical and measured power delay profiles for the 300 GHz desktop LoS scenarios: (a) D = 30 cm (b) D = 40 cm.

Figures 65(a) and 65(b) show that the proposed model captures well the amplitudes and the excess delays of the LoS and double-reflected multipath components for the two distances. Measurements indicate that the signal power drops to a negligible level after bouncing off the test head surfaces multiple times. Hence, it is sufficient for the reference model to include only the single and double-reflected multipath components. Note that a mismatch between the modelled and measured PDPs is observed towards larger excess delays because the measurement has reached its noise floor, while the model does not take into account the noise threshold of the receiver.

In addition to LoS desktop scenario, we also compare our measured and modelled PDPs in a more realistic device-to-device communication scenario shown in Fig. 66(a), where different objects, such as a book, a phone, a stack of paper, and a laptop, are placed on a desk to obstruct the LoS between the T_x and the R_x. Figure 66(b) presents the modelled and measured PDPs for the measurement setup of Fig. 66(a). The T-R separation, D, is 55 cm, and other parameters are estimated using the methods from [118] and [119] as follows: $K = 0.5$, $\eta_{SR} = 0.3$, and $\eta_{DR} = 0.7$, $R_{t1} = R_{r1} = 10$ cm, and $R_{t2} = R_{r2} = 50$ cm. The random variables, R_t, R_r, α_T, and α_R, are assumed to be uniformly distributed with the joint pdf of (46), and it has been proven that this assumption is valid for the realistic desktop propagation environment with cluttered

scatterers by observing a good match between the theoretical and measured PDPs in Fig. 66(b).

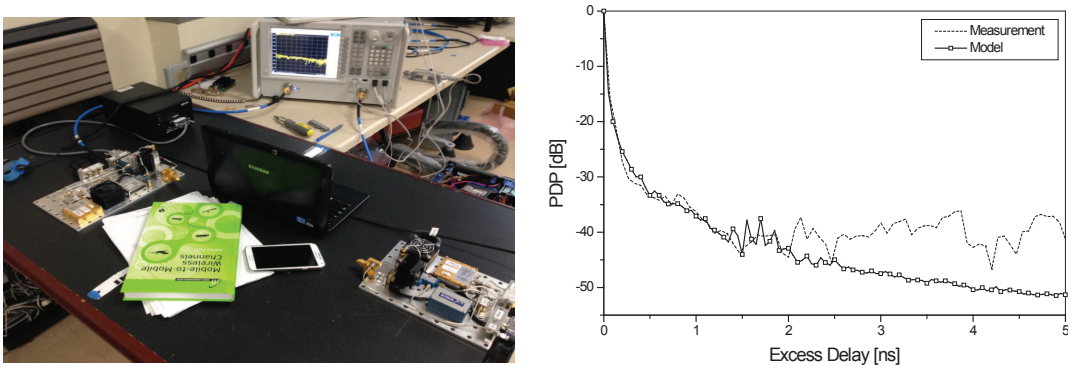

(a) (b)

Figure 66: Realistic 300 GHz device-to-device desktop scenario with clutter: (a) Measurement setup and (b) Comparison of measured and modelled PDP's.

Another potential THz application is chip-chip communication, where ultra-wideband channels over short distances are required. To illustrate validity of our model, we compare our modeled PDP with the measured one for an NLoS scenario in a computer motherboard environment, where a RAM module (DIMM) is placed perpendicularly at the midpoint of the T-R separation distance, 23.5 cm, blocking the LoS. The measurement setup and the PDPs are presented in Figs. 67(a) and 67(b), respectively. The measured PDP shown in Fig. 67(b) shows two distinct paths reaching the R_x, i.e., at $\tau = 0$ ns $\tau = 0.93$ ns. From the fact that the backside of the DIMM is metallic, it can be concluded that the first arriving path at $\tau = 0$ ns is the path that diffracts off the top edge of the RAM (i.e. a single-reflected ray). On the other hand, considering the geometry of the setup and the excess delay of 0.93 ns of the second arriving path, it is reasonable to assume that the second path is the result of two consecutive reflections off the R_x back panel and the back side of the DIMM (i.e. double-reflected rays). The modelled PDP in Fig. 67(b), which accurately predicts the excess delay and amplitude of the second arriving path, is produced with the

following parameters: $K = 0$, $\eta_{SR} = 0.45$, $\eta_{DR} = 0.55$, $D = 23.5$ cm, $R_{t1} = 25.5$ cm, $R_{t2} = 26.5$ cm, $R_{r1} = 11$ cm, and $R_{r2} = 12$ cm. As before, the estimation of K is based on the method from [118], while that of other parameters are estimated using the method in [119]. The Rician factor, K, of 0 agrees with intuition since there is no LoS path in this scenario, and the estimated contribution factors, η_{SR}, η_{DR}, reveal that the DR rays have slightly higher contribution to the total received power than the SR rays.

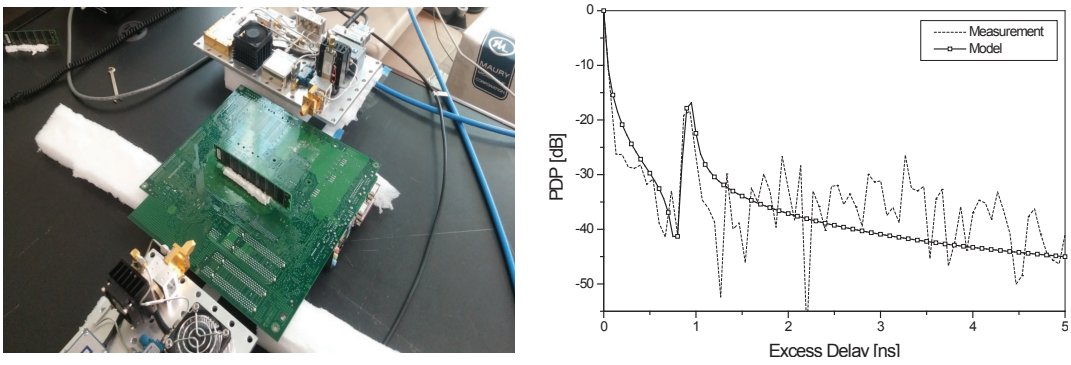

(a) (b)

Figure 67: 300 GHz NLoS scenario in a computer motherboard environment with a RAM module (DIMM) as an obstruction: (a) Measurement setup and (b) Comparison of measured and modeled PDP's.

Finally, we compare measured and modelled PDPs in a NLoS scenario, where a cylindrical object, such as a coffee mug, obstructs the line of sight. The measurements are collected in D-band [69] with a coffee mug obstructing the LoS between the T_x and the R_x. The mug is placed at the midpoint of the T-R separation distance, i.e., $D = 35.56$ cm. The measurement setup is shown in Fig. 68(a). In [69], for this particular scenario, we have shown that the received power is a vector sum of LoS, convex-surface-diffracted rays (i.e., single-reflected rays), and the double-reflected rays (i.e., reflections inside the mug). For this scenario, the model parameters are estimated as follows: $K = 0.15$, $\eta_{SR} = \eta_{DR} = 0.5$, $R_{t1} = R_{r1} = 21.5$ cm, and $R_{t2} = R_{r2} = 22.5$ cm, using the methods from [118] and [119], respectively.

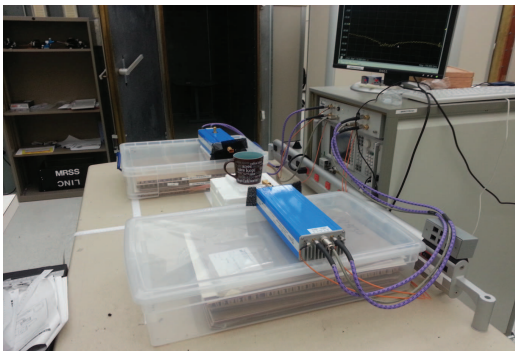

(a)

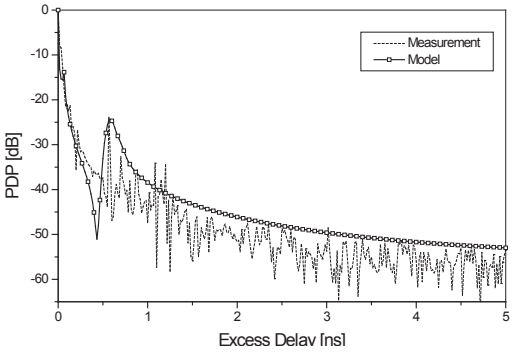

(b)

Figure 68: D-band desktop NLoS scenario with cylindrical obstruction: (a) Measurement setup and (b) Comparison of measured and modelled PDPs.

7.4 Simulation Model for Short-range Wideband sub-THz Channels

The reference model for short-range wideband sub-THz channels described in Section 7.2 assumes an infinite number of scatterers, which prevents practical implementation. It is desirable to design a simulation model with a finite (preferably small) number of scatterers, while still matching the statistical properties of the reference model.

The simulation model proposed in this chapter uses the statistical Sum-of-Sinusoids (SoS) method, which generates the channel waveform by superimposing a finite number of properly selected sinusoids [108], i.e., LoS, Single-Reflected (SR), and Double-Reflected (DR) components. Also, in this statistical SoS model, the parameter sets, (R_t, R_r) and (α_T, α_R), are left as random variables that vary with each simulation trial. Therefore, the statistical properties of the SoS model vary for each trial, but converge to the desired properties when averaged over a sufficient number of simulations.

Using the reference model in (38) with a finite number of scatterers and assuming 2-D isotropic scattering, the following function is considered for the received complex

faded envelope

$$h(\tau) = \sqrt{\frac{\eta_{SR}}{K+1}} \frac{1}{\sqrt{M}} \sum_{l=1}^{L} \sum_{m=1}^{M^{(l)}} A_{l,m} e^{j\phi_{l,m}} \delta(\tau - \tau_{l,m})$$
$$+ \sqrt{\frac{\eta_{DR}}{K+1}} \frac{1}{\sqrt{MQ}} \sum_{l,m=1}^{L,M^{(l)}} \sum_{p,q=1}^{P,Q^{(p)}} A_{l,m,p,q} e^{\phi_{l,m,p,q}} \delta(\tau - \tau_{l,m,p,q})$$
$$+ \sqrt{\frac{K}{K+1}} A_{LoS} e^{j\phi_{LoS}} \delta(\tau - \tau_{LoS}), \tag{61}$$

where amplitudes and delays of SR, DR, and LoS components are defined in [69]. It is assumed that the angles of departure ($\alpha_T^{(l,m)}$) and the angles of arrival ($\alpha_R^{(p,q)}$) are uniformly distributed random variables. They are realized as follows:

$$\alpha_T^{(l,m)} = \frac{(m + \psi_T - 1)(\alpha_{T2} - \alpha_{T1})}{M} + \alpha_{T1}, \tag{62}$$
$$\alpha_R^{(p,q)} = \frac{(q + \psi_R - 1)(\alpha_{R2} - \alpha_{R1})}{Q} + \alpha_{R1}, \tag{63}$$

for $l = 1, ..., L$, $m = 1, ..., M$, $p = 1, ..., P$, and $q = 1, ..., Q$. Furthermore, it is assumed that the radii $R_t^{(l)}$ and $R_r^{(p)}$ are uniformly distributed independent random variables implemented as follows:

$$R_t^{(l)} = \sqrt{\frac{(l + \sigma_T - 1)(R_{t2}^2 - R_{t1}^2)}{L} + R_{t1}^2}, \tag{64}$$
$$R_r^{(p)} = \sqrt{\frac{(p + \sigma_R - 1)(R_{r2}^2 - R_{r1}^2)}{P} + R_{r1}^2}, \tag{65}$$

for $l = 1, ..., L$, $m = 1, ..., M$, $p = 1, ..., P$, and $q = 1, ..., Q$. Finally, it is assumed that the phases $\phi_{l,m}$, $\phi_{p,q}$, and $\phi_{l,m,p,q}$ are uniform random variables on the interval $[-\pi, \pi)$ that are independent from the angles of departure, the angles of arrival, and the radii of the sectors. The parameters, σ_T, σ_R, ψ_T, and ψ_R, are independent random variables uniformly distributed on the interval [0,1), such that a 2-D isotropic scattering environment is ensured.

Figure 69 shows good agreement between the analytical and simulated correlation functions for the scenario modelled with the following parameters: $R_{t1} = R_{r1} = 0.16$ m, $R_{t2} = R_{r2} = 0.161$ m, $D = 0.3$ m, $\theta_T = \theta_R = 45°$, $K = 0.1$, $\eta_{SR} = 0.5$, and

$\eta_{DR} = 0.5$. The number of scatterers was $L = M = P = Q = 4$ and the correlation functions are averaged over $N_{stat} = 400$ simulation trials. Corresponding PDPs are compared in Figs. 70. The results show that the theoretical and simulated FCFs and PDPs have a good match over a wide range of time delays.

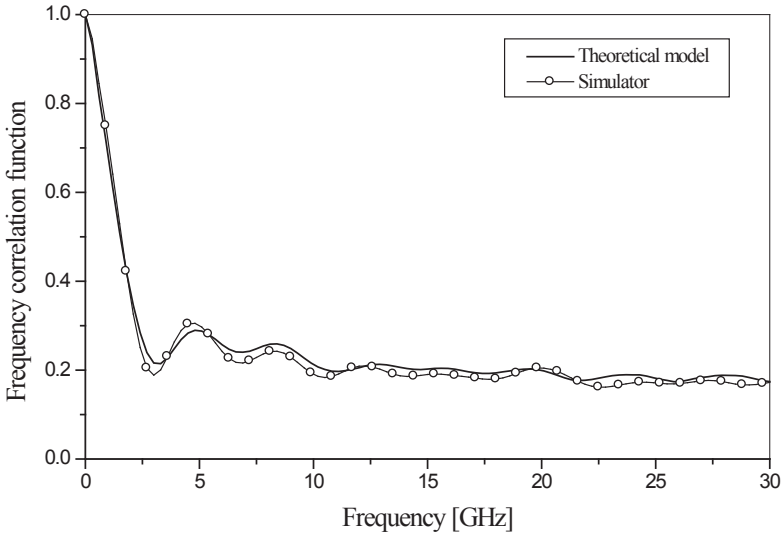

Figure 69: The theoretical and simulated frequency correlation functions for $R_{t1} = R_{r1} = 0.16$ m, $R_{t2} = R_{r2} = 0.161$ m, $\theta_T = \theta_R = 45°$, $K = 0.1$, $\eta_{SR} = 0.5$, $\eta_{DR} = 0.5$, and $L = M = P = Q = 4$

Finally, Fig. 71 presents the theoretical, measured, and simulated PDPs on the same plot for the realistic 300 GHz desktop scenario shown in Fig. 66(a). For simulation, the same parameters that have been estimated for the theoretical PDP are used, and the number of scatterers is set by the parameters, $L = M = P = Q = 6$. All three PDPs are in a good agreement, which confirms the validity of the reference model as well as the simulation model.

7.5 Summary

This chapter proposed a two-dimensional (2-D) geometrical propagation model for short-range sub-THz device-to-device communications. Based on the geometrical model, a parametric reference model for wideband sub-THz multipath fading channels

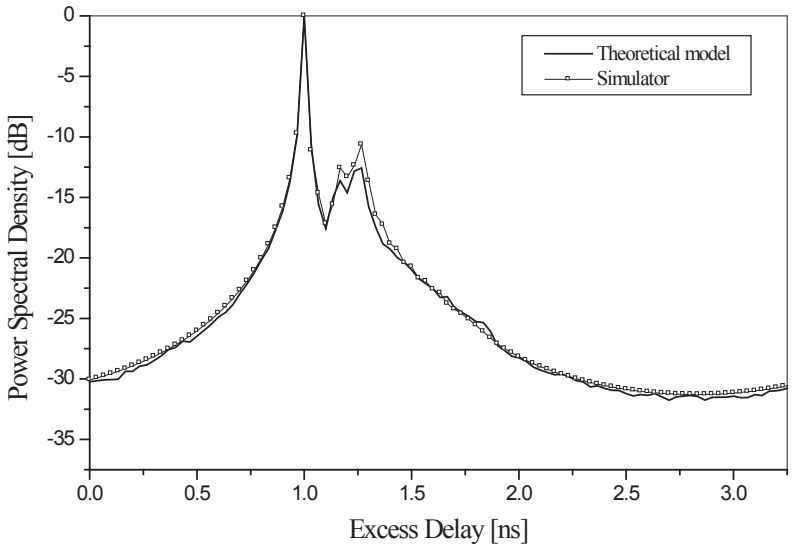

Figure 70: The theoretical and simulated power delay profiles for $R_{t1} = R_{r1} = 0.16$ m, $R_{t2} = R_{r2} = 0.161$ m, $\theta_T = \theta_R = 45°$, $K = 0.1$, $\eta_{SR} = 0.5$, $\eta_{DR} = 0.5$, and $L = M = P = Q = 4$

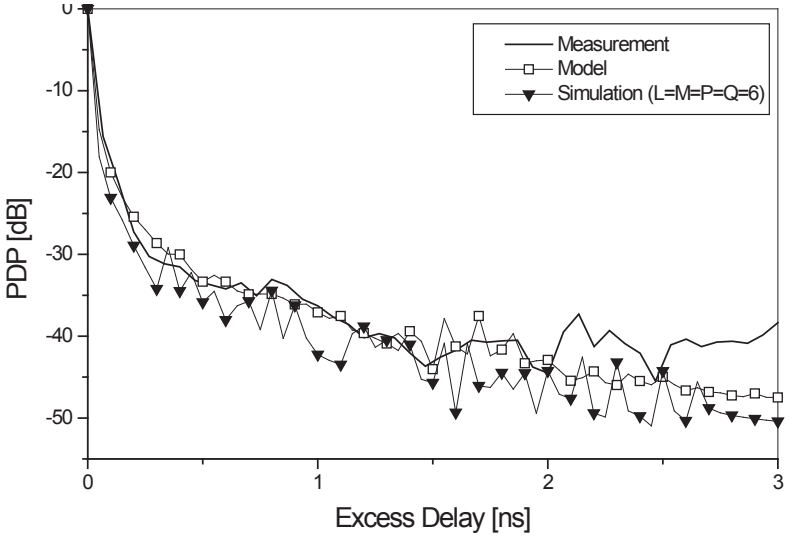

Figure 71: The measured, modelled, and simulated PDPs for the realistic 300-GHz desktop scenario shown in Fig. 66(a).

is developed. From the reference model, the corresponding FCF and PDP are derived and compared with measured data. The results show good agreement between the measured and theoretical PDPs. Finally, a new sum-of-sinusoids based simulation model for wideband sub-THz channels is proposed. The statistics of the reference

model are verified by simulation. The results show that the simulation model is a good approximation of the reference model.

CHAPTER VIII

EMPIRICAL COMPARATIVE ANALYSIS OF INDOOR PROPAGATION AT MM-WAVE AND THZ FREQUENCIES: 30 GHZ, 140 GHZ, AND 300 GHZ CHANNELS

8.1 Overview

While the THz band can offer an ultra-high data rate, the channel suffers from inherently high free-space path loss due to its dependence on frequency, and therefore, is limited in propagation distance. NLoS propagation is even more problematic at THz frequencies, unless it is directed, or guided, by reflections. It has been recently shown that new mm-Wave broadband cellular communication networks (5G) can be realized at frequencies 28 GHz and 38 GHz, where the available bandwidth is significantly less compared to THz bands (i.e., 1 GHz [65] vs. tens of GHz), with steerable directional antennas at base stations and mobile devices [65]. By moving down to a lower spectrum (i.e., mm-Wave band), where frequencies are more congested, the channel can cover a longer range in the LoS case, and undergo less penetration losses in an NLoS environment at the expense of bandwidth. Therefore, a topic that deserves attention is to investigate this trade-off between range and bandwidth through a comparative analysis of propagation mechanisms in mm-Wave channels and those in THz channels, which, to the best of author's knowledge, has not been reported in the open literature. We propose to compare the same indoor scenarios measured at D-band and 300 GHz with 30 GHz channel measurements.

Different path loss parameters and power delay profiles are expected for 30 GHz

channels because of the richer multipaths due to the wider beamwidth of the antennas and different reflection/penetration losses. Therefore, in this chapter, 30 GHz measurements in various indoor scenarios (e.g., LoS, OLoS, and RNLoS) are performed, and their characterization results in terms of path loss (i.e, path loss exponent and standard deviation) and multipath propagation (i.e, RMS delay spread and coherence bandwidth) are compared with those obtained for 300 GHz and D-band channels in Chapter 4 and 5.

The remainder of this chapter is organized as follows: Section 8.2 describes the equipment and the antennas used in the measurements, and Section 8.2.2 presents the measurement scenarios, in which 30 GHz, D-band, and 300 GHz are compared. Section 8.3 will provide the details of comparative analysis of the three frequency bands in terms of path loss, shadowing, and multipath propagation for each measurement scenario described in Section 8.2.2, and finally, Section 8.4 provides some concluding remarks.

8.2 Measurement Setup

The same equipment, namely, the N5224A PNA vector network analyzer, as in the 300 GHz measurement presented in Chapter 4 has been used for 30 GHz channels. In this measurement campaign, however, instead of the T_x and R_x modules that featured frequency converters and mixers, the input signal from the VNA is directly fed into the horn antenna. An input signal bandwidth of 13.5 GHz around the center frequency of 33.25 GHz (i.e., f = 26.5 GHz–40 GHz) is used. The input power level is 0 dBm, and an IF bandwidth of 100 kHz has been chosen, providing a dynamic range of approximately 80 dB. The number of sweep points is set to 801. All measurement parameters used in this chapter are summarized in Table 14.

Table 14: Measurement parameters.

Parameter	Symbol	Value
Measurement points	N	801
Intermediate frequency bandwidth	Δf_{IF}	100 kHz
Average noise floor	P_N	-82 dBm
Input signal power	P_{in}	0 dBm
Start frequency	f_{start}	26.5 GHz
Stop frequency	f_{stop}	40 GHz
Bandwidth	B	13.5 GHz
Time domain resolution	Δt	0.074 ns
Maximum excess delay	τ_m	59 ns

8.2.1 Antenna Characteristics

A WR28 pyramidal horn with gain that varies from 10 dBi at 26.5 GHz to 13.5 dBi at 40 GHz has been used. Both T_x and R_x antennas are vertically polarized and have HPBW of 56° in both the E-plane and H-plane at 26.5 GHz, and it decreases to 33° at 40 GHz. The antenna's VSWR is less than 1.3 at all frequencies.

Furthermore, the antennas have side-lobes that are at least 25 dB below the main beam at all frequencies of interest in the H-plane, while they can get as high as 15 dB in the E-plane between 36–37.5 GHz. The effect of these sidelobes is addressed in a RNLoS propagation environment, which will be presented later in this chapter.

8.2.2 Measurement Scenarios

For the purpose of comparative analysis, the 30 GHz wireless channels have been subject to the same measurement scenarios described in Section 5.2.3, namely, LoS, OLoS, and RNLoS. Due to much wider beamwidths of the antennas, however, the ground reflection was a greater concern for 30 GHz channels. Therefore, for the LoS measurement, as shown in Fig. 72(a), the T_x antenna has been fixed on the edge of a desk, while the R_x antenna has been mounted on a movable cabinet of equal height. Also, to suppress reflections from the metallic surface of the cabinet as well as the horn antenna support, absorbing pads have been used to cover them as shown in

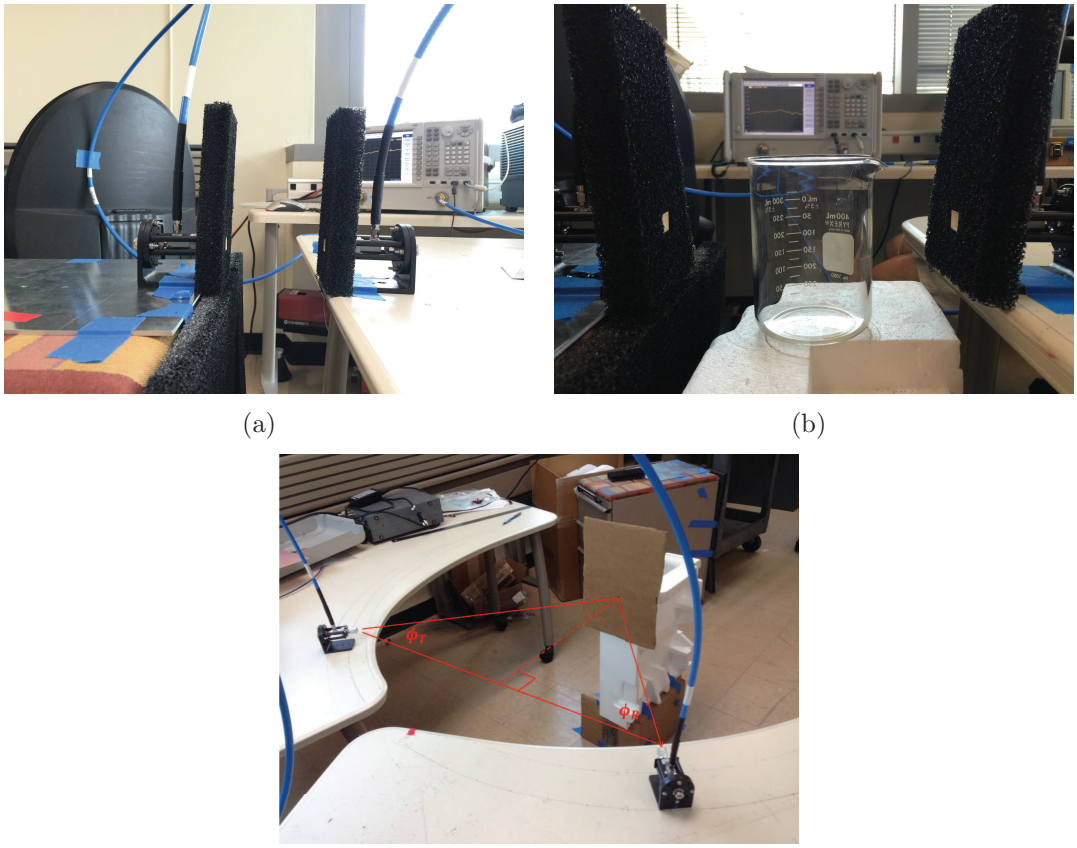

Figure 72: Photographs of measurement scenarios: (a) LoS; (b) OLoS, glass as obstruction; (c) Reflected NLoS, cardboard as reflector.

Fig. 72(a). The cylinder-obstructed LoS (OLoS) and RNLoS measurement setups are presented in Fig. 72(b) and 72(c), where effects of ground reflection have also been eliminated by elevating the antennas sufficiently and using the absorbers.

Considering the longer range of 30 GHz band indoor channels, the LoS T-R separation distance has been varied from 10 cm to 190 cm in 5 cm increments. For the OLoS scenario, three cylindrical obstructions of the same material as in the D-band OLoS measurements (i.e., glass, plastic, and ceramic) have been used, and T-R separations are varied in identical manner as in the LoS scenario. Each obstruction is placed such that the cylinder's center coincides with the midpoint of the separation distance. Further, a diffraction measurement has also been performed for 30 GHz OLoS channel with a similar measurement setup as the one presented in Section 5.6, where the cylinder obstruction is pulled away along the path orthogonal to the LoS. For this measurement, the T-R separation was set to 40 cm, and the cylinder has been orthogonally offset in 5 mm increments from 0 to 180 mm. In the RNLoS scenario, the same materials as in D-band RNLoS channels (i.e., Aluminum plate and cardboard) are considered to facilitate the comparative study. By varying the angular position of the R_x (i.e., $0^\circ \leq \phi_R \leq 90^\circ$ in Fig. 72(c)), while keeping the T_x position fixed (i.e., $\phi_T = 45^\circ$), the tolerable R_x angular offset range, where the coherence bandwidth stays sufficiently high, has been investigated. For RNLoS, the LoS separation distance was fixed to 92 cm. Finally, reflection coefficient magnitudes of the different materials at 30 GHz have also been measured and compared with those at 300 GHz using the similar setup described in Section 6.3.3. Here, the incident angle (i.e., $90^\circ - \phi_T$) and the reflected angle (i.e., $90^\circ - \phi_R$) are equally varied from 0° to 90°, while the total propagation distance is fixed at 130 cm, and the variation in the magnitude of the reflection coefficient is measured with respect to the angle for different materials.

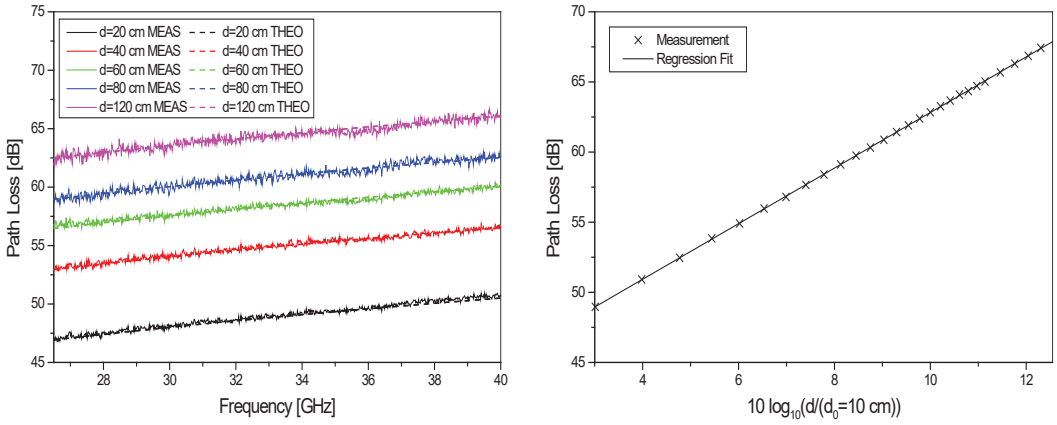

(a) (b)

Figure 73: 30 GHz LoS path loss measurements in (a) frequency and (b) distance domains.

8.3 Results and Analysis

8.3.1 LoS Comparison

Figures 73(a) and 73(b) present the measured 30 GHz LoS path loss plots in the frequency and distance domains, respectively. Figure 73(a) shows close matches between the measured and theoretical path losses for several different T-R separations. Also, it is observed from Fig. 73(b) that, due to effective elimination of reflections, including one from ground, an almost perfect linear regression fit has been achieved between the measured and modelled log-distance path losses for the 30 GHz LoS channel.

Table 15: 30 GHz/D-band/300 GHz Path Loss Parameters in LoS environment

	30 GHz	D-band	300 GHz
PLE, γ	1.9815	1.97	1.927
Std. Dev., σ	0.033 dB	0.12 dB	0.67 dB
PL_0 (d_0=10 cm)	43 dB	55.5 dB	62.8 dB

Table 15 compares the path loss parameters found in the three bands: 30 GHz band, D-band, and 300 GHz band. For all three bands, a path loss exponent that is

very close to 2 has been found, and the smallest standard deviation, σ, is obtained for the 30 GHz band due to the complete absence of ground reflection, as shown in Fig. 73(b). In addition, the significance of T-R misalignment is less pronounced for 30 GHz LoS channels than the other two bands because of the wider beamwidths of the antennas, which have contributed to the small standard deviation as well. Note that the reference distance has been set to 10 cm to accommodate the short-range indoor environment.

Table 16: 30 GHz/D-band/300 GHz Multipath Parameters in LoS environment

Distance [cm]	30 GHz		D-band		300 GHz	
	τ_{rms} [ps]	B_c [GHz]	τ_{rms} [ps]	B_c [GHz]	τ_{rms} [ps]	B_c [GHz]
5	88.12	1.806	-	-	105.56	1.508
10	99.82	1.594	-	-	145.77	1.092
15	106.14	1.499	-	-	223.96	0.711
20	111.94	1.422	-	-	275.39	0.578
25	115.92	1.373	-	-	325.23	0.489
30	135.11	1.178	-	-	401.29	0.397
35	142.80	1.115	12.00	13.263	426.28	0.373
40	155.88	1.021	11.89	13.386	506.99	0.314
45	167.48	0.950	11.66	13.650	561.30	0.284
50	182.76	0.871	10.09	15.774	566.14	0.281
55	188.26	0.845	12.84	12.395	626.54	0.254
60	190.06	0.837	8.96	17.763	-	-
65	205.89	0.773	13.44	11.842	-	-
70	220.80	0.721	9.41	16.913	-	-
75	235.12	0.677	10.03	15.868	-	-
80	237.43	0.670	15.97	9.966	-	-
85	262.48	0.606	10.72	14.847	-	-
90	263.06	0.605	-	-	-	-
95	284.74	0.559	-	-	-	-
100	294.55	0.540	-	-	-	-

A comparison of the LoS channel's multipath propagation at 30 GHz, D-band, and 300 GHz is presented in Table 16, where RMS delay spreads (Eq. (4.3.2)) and coherence bandwidths ($B_c = 1/(2\pi * \tau_{rms})$) of the LoS channels in the three bands are found from the measured multipath intensity profiles for different T-R separations. For the comparison to be feasible, a common noise threshold of -70 dB is applied to all three frequency bands. It is observed from the table that the least RMS delay

spreads, and therefore, the widest coherence bandwidths, are obtained for D-band LoS indoor channels, followed by the 30 GHz and 300 GHz bands. While a general trend of increasing delay spread as T-R separation increases is observed in 30 GHz and 300 GHz LoS channels, D-band's τ_{rms} fluctuates around the average value of 11.5 ps for the considered separation distances.

8.3.2 OLoS Comparison

Figure 75 shows the measured path losses in the frequency domain (Figs. 75(a),75(c), and 75(e)) and distance domain (Figs. 75(b),75(d), and 75(f)) for the 30 GHz channels obstructed by the three cylindrical obstructions: a glass, a plastic cup, and a ceramic mug. On Figs. 75(b),75(d), and 75(f) are also shown linear regression fits through the scattered path loss measurements at each T-R separation distance as well.

For the ease of comparison, the scatter plots and regression fits of the three cylinders are plotted on the same graph for 30 GHz band and D-band, which are shown in Figs. 74(a) and 74(b), respectively, and the parameters obtained from each regression fit are summarized in Table 17. Please note that, for the distance-domain path loss parameters (i.e., γ, σ, PL_0), the frequency-averaging windows of 13.5 GHz (26.5 GHz–40 GHz) for 30 GHz band and 60 GHz (110 GHz–170 GHz) for D-band have been selected, except for the case of ceramic-obstructed D-band channel, in which the path loss variation with respect to frequency is significant, i.e., more than 25 dB (Please refer to Fig. 31(e)). Therefore, for this particular D-band scenario, an averaging window of 10 GHz from 110 GHz to 120 GHz, within which the measured path loss is considered constant, is used.

From Fig. 74, it is evident that the highest attenuation is caused by ceramic, followed by glass and plastic, in both 30 GHz and D-band. From Table 17, a similar trend of increasing γ and σ, in the order of plastic, glass, and ceramic, is observed in the two bands, in accordance with the order of increasing path loss. For D-band

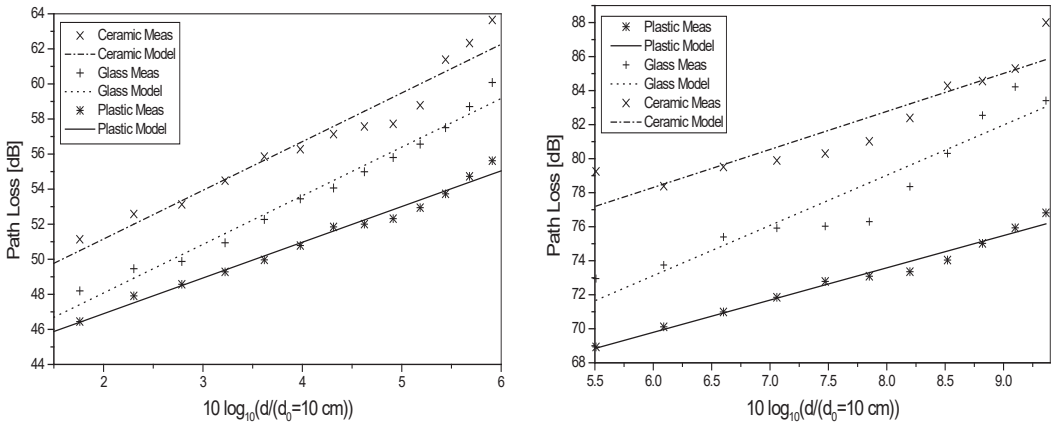

(a) (b)

Figure 74: Measured scatter path losses and regression fits for plastic, glass, and ceramic on a single plot in (a) 30 GHz band and (b) D-band.

Table 17: 30 GHz/D-band Path Loss Parameters in OLoS environment with Cylinders of Different Materials

	Glass		Plastic		Ceramic	
	30 GHz	D-band	30 GHz	D-band	30 GHz	D-band
γ	2.7733	2.9519	2.0377	1.8964	2.7767	2.2351
σ	0.5658 dB	1.3418 dB	0.3739 dB	0.3757 dB	0.9425 dB	1.2502 dB
PL_0 (d_0=10 cm)	42.53 dB	55.41 dB	42.82 dB	58.41 dB	45.60 dB	64.90 dB

ceramic, however, a γ that is lower than that of glass is obtained, although the signal obstruction by ceramic is greater than that by glass, as observed in Fig. 74(b). This can be explained by the existence of surface-diffraction in the ceramic-obstructed D-band channel, as it has been proven in Section 5.6. It is also observed from the table that the shadowing variance is greater in the D-band compared to the 30 GHz band for all three materials. The observations from Fig. 74 and Table 17 lead to the conclusion that the relative transparency of the three materials are equal in 30 GHz and D-band OLoS channels (i.e., path loss increases in the order of plastic, glass, and ceramic in both bands), and they exhibit similar large-scale characteristics in terms of γ, while generally higher σ has been obtained in D-band.

By comparing the differences between the measured path losses and the theoretical free-space path losses at given distances for each material (Figs. 75(a), 75(c), and 75(e)), it is observed that plastic has almost no penetration loss and minimal frequency-dependence in its path loss at 30 GHz. Evidently, the penetration loss and frequency-dependence increase for glass and ceramic as for the D-band OLoS scenarios, but comparison between Figs. 75 and 31 indicates that all three materials are much more penetrable in 30 GHz band than they are in D-band, which is especially true in the case of ceramic. For the purpose of complete comparative analysis of OLoS propagation in the two bands, it is also necessary to investigate the presence of diffraction at the curvature of cylinder surface by applying the Uniform Theory of Diffraction (UTD) once again to the 30 GHz OLoS channel, as it has been done in D-band in Section 5.6.

Figure 77 presents the measured and UTD modelled diffraction loss curves with respect to the orthogonal offset distance of the cylindrical obstruction for 30 GHz, D-band, and 300 GHz channels. For UTD modelling, the obstructing cylinder was a ceramic mug for the 30 GHz and D-band channels, while, for 300 GHz, due to limited beamwidth and propagation distance, the mug's diameter of 8.5 cm was too large for the diffraction to occur. Therefore, a much thinner metal pipe with 1.6 cm of diameter has been used for 300 GHz OLoS channel's diffraction measurement, whose setup is shown in Fig. 76. The same procedure as in Section 5.6 was followed to obtain the measured diffraction loss at the 30 GHz and 300 GHz bands, and their mathematical UTD models have been found by applying the same theoretical details presented in Appendix A. One of the main observations from the comparison presented in Fig. 77 is that the measurement and UTD curves match with great precision for D-band and 300 GHz, whereas the degree of matching drops slightly for the 30 GHz channel, especially in the Shadow Region. This is due to the fact that the contribution from the ray component that penetrates the cylinder is higher for the lower 30 GHz band

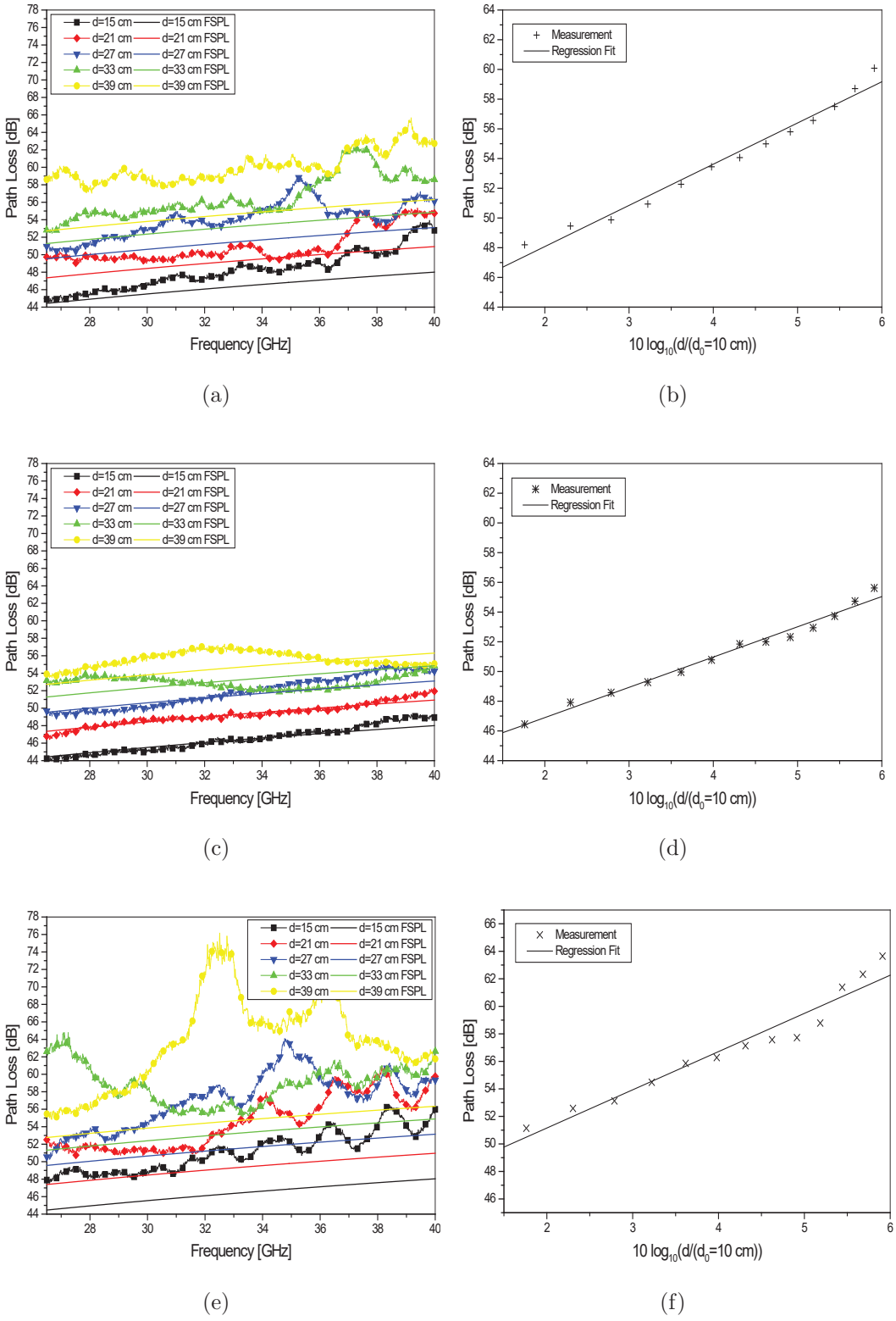

Figure 75: Measured path losses in the frequency and distance domains for 30 GHz OLoS channels obstructed by: (a),(b) a glass, (c),(d) a plastic cup, and (e),(f) a ceramic mug.

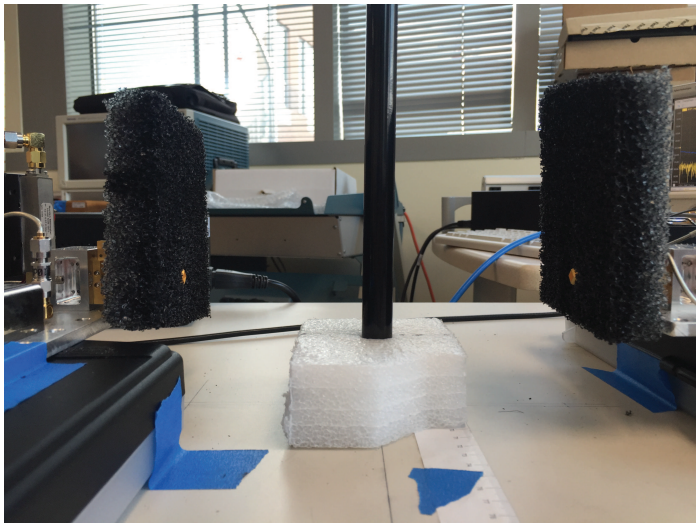

Figure 76: Diffraction measurement setup for the 300 GHz OLoS channel with a thin metal pipe as the cylindrical obstruction.

when compared to the other two bands. Therefore, it is observed from Fig. 77(a) that the measured diffraction gain is higher than that modelled with UTD, which does not take into account the fields that propagate through the cylinder obstruction. Another observation is the "dip" that appears near the shadow boundary in the measured diffraction gain curves in Figs. 77(a) and 77(b). The "dip", or the abrupt increase in diffraction loss, results from the thickness of the mug's wall. In other words, when the offset distance approaches the value, at which LoS is tangent with the cylinder, the waves have to propagate the longest distance through the ceramic material, and therefore, undergo the largest attenuation. On the other hand, in the UTD model, the thickness of the cylinder wall is not considered, which explains why the "dip" is absent in the UTD diffraction gain curves. For the 300 GHz OLoS channel (Fig. 77(c)), however, the "dip" is not observed in the measurement, and that is because the thickness of the pipe was less than the increment of the mug offset (i.e., 1 mm), such that the measurement instance did not capture the moment when the "dip" occurred.

Finally, Table 18 compares the measured RMS delay spreads and the coherence

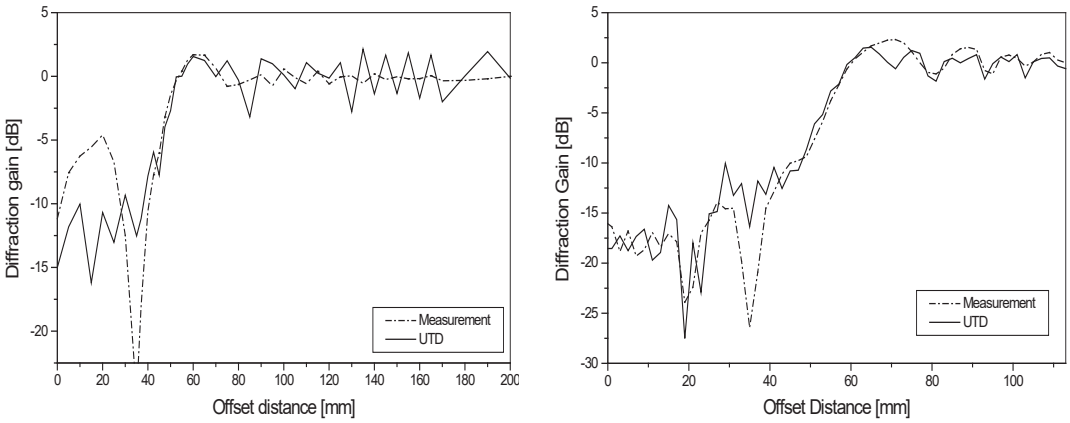

(a)

(b)

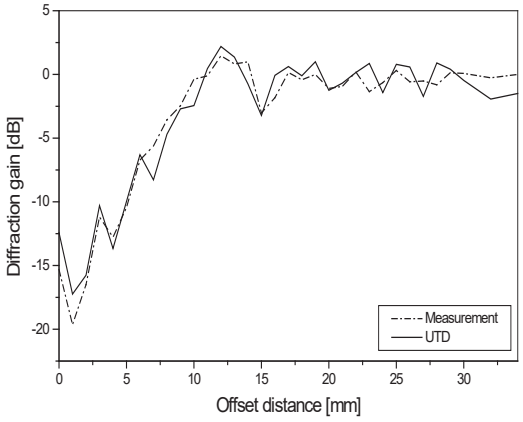

(c)

Figure 77: Measured and UTD modeled diffraction gain curves at the center frequencies of the three bands: (a) $f_c = 33.25$ GHz, (b) $f_c = 140$ GHz, and (c) $f_c = 307$ GHz.

bandwidths of 30 GHz band and D-band for several different T-R separation distances when the channels are obstructed by the three cylinders: a glass, a plastic cup, and a ceramic mug. Note that the 300 GHz band has been excluded from the comparison in this particular OLoS scenario since the signal attenuation by the cylindrical obstruction is too large for a viable connection. From Table 18, it is evident that the RMS delay spreads for the 30 GHz band are larger than those for D-band. Also, for D-band, ceramic mug has clearly the highest RMS delay spread, and therefore, the lowest coherence bandwidth, followed by the glass and plastic cup, whereas, for the 30 GHz band, the ceramic mug, although not by as much difference as in D-band, still shows a generally higher RMS delay spread than the other two materials that have comparable RMS delay spreads and coherence bandwidths. When compared with the LoS scenario with equal separation, as shown in the table, the increase in the RMS delay spreads of the OLoS scenario is much greater in D-band, especially for glass and ceramic, which indicates that the cylinders appear more disruptive to D-band signals than they do to the 30 GHz band. Nevertheless, it is observed from the table that coherence bandwidths are still much higher in D-band compared to the 30 GHz band.

Table 18: 30 GHz/D-band Multipath Parameters in OLoS environment with Cylindrical Obstructions

d [cm]	Glass				Plastic				Ceramic				LoS	
	30 GHz		D-band		30 GHz		D-band		30 GHz		D-band		30 GHz	D-band
	τ_{rms} [ps]	B_c [GHz]	τ_{rms} [ps]	B_c [GHz]	τ_{rms} [ps]	B_c [GHz]	τ_{rms} [ps]	B_c [GHz]	τ_{rms} [ps]	B_c [GHz]	τ_{rms} [ps]	B_c [GHz]	τ_{rms} [ps]	τ_{rms} [ps]
35	335	0.475	31.86	4.99	199	0.801	14.40	11.05	197	0.809	76.60	2.078	143	12.0
40	197	0.806	44.13	3.61	170	0.935	15.50	10.27	286	0.556	76.11	2.091	156	11.9
55	213	0.746	45.55	3.49	221	0.720	23.74	6.70	360	0.442	62.87	2.532	188	12.8
60	238	0.670	31.65	5.03	239	0.665	21.46	7.42	429	0.371	61.77	2.576	190	8.96
75	333	0.478	57.17	2.78	269	0.591	10.85	14.68	407	0.391	54.86	2.901	235	10.0

8.3.3 RNLoS Comparison

Figure 78 presents the measured path loss curves for the RNLoS scenario shown in Fig. 72(c) when the receiver angle, ϕ_R is varied between 0° and 90°, while ϕ_T is

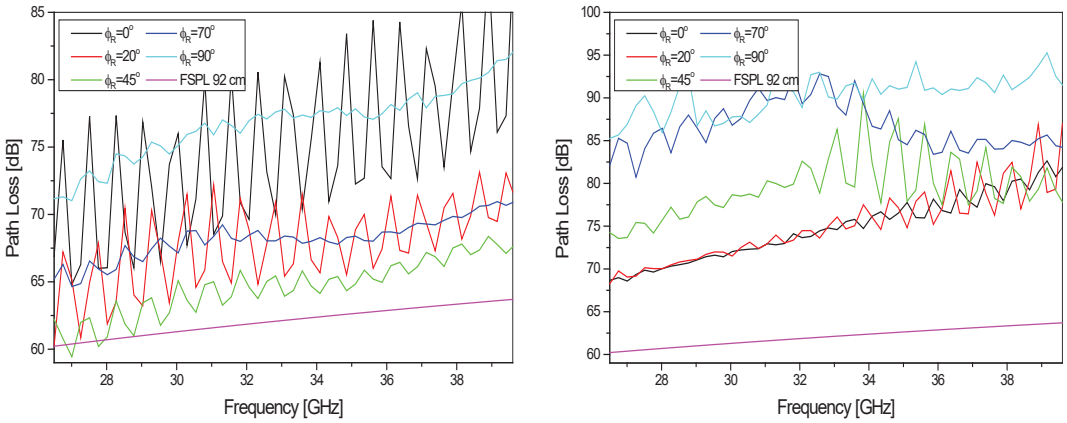

(a) (b)

Figure 78: Measured path losses in frequency domain in 30 GHz RNLoS channels with two different reflecting surfaces: (a) Aluminum plate and (b) Cardboard, when receiver angle is varied between 0° and 90°, and transmitter angle is fixed at 45°.

fixed at 45°, for the same reflecting surfaces used in D-band RNLoS measurement (Section 5.5), i.e., Aluminum and cardboard. The figure also compares the measured curves with the theoretical Free-Space path loss calculated for the LoS distance of 92 cm. The first observation from the figure is that, for the Aluminum plate, as in D-band, the lowest path loss, or the maximum received power occurs under the condition, $\phi_T = \phi_R = 45°$, and the path loss increases as the angle deviates from 45°. On the other hand, for cardboard, the maximum transfer of transmitted power does not occur at $\phi_T = \phi_R = 45°$, but when $\phi_R = 0°$. The reason for this will become apparent later in this subsection. The second observation is the ripples in the measured path losses; The ripples result from the interference between the LoS path and the reflected path, and their peak-to-peak variation increases as the amplitude of the two paths become comparable. The effect of this interference is much more pronounced for the 30 GHz channel than the D-band or 300 GHz channels because of the wider beamwidths of the antennas. In Fig. 78(a), it is observed that the ripples are deepest for $\phi_R = 0°$ because the LoS path is strongest at this angle when the

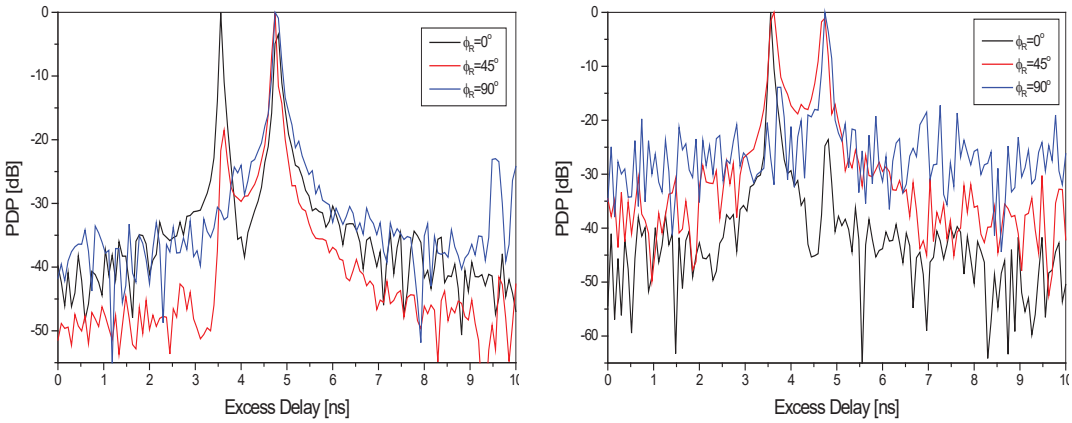

(a) (b)

Figure 79: Measured power delay profiles in 30 GHz RNLoS channels with two different reflecting surfaces: (a) Aluminum plate and (b) Cardboard, when receiver angle is varied between 0° and 90°, and transmitter angle is fixed at 45°.

R_x antenna is pointed towards the T_x antenna. As ϕ_R increases, the LoS path gets weaker, and the ripples also fade away as observed in Fig. 78(a). How the amplitude of the LoS path changes with respect to the reflected path as the receiver angle increases can be observed from the PDPs, which are presented in Fig. 79(a) for the Aluminum plate. It is apparent from Fig. 79(a) that, at $\phi_R = 0°$, the LoS path is actually stronger than the reflected path by about 3.5 dB. The PDPs for the cardboard are shown in Figure 79(b), from which it is observed that, at $\phi_R = 0°$, the LoS path is much stronger than the reflected path due to the low reflectivity of the cardboard. Therefore, for the cardboard, the path loss is lowest when the LoS path is dominant in the channel (i.e., $\phi_R = 0°$) as shown in Fig. 78(b). Figure 79(b) also shows that the strengths of LoS and reflected paths become almost equal at $\phi_R = 45°$, beyond which the reflected path now becomes the dominant component in the channel.

Table 19 compares the multipath parameters measured in the three frequency bands of interest for this particular RNLoS channel, where receiver angle changes while transmitter is fixed, with Aluminum and cardboard as reflecting surfaces. Note

Table 19: 30 GHz/D-band/300 GHz Multipath Parameters in RNLoS environment with Different Reflecting Materials

ϕ_R	30 GHz					D-band					300 GHz				
	Cu. plate		Cardboard		LoS	Al. plate		Cardboard		LoS	Al. plate		Cardboard		LoS
	τ_{rms} [ps]	B_c [GHz]	τ_{rms} [ps]	B_c [GHz]	τ_{rms} [ps]	τ_{rms} [ps]	B_c [GHz]	τ_{rms} [ps]	B_c [GHz]	τ_{rms} [ps]	τ_{rms} [ps]	B_c [GHz]	τ_{rms} [ps]	B_c [GHz]	τ_{rms} [ps]
0°	861	0.185	1037	0.154		312.9	0.509	-	-		3634	0.044	-	-	
10°	688	0.231	952	0.167		311.2	0.511	-	-		3601	0.044	-	-	
35°	378	0.421	1256	0.127		9.36	17.00	36.84	4.32	10.03	1054	0.151	2664	0.060	
37.5°	-	-	-	-		-	-	-	-		1020	0.156	2432	0.065	553
45°	350	0.454	1609	0.099	263	-	-	-	-		1728	0.092	2894	0.055	
60°	402	0.396	2326	0.068		26.97	5.901	-	-		3548	0.045	3731	0.043	
65°	434	0.367	2913	0.055		-	-	-	-		3487	0.046	3381	0.047	
70°	486	0.327	3282	0.049		-	-	-	-		3734	0.043	-	-	
90°	1324	0.120	4429	0.036		678.5	0.235	-	-		-	-	-	-	

that the angle of specular reflection, or the angle that the T_x is fixed at, is 45°, 35°, and 37.5° for the 30 GHz, D-band, and 300 GHz channels, respectively. All three bands show a similar pattern, where the least RMS delay spread, i.e., the widest coherence bandwidth, is achieved at the angle of specular reflection (i.e., $\phi_T = \phi_R$), while it decreases as the receiver angle deviates from the transmitter angle. However, for 30 GHz RNLoS channel with cardboard as the reflector, a wider coherence bandwidth is achieved for a smaller receiver angle due to the existence of the dominant LoS path. This also indicates the fact that when the reflecting surface has low reflection coefficient, the LoS path, despite the angular offset as big as 45° between T_x and R_x, can be a more reliable link than the perfectly aligned (i.e., $\phi_T = \phi_R$) reflected path. Furthermore, Table 19 shows that, under specular reflection, the RNLoS channel with the metal plate as the reflector has about 4 times wider coherence bandwidth than that with the cardboard for the 30 GHz band and D-band, while, for the 300 GHz band, the maximum coherence bandwidth with the Aluminum plate is only about twice as wide as that with the cardboard. It can also be found from the table that the tolerable receiver angle deviation from the transmitter angle that results in a coherence bandwidth reduction of no more than 50 % is around ±25°, ±10°, and ±7.5° for 30 GHz, D-band, and 300 GHz RNLoS channels, respectively. Finally,

Table 19 also compares the RNLoS RMS delay spreads with those of LoS link with an equal T-R separation for each band. The comparison indicates that, although the delay spread is slightly higher, the RNLoS link is almost as reliable as the LoS for all three bands, especially when the reflecting surface is metallic and the receiver angle equals the transmitter angle.

For the RNLoS channel, it is also important to characterize the reflectors in terms of their reflection coefficient, especially for 30 GHz channels that could have a much stronger LoS path than the reflected path when the reflectivity of the material is low, as has been shown in the case of cardboard. Therefore, the reflection coefficient magnitude of different materials has been measured using Eqs. (36) and (37) in 30 GHz band, and is plotted with respect to the incident angle in Fig. 80(a) for three materials: Copper plate, cardboard, and wood. In Fig. 80(b), reflection coefficients of the same materials are also measured in the 300 GHz band to compare the reflective characteristics of the materials in the two bands. Note that for the calculation of reflection loss in Eq. 37, the measured frequency response is averaged across the full bandwidths of the 30 GHz and 300 GHz bands.

From Fig. 80(a) and 80(b), it is observed that the metal is a slightly better reflector in the 30 GHz band, whereas the non-conducting materials, such as cardboard and wood, have slightly higher reflection coefficient magnitudes in the 300 GHz band. Note that the LoS path also affects the reflection coefficient measurement since its interference with the reflected path causes the measured frequency response to ripple, and when averaged across the entire measured bandwidth, it can lead to false reflection losses. This is why, in Fig. 80(a), the $|\Gamma|$ starts to increase for cardboard and wood, and fluctuation in the reflection coefficient starts to appear for metal beyond 55°, at which the LoS path's amplitude becomes comparable with that of the reflected path and the ripples in the measured S_{21} becomes significant. For the 300 GHz channel, on the other hand, not only the antenna's mainlobe is very narrow,

but the sidelobes are also negligibly small compared to the mainlobe, and therefore, the interference from the LoS path is absent. Hence, in Fig. 80(b), the $|\Gamma|$ values are valid for a wider range of incident angles (i.e., upto 85°) than the 30 GHz channel. Another observation from the 300 GHz reflection coefficients (Fig. 80(b)) is that, for the Aluminum plate, $|\Gamma|$ starts high near 1 and decreases to about 0.7 at 85°, while, for wood, it behaves in completely opposite fashion, i.e., starts low around 0.2 and increases to 0.6 towards a higher incident angle. Also, the reflection coefficient of cardboard is fairly constant at around 0.16 for all incident angles (i.e., from 15° to 50°) in the 30 GHz band, whereas, in the 300 GHz band, it is as low as 0.24 at 20° and increases with the incident angle.

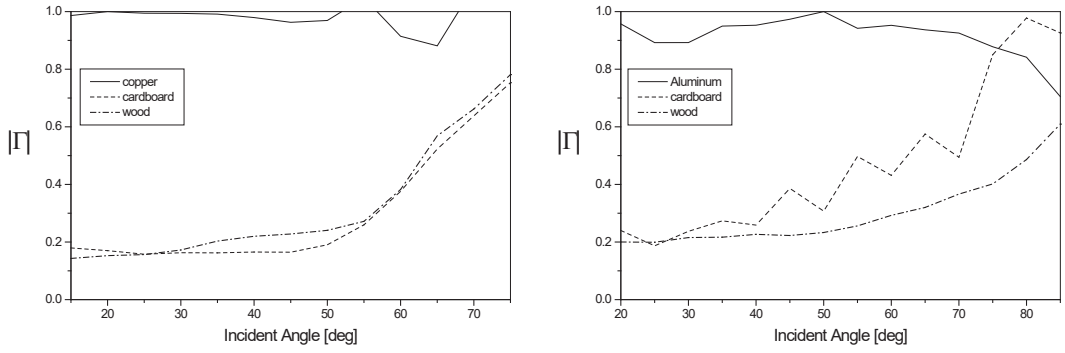

(a) (b)

Figure 80: Magnitude of reflection coefficient for Aluminum plate, Cardboard, and Wood in (a) 30 GHz and (b) 300 GHz bands.

8.4 Summary

This chapter has presented the empirical comparative analysis among the three frequency bands that have potential usage for future indoor THz device-to-device wireless channels due to wide bandwidths available, namely, the 30 GHz band (26.5 GHz–40 GHz), the D-band (110 GHz–170 GHz), and the 300 GHz band (300 GHz–320 GHz). The comparison has been made in large-scale (i.e., path loss characterization in frequency and distance domains) and small-scale (i.e., multipath characterization with power delay profiles) in three different indoor scenarios: LoS, Obstructed-LoS (OLoS), and Reflected-Non-LoS (RNLoS). In the LoS environment, it has been found that all three bands exhibit path loss exponents that are very close to 2, while the standard deviation of shadow fading increases as the band moves up the frequency spectrum because of the difficulty in T-R alignment due to narrower beamwidth. Small-scale comparative analysis reveals that D-band has the smallest RMS delay spread (i.e, widest coherence bandwidth) in the LoS channel, followed by the 30 GHz and 300 GHz bands. In the OLoS environment, three cylinders of different materials, glass, plastic, and ceramic, have been used as the obstruction for the three bands. Large-scale comparative analysis of 30 GHz and D-band OLoS channels has revealed that, while standard deviation of shadow fading is greater in D-band, the two bands exhibit similar path loss exponents for each material, except for the ceramic, in which case the presence of surface-diffracted rays has resulted in lower path loss exponent in D-band. The application of UTD has also revealed that, unlike D-band, the diffracted ray is not a dominant ray component in the 30 GHz ceramic-obstructed channel. While the 300 GHz band suffers from significantly high path losses with the cylinders, UTD has also shown that, when the diameter of the cylindrical obstruction is properly scaled down to accommodate the narrow beamwidth, diffraction at the cylinder's convex surface can occur in the 300 GHz band as well. Furthermore, while coherence bandwidths for the three materials are comparable (few hundreds of MHz)

in the 30 GHz band, GHz-range coherence bandwidths that are highest for plastic, followed by glass and ceramic, are measured in the D-band. Finally, in an RNLoS environment, the wider beamwidth and higher sidelobes of 30 GHz antennas result in the existence of an LoS path even at the perfect angular alignment (i.e., $\phi_T = \phi_R$), and for a reflective surface, such as a metal plate, the LoS path's interference with the reflected path leads to the fluctuation in path loss in frequency domain. Coherence bandwidths are widest when the receiver angle equals the transmitter angle for all three bands for the metal reflecting surface, although, for the 30 GHz RNLoS channel, when the reflectivity of the surface is poor, the LoS path with T-R angular misalignment as large as 45° can have a wider coherence bandwidth than the perfectly aligned reflected path. Under the condition $\phi_T = \phi_R$, reflection off the metallic surface has resulted in about 4 times wider coherence bandwidth than cardboard in the 30 GHz band and D-band, while it was twice as wide as cardboard in the 300 GHz band. For a good reflector (i.e, Copper or Aluminum), the tolerable receiver angle deviation from the transmitter angle that resulted in a coherence bandwidth reduction of no more than 50 % has been found to be around ±25°, ±10°, and ±7.5° for 30 GHz, D-band, and 300 GHz RNLoS channels, respectively. Lastly, the measured magnitudes of reflection coefficients for the three materials, Aluminum, Cardboard, and Wood, show generally more consistent coefficients with respect to the incident angle in the 30 GHz band compared to the 300 GHz band for all three materials. For metal, the coefficient magnitude is higher at 30 GHz, whereas, for the non-conductors, it is slightly lower at 30 GHz than 300 GHz.

CHAPTER IX

RESEARCH CONTRIBUTIONS AND FUTURE RESEARCH DIRECTIONS

9.1 Research Contributions

The contributions of this research are summarized as follows:

1. A double-sided Linearly-Tapered Slot Antenna (LTSA) that operates at the 300 GHz band has been designed simulated, and fabricated on a low-K material, RT Duroid 5880. The fabricated antenna has been used in the 300 GHz transmission system in replacement of the horn antennas, and a simple post-processing of the measured transfer function has been used to obtain the gain and return loss of the fabricated LTSA. Average gain of 13 dBi and S_{11} below -10 dB across the measured bandwidth between 305 GHz and 320 GHz are achieved, which has shown the possibility of a classical broadband antenna's operation at THz frequencies, while maintaining its high-gain and wideband characteristics. [66]

2. $300 - 320$ GHz LoS and NLoS desktop channel measurements are used for the large-scale (i.e, path loss, shadowing) and small-scale (i.e., RMS delay spread and coherence bandwidth) characterization the THz channel. For LoS, a path loss exponent around 1.9 and a standard deviation of 0.67 dB contributed by the difficulty in T-R alignment are found. For NLoS, it is found that metal causes the highest path loss, followed by FR4 and plastic. From small-scale characterization, the mean excess delay and rms delay spread increase with distance and the rms delay spread in a desktop THz channel is found to be much smaller

than in typical indoor ultra-wideband channels. In addition, the LoS power delay profiles show strong reflections from the transmitter electronics that can significantly reduce the channel coherence bandwidth. Finally, the statistical analysis of the measured signal amplitude in LoS and NLoS environments is performed. For both LoS and NLoS propagation environments, it is found that a lognormal distribution provides the best fit. [67], [68]

3. The channel measurement and characterization in large- and small-scale have also been performed at D-band in more diverse indoor scenarios, including LoS, Cylinder-Obstructed LoS (OLoS), and Reflected-NLOS (RNLoS) environments. D-band LoS channel also has a path loss exponent close to 2 and a very small standard deviation of 0.12 dB. Wide coherence bandwidths in the GHz range are found for LoS links with T-R separation less than 1 m. For NLoS measurements (i.e, OLoS and RNLoS), path loss measurements have revealed the penetration and reflection losses of objects of different shapes (i.e., cylinders and large panels) and materials (i.e, glass, plastic, ceramic, cardboard, metal, etc.). Especially, in a cylinder-obstructed LoS scenario, it has been found that the received power is not only contributed by the EM waves that penetrate the cylinder, but also by the creeping waves that travel around the cylinder through diffraction at its convex surface for ceramic material. The existence of surface-diffracted rays has been confirmed by modelling the diffraction loss caused by the cylindrical obstruction with the Uniform Theory of Diffraction (UTD). Path loss exponents greater than 2 are found in OLoS environments, and the exponent increases in the order of plastic, glass, and ceramic. Coherence bandwidth for plastic is comparable with that of LoS, while it drops to few GHz for glass and ceramic. In an RNLoS environment, the reflective characteristics of Aluminum and cardboard are compared through measured path losses of the reflected signals, whose RMS delay spread is found to increase rapidly as

the reflection angle deviates from the incident angle with an Aluminum plate as the reflecting surface. [69], [70], [71]

4. 300 GHz Chip-to-Chip channels in a unique propagation environment of a computer motherboard that has high density of scatterers and diversity of materials, including FR4, copper, lead, silicon, etc. It is found that the antenna height above the board surface and the roughness and material composition of the board section where ground reflection occurs can affect the LoS path loss by as much as 3 dB. On a motherboard, signals can also propagate between two vertically inserted components, such as RAMs and graphic cards, and the constructed or destructive interference between the direct LoS and the path bouncing between the two surfaces can decrease or increase the path loss. Further, signals can reflect off the front and back surfaces of the vertical components when an LoS path is unavailable, and it has been found that the back surface of the RAM module is an excellent reflector with a reflection coefficient close to 1, while that of the front surface varies significantly depending on the incident angle due to components of diverse shapes and materials. It follows that the signals reflecting off the back surface of the RAM has 3 times wider coherence bandwidth than the front surface when incident and reflection angles are equal. For the front surface, a reflection angle that is off by 2° from the incident angle can result in a 99 % reduction in coherence bandwidth, while the back surface has higher tolerance to reflection angle deviation (6°–7°). All these results have confirmed the possibility of reliable THz links for chip-to-chip wireless communications on a computer motherboard with coherence bandwidths as wide as tens of GHz, while careful positioning of antennas with respect to motherboard layout is necessary for an optimal channel environment. [72], [73]

5. A 2-D geometry-based statistical channel model has been devised for indoor

short-range THz channels. The data collected from the measurement campaigns conducted in D-band and the 300 GHz band are used to validate the model. The analytically derived frequency auto-correlation function of the channel is inverse Fourier transformed to obtain the power delay profile, which are then compared with the measured ones in LoS and NLoS scenarios from the two THz bands. Approximated frequency correlation functions that bypass the numerical evaluation of integrals that do not have closed-form solutions along with the conditions required for the approximation to be valid are also provided. Furthermore, to overcome the impracticality of the mathematical reference model that assumes an infinite number of scatterers, a simulation model based on the Sum-of-Sinusoids (SoS) method is used, such that statistical properties of the reference model can be realized with a finite number of scatterers. The three PDPs, i.e., analytical, measured, and simulated, are compared with one another for a number of measurement scenarios from the THz bands, and good match among them is achieved for all the scenarios, validating the proposed reference model as well as the simulation model. [74], [75]

6. The indoor measurement campaigns conducted in D-band and the 300 GHz band have been replicated at a lower spectrum centered at 33.25 GHz, which is a potential sub-THz band for the next generation mobile network. The first obvious advantage of 30 GHz band is the longer distance the signal can propagate due to lower free-space path loss. Further, the beamwidth of the 30 GHz horn antenna that is much wider than those of the other two bands allows for minimal standard deviation in an LoS scenario since path loss variation from T-R misalignment is minimized. In an OLoS environment, for cylinders of the three materials, glass, plastic, and ceramic, the shadowing standard deviation is smaller in the 30 GHz band, while its path loss exponents are comparable to those in D-band with the exception of ceramic, for which a lower γ is obtained in

D-band due to the presence of surface-diffracted rays. While the ceramic mug's dimensions were too large for 300 GHz waves to diffract at the cylinder's convex surface, application of the UTD to a 30 GHz OLoS channel has revealed that the rays penetrating the cylinder, rather than those diffracting at its surface, are dominant at 30 GHz. Furthermore, small-scale characterization has shown much higher RMS delay spreads for all three cylinders at 30 GHz compared to D-band. Finally, in an RNLoS environment, the wider beamwidth and higher sidelobes of 30 GHz antennas result in the existence of an LoS path even at the perfect angular alignment (i.e., $\phi_T = \phi_R$), and for a reflective surface, such as a metal plate, the LoS path's interference with the reflected path leads to the fluctuation in path loss in the frequency domain. As observed in the two THz bands, the RMS delay spread is highest when the receiver angle equals the transmitter angle for the 30 GHz band as well for the metal reflecting surface. However, for the 30 GHz RNLoS channel, when the reflectivity of the surface is poor, an LoS path with T-R angular misalignment as large as 45° can have a wider coherence bandwidth than the perfectly aligned reflected path. When reflection angle equals incident angle, a metal surface has resulted in about 4 times wider coherence bandwidth than cardboard in the 30 GHz band and D-band, while the delay spread doubled for the metal plate compared to cardboard in the 300 GHz band. For a good reflector (i.e, Copper or Aluminum), the tolerable reflection (R_x) angle deviation from the incident (R_x) angle that results in half the maximum coherence bandwidth has been found to be around ±25°, ±10°, and ±7.5° for 30 GHz, D-band, and 300 GHz RNLoS channels, respectively. The measured magnitudes of reflection coefficients for the three materials, Aluminum, Cardboard, and Wood, show generally more consistent coefficients with respect to the incident angle in the 30 GHz band compared to the 300 GHz band for all three materials. For metal, the coefficient magnitude

is higher at 30 GHz, whereas, for the non-conductors, it is slightly lower at 30 GHz than at 300 GHz.

9.2 Future Research Directions

In this thesis, properties of THz band channels have been explored in terms of statistical parameters, such as path loss exponent, standard deviation of shadowing, RMS delay spread, and coherence bandwidth. While these parameters offer useful information about the THz channels from a physical point of view, to enable THz communications, this research should be followed by channel characterization from a communications perspective with the actual transmission of binary data through the channel in LoS and NLoS environments, presenting more tangible information, such as realizable peak data rate, associated modulation schemes, and BER. Furthermore, in this thesis, the existence of two surface-diffracted rays in a D-band NLoS channel obstructed by a ceramic cylinder has been revealed through ray optics. However, in an indoor environment, one of the objects most frequently obstructing the signal is the human body, while its interaction with THz waves has not been researched in this thesis. It has been reported in [120] that human bodies can be modelled as cylinders filled with salt water for 60 GHz indoor channels. Therefore, to use the findings from the D-band cylinder-obstructed-LoS scenario, the feasibility of modelling of human body as a cylinder at THz band should first be investigated. Then, a new indoor THz propagation model that can precisely predict the channel fading due to signal obstruction by human bodies can be devised by incorporating their diffraction effect with THz waves. It has been also shown in the thesis that the physical dimensions of an LTSA, a classical broadband antenna, can be scaled down to few mm's and still maintain its high-gain and wideband properties at THz frequencies. However, due to limitations in the capabilities of the PCB milling machine, the overall size of the fabricated LTSA is still far too large for chip integration. Therefore, a future

research endeavor should be directed towards fabrication of the LTSA in micro- or nano-scale as well as its integration with an actual processor or a memory module. The chip-integrated LTSA will also enable much more realistic on-board chip-to-chip measurements in a functioning computer system that would assure the reliability of THz communications channels on a computer motherboard.

APPENDIX A

UTD FORMULATION OF SURFACE-DIFFRACTED AND REFLECTED FIELD COMPONENTS

In the Shadow Region, there are two surface-diffracted rays, travelling clock-wise and counter-clock-wise around the cylinder [113] as shown in Fig. 37(a). Hence, the total E-field at the observation point, S_0, is determined by the sum of these two rays. The E-fields associated with each ray at S_0 can be mathematically expressed as

$$E_1^d(S_0) = E^i(Q_1') \cdot T_1 \cdot \frac{e^{-jks_1^d}}{\sqrt{s_1^d}} \tag{66}$$

$$E_2^d(S_0) = E^i(Q_2') \cdot T_2 \cdot \frac{e^{-jks_2^d}}{\sqrt{s_2^d}} \tag{67}$$

where T is the UTD diffraction coefficient; $E^i(Q_1)$ and $E^i(Q_2)$ are the E-fields incident at Q_1 and Q_2, respectively, which are expressed as

$$E^i(Q_1') = \frac{e^{-jks_1'}}{\sqrt{s_1'}} \tag{68}$$

$$E^i(Q_2') = \frac{e^{-jks_2'}}{\sqrt{s_2'}} \tag{69}$$

In the Lit Region, on the other hand, the total field at the observation point, S_n, is determined by the contributions from the direct LoS ray and the reflected ray as shown in Fig. 37(b), and the fields associated with each ray can be written as

$$E^i(S_n) = \frac{e^{-jks^{LOS}}}{\sqrt{s^{LOS}}} \tag{70}$$

$$E^r(S_n) = E^i(Q_r) \cdot R \cdot \sqrt{\frac{\rho^r}{\rho^r + s^r}} \cdot e^{-jks^r} \tag{71}$$

where R is the UTD reflection coefficient, and $E_i(Q_r)$, the incident field at the reflection point, Q_r, is expressed as

$$E^i(Q_r) = \frac{e^{-jks^i}}{\sqrt{s^i}} \tag{72}$$

Calculations of T and R are omitted here, but can be found in [113]. In Eq. (71), ρ_r represents the caustic distance of the reflected ray tube, which can be calculated as following [113]

$$\frac{1}{\rho^r} = \frac{1}{\rho^i(Q_r)} + \frac{2}{a_0(Q_r)\cos\theta^i} \tag{73}$$

where $\rho_i(Q_r)$ is equivalent to s_i, and $a_0(Q_r)$ denotes the radius of curvature at the reflection point, Q_r. All parameters in Eqs. (66)–(73) are shown in Figs. 37(a) and 37(b). It is also observed from Fig. 37(b) that there exists a third ray reaching the observation point, which is equivalent to surface-diffracted ray 2 from Fig. 37(a). The total E fields in the Shadow and Lit Regions can finally be expressed as a sum of the field components defined in Eqs. (66), (67), (70), and (71):

$$E^{tot} = \begin{cases} E_1^d + E_2^d & ShadowRegion \\ E^i + E^r + E_2^d & LitRegion \end{cases} \tag{74}$$

APPENDIX B

DERIVATIONS OF THE SINGLE-REFLECTED AND DOUBLE-REFLECTED PATH LENGTHS

In this section, we show the derivations for the expressions in (43) and (44). We start with the derivations for (43). From the triangle, $A_T - S^{(l,m)} - A_R$, in Fig. 62, we can observe that

$$\epsilon_T^{(l,m)} \cos\alpha_T^{(l,m)} + \epsilon_R^{(l,m)} \cos(\pi - \alpha_R^{(l,m)}) \;=\; D, \tag{75}$$

Hence, the distance $\epsilon_R^{(l,m)}$ can be written as

$$\epsilon_R^{(l,m)} \;=\; \frac{\epsilon_T^{(l,m)} \cos\alpha_T^{(l,m)} - D}{\cos\alpha_R^{(l,m)}}. \tag{76}$$

Now, $\alpha_R^{(l,m)}$ can also be expressed in terms of $\epsilon_T^{(l,m)}$ and $\alpha_T^{(l,m)}$ using the sine rule:

$$\frac{\epsilon_T^{(l,m)}}{\sin(\pi - \alpha_R^{(l,m)})} \;=\; \frac{D}{\sin(\alpha_R^{(l,m)} - \alpha_T^{(l,m)})}. \tag{77}$$

Using (76) and (77), $\epsilon_R^{(l,m)}$ can be written as

$$\epsilon_R^{(l,m)} \;=\; \frac{R_t^{(l)} \cos\alpha_T^{(l,m)} - D}{\cos\left[\tan^{-1}\left(-\frac{R_t^{(l)} \sin\alpha_T^{(l,m)}}{D - R_t^{(l)} \cos\alpha_T^{(l,m)}}\right) + \pi\right]}, \tag{78}$$

Now we show the derivations for (44). From Fig. 62, we can represent the length of $\epsilon_S^{(l,m,p,q)}$ as a sum of the projections to x- and y-axis, i.e., $\epsilon_S^{(l,m,p,q)} = \sqrt{X^2 + Y^2}$.

We can find X projection by solving the following equations:

$$X \;=\; D - (Z + W) \tag{79}$$

$$X + Z \;=\; \epsilon_T^{(l,m)} \cos\alpha_T^{(l,m)} \tag{80}$$

$$X + W \;=\; \epsilon_R^{(p,q)} \cos(\pi - \alpha_R^{(p,q)}), \tag{81}$$

where Z and W are, respectively, the distances $A_T - S^{(p,q)}$ and $A_R - S^{(l,m)}$ projected onto the x-axis. Adding (80) and (81), we get

$$2X + Z + W = \epsilon_T^{(l,m)} \cos \alpha_T^{(l,m)} - \epsilon_R^{(p,q)} \cos \alpha_R^{(p,q)}. \tag{82}$$

Then, substituting (79) into (82), X can be written as:

$$X = \left| \epsilon_T^{(l,m)} \cos \alpha_T^{(l,m)} - \epsilon_R^{(p,q)} \cos \alpha_R^{(p,q)} - D \right|. \tag{83}$$

Using similar reasoning, Y component can be written as:

$$Y = \left| \epsilon_T^{(l,m)} \sin \alpha_T^{(l,m)} - \epsilon_R^{(p,q)} \sin \alpha_R^{(p,q)} \right|. \tag{84}$$

Then, the final expression for $\epsilon_S^{(l,m,p,q)}$ is

$$\epsilon_S^{(l,m,p,q)} = \left[\left| \epsilon_T^{(l,m)} \sin \alpha_T^{(l,m)} - \epsilon_R^{(p,q)} \sin \alpha_R^{(p,q)} \right|^2 + \left| \epsilon_T^{(l,m)} \cos \alpha_T^{(l,m)} - \epsilon_R^{(p,q)} \cos \alpha_R^{(p,q)} - D \right|^2 \right]^{1/2}. \tag{85}$$

APPENDIX C

THE SR, DR, AND LOS COMPONENTS OF THE TIME-INVARIANT TRANSFER FUNCTION

Using (38) - (45), the SR, DR, and LoS components of the time-invariant transfer function in (47) can be written as

$$T^{SR}(f) = \lim_{M\to\infty} \sqrt{\frac{\eta_{SR}}{K+1}} \frac{1}{\sqrt{M}} \sum_{l=1}^{L} \sum_{m=1}^{M^{(l)}} A_{SR}^{(l,m)}\ e^{-j2\pi f \tau_{SR}^{(l,m)} + j\phi_{SR}^{(l,m)}}, \tag{86}$$

$$T^{DR}(f) = \lim_{M,Q\to\infty} \sqrt{\frac{\eta_{DR}}{K+1}} \frac{1}{\sqrt{MQ}} \sum_{l,m=1}^{L,M^{(l)}} \sum_{p,q=1}^{P,Q^{(p)}} A_{DR}^{(l,m,p,q)}\ e^{-j2\pi f \tau_{DR}^{(l,m,p,q)} + j\phi_{DR}^{(l,m,p,q)}}, \tag{87}$$

$$T^{LoS}(f) = \sqrt{\frac{K}{K+1}}\ A_{LoS}\ e^{-j2\pi f \tau_{LoS} + j\phi_{LoS}}, \tag{88}$$

respectively, where the amplitudes, $A_{SR}^{(l,m)}$, $A_{DR}^{(l,m,p,q)}$, and A_{LoS}, and the time delays, $\tau_{SR}^{(l,m)}$, $\tau_{DR}^{(l,m,p,q)}$, and τ_{LoS}, are defined in [69].

APPENDIX D

THE APPROXIMATED FCF OF THE SR AND DR COMPONENTS

The expression in (54) can be further simplified by noting that distance in (43) can be approximated as

$$\epsilon_R^{(l,m)} \approx D - R_t^{(l)} \cos \alpha_T^{(l,m)} \tag{89}$$

under the assumption of Eq. (58). The expression in (89) is obtained using the trigonometric identity $\cos(\tan^{-1} x) = 1/\sqrt{1+x^2}$. Now applying the approximation $(1+x)^n \approx 1 + nx$ for small x, we obtain the expression for the approximated FCF of the SR component as in (56).

The expression in (55) can be further simplified by noting that distance in (44) can be approximated as

$$\epsilon_S^{(l,m,p,q)} \approx \left| R_t^{(l)} \cos \alpha_T^{(l,m)} - R_r^{(p)} \cos \alpha_R^{(p,q)} - D \right|. \tag{90}$$

Without loss of generality, we have assumed that $R_t^{(l)} = R_r^{(p)}$ and $\alpha_R^{(p,q)} = \pi - \alpha_T^{(l,m)}$, which leads to the expression for the approximated FCF of the DB component as in (57).

REFERENCES

[1] I.F. Akyildiz, D.M. Gutierrez-Estevez, R. Balakrishnan, E. Chavaria-Reyes, "LTE-advanced and the evolution to beyond 4G (B4G) systems." *Phy. Commun. (Elsevier) J.*, vol. 10, pp. 31–60, March 2014.

[2] P. Smulders, "Exploiting the 60 GHz bandfor local wireless multimedia access: prospects and future directions," *IEEE Commun. Mag.*, vol. 40, no. 1, pp. 140–147, 2002.

[3] M. Fryziel, C. Loyez, L. Clavier, N. Rolland, and P. A. Rolland, "Path-loss model of the 60-GHz indoor radio channel," *Microw. and Opt. Technology Lett.*, vol. 34, no. 3, pp. 158–162, 2002.

[4] H. Xu, V. Kukshya, and T. S. Rappaport, "Spatial and temporal characteristics of 60-GHz indoor channels," *IEEE J. Sel. Areas Commun.*, vol. 20, no. 3, pp. 620–630, April 2002.

[5] N. Moraitis and P. Constantinou, "Indoor channel measurements and characterization at 60 GHz for wireless local area network applications," *IEEE Trans. Antennas Propag.*, vol. 52, no. 12, pp. 3180–3189, December 2004.

[6] T. Zwick, T. J. Beukema, and H. Nam, "Wideband channel sounder with measurements and model for the 60 GHz indoor radio channel," *IEEE Trans. Veh. Technol.*, vol. 54, no. 4, pp. 1266–1276, July 2005.

[7] H. Yang, P. F. M. Smulders, and M. H. A. J. Herben, "Indoor channel measurements and analysis in the frequency bands 2 GHz and 60 GHz," *Proc. IEEE Symp. Pers. Indoor Mob. Radio Commun.*, pp. 1–5, September 2005.

[8] S. Geng, J. Kivinen, X. Zhao, and P. Vainikainen, "Millimeter-wave propagation channel characterization for short-range wireless communications," *IEEE Trans. Veh. Technol.*, vol. 58, no. 1, pp. 3–13, January 2009.

[9] M. Peter and W. Keusgen, "Analysis and comparison of indoor wideband radio channels at 5 and 60 GHz," *Proc. European Conf. Antennas and Propag. EUCap09*, pp. 3830–3834, March 2009.

[10] T. Rappaport, J. Murdock, F. Gutierrez, "State of the art in 60-GHz integrated circuits and systems for wireless communicaitons." *Proc. IEEE*, vol. 99, pp. 1390–1436, 2011.

[11] M. Koch, "Terahertz communications: a 2020 vision", in: R. Miles, X.C. Zhang, H. Eisele, A. Krotkus(Eds.), "Terahertz Frequency Detection and Identification of Materials and Objects", in: *NATO Security through Science Series*, vol. 19, pp. 325–338, 2007.

[12] B. Glushko, D. Kin, A. Shar, "Gigabit optical wireless communication system for personal area networking." *Opt. Mem. Neural Netw.*, vol. 22, pp. 73–80, 2013.

[13] A.H. Azhar, T.A. Tran, D. O'Brien, "A gigabit/s indoor wireless transmission using MIMO-OFDM visible light communications." *IEEE Photonics Techno. Lett.*, vol. 25, pp. 171–174, 2013.

[14] X. Li, J. Vucic, V. Jungnickel, J. Armstrong, "On the capacity of intensity-modulated direct-detection systems and the information rate of aco-ofdm for indoor optical wireless applications." *IEEE Trans. Commun.*, vol. 60, pp. 799–809, 2012.

[15] E. Ciaramella, Y. Arimoto, G. Contestabile, M. Presi, A. D'Errico, V. Guarino, M. Matsumoto, "1.28 terabit/s (32*40 Gbit/s) wdm transmission system for free space optical communications." *IEEE J. Sel. Areas Commun.*, vol. 27, pp. 1639–1645, 2009.

[16] D. B. Rutledge and M. S. Muha, "Imaging antenna arrays," *IEEE Transactions on Antennas and Propagation*, vol. 30, no. 4, pp. 535–540, July 1982.

[17] D. F. Filippovic, S. S. Gearhart, and G. M. Rebeiz, "Double slot on extended hemispherical and elliptical silicon dielectric lenses," *IEEE Transactions on Microwave Theory and Techniques*, vol. 41, no. 10, pp. 1738–1749, October 1993.

[18] X. Wu, G. Eleftheriades, and T. E. van Deventer-Perkins, "Design and characterization of single and multiple beam MM-wave circularly polarized substrate lens antennas for wireless communications," *IEEE Transactions on Microwave Theory and Techniques*, vol. 49, no. 3, pp. 431–441, March 2001.

[19] A. V. Boriskin, G. Godi, R. Sauleau, and A. I. Nosich, "Small hemielliptic dielectric lens antenna analysis in 2-D: Boundary integral equations versus geometrical and physical optics," *IEEE Transactions on Antennas and Propagation*, vol. 56, no. 2, pp. 485–492, February 2008.

[20] P. Focardi, W. R. McGrath, and A. Neto, "Design guidelines for terahertz mixers and detectors," *IEEE Transactions on Microwave Theory and Techniques*, vol. 53, no. 5, pp. 1653–1661, May 2005.

[21] A. Neto, S. Bruni, G. Gerini, and M. Sabbadini, The leaky lens: A broad band, fixed beam leaky wave antenna, IEEE Trans. Antennas Propag., vol. 53, no. 10, pp. 3240–3246, Oct. 2005.

[22] S. Bruni, A. Neto, and F. Marliani, "The UWB leaky lens antenna," *IEEE Transactions on Antennas and Propagation*, vol. 55, no. 10, pp. 2642–2653, October 2007.

[23] A. Neto, "UWB, non-dispersive radiation from the planarly fed leaky lens antenna-part I: theory and design," *IEEE Transactions on Antennas and Propagation*, vol. 58, no. 7, pp. 2238–2247, July 2010.

[24] A. Neto, S. Monni, and F. Nennie, "UWB, non-dispersive radiation from the planarly fed leaky lens antenna-part II: demonstrators and measurements," *IEEE Transactions on Antennas and Propagation*, vol. 58, no. 7, pp. 2248–2258, July 2010.

[25] N. Llombart, G. Chattopadhyay, A. Skalare, and I. Mehdi, "Novel terahertz antenna based on a silicon lens fed by a leaky wave enhanced waveguide," *IEEE Transactions on Antennas and Propagation*, no. 6, pp. 2160–2168, June 2011.

[26] Y. Fuh, A. Margomenos, Y. Jiang, and L. Lin, "Micromachined W-band plastic slot array antenna with self-aligned and integrated flange," *15th Annual International Conference on Solid-State Sensors, Actuators, and Microsystems*, pp. 2122-2125, June 2009.

[27] T. Tick, J. Jantti, M. Henry, C. Free, and H. Jantunen, "LTCC integrated air-filled waveguide for G-band applications," *Microwave and Optical Technology Letters*, vol. 51, no. 1, pp. 176-178, 2009.

[28] M. Henry, C. E. Free, B. S. Izqueirdo, J. Batchelor, and P. Young, "Millimeter wave substrate integrated waveguide antennas: design and fabrication analysis," *IEEE Transactions on Advanced Packaging*, vol. 32, pp. 93-100, February 2009.

[29] Y. Wang, M. Ke, M. J. Lancaster, and J. Chen, "Micromachined 300-GHz SU-8-based slotted waveguide antenna," *IEEE Antennas and Wireless Propagation Letters*, vol. 10, pp. 573–576, 2011.

[30] M. Jenning, and D. Plettemeier, "Multilayer and multidirectional linearly-tapered slot antenna for 300 GHz applications, *The 4th European Conference on Antennas and Propagation (EuCAP10)*, pp. 1–5, Barcelona Spain, April 2010.

[31] P. H. Siegel, "Terahertz technology", *IEEE Transactions on Microwave Theory and Techniques*, vol. 50, pp. 910–928, March 2002.

[32] S. Priebe, C. Jastrow, M. Jacob, T. Kleine-Ostmann, T. Schrader, T. Kürner, "Channel and propagation measurements at 300 GHz," *IEEE Transactions on Antennas and Propagation*, vol. 59, no. 5, pp. 1688–1698, May 2011.

[33] R. Piesiewicz, T. Kleine-Ostmann, N. Krumbholz, D. Mittleman, M. Koch, J. Schoebel, and T. Kürner, "Short-range ultra-broadband terahertz communications: Concepts and perspectives," *IEEE Antennas Propagation Mag.*, vol. 49, pp. 24-39, June 2007.

[34] R. Piesiewicz, C. Jansen, D. Mittleman, T. Kleine-Ostmann, M. Koch, and T. Kürner, "Scattering analysis for the modeling of THz communication systems," *IEEE Trans. Antennas Propagation*, vol. 55, pp. 3002-3009, November 2007.

[35] S. Priebe, M. Jacob, C. Jastrow, T. Kleine-Ostmann, T. Schrader, and T. Kürner, "A comparison of indoor channel measurements and ray tracing simulations at 300 GHz," *Proc. Int. Conf. Infrared Millim. Terahertz Waves (IRMMW-THz)*, 2010.

[36] G. Liu and E. K. Seo,"Detecting snowfall over land by satellite high-frequency microwave observations: The lack of scattering signature and a statistical approach," *Journal of geophysical research: atmospheres*, vol. 118, 1376-1387, February 2013.

[37] Z. Chen and J. C. Cao,"Channel characterization at 120 GHz for future indoor communication systems," *Chin. Phys. B*, vol. 22, No. 5, 059201, 2013.

[38] A. Naeemi, R. Sarvari, and J. Meindl, "On-chip interconnect networks at the end of the roadmap: limits and nanotechnology opportunities," *International Interconnect Technology Conference (IITC)*, 2006.

[39] G. Chen, H. Chen, M. Haurylau, N. Nelson, D. Albonesi, P. Fauchet, and E. Friedman, "On-chip copper-based vs. optical interconnects: delay uncertainty, latency, power, and bandwidth density comparative predictions." *Proc. International Interconnect Technology Conference (IITC)*, 2006.

[40] K. Banerjee, S. J. Souri, P. Kapur, and K. C. Saraswat, "3-D ICs: A novel chip design for improving deep-submicrometer interconnect performance and systems-on-chip integration," *Proc. IEEE*, vol. 89, pp. 602-633, May 2001.

[41] D. A. B. Miller, "Rationale and challenges for optical interconnects to electronic chip," *Proc. IEEE*, vol. 88, pp. 728-749, June 2000.

[42] R. H. Havemann and J. A. Hutchby, "High-performance interconnects: An integration overview," *Proc. IEEE*, vol. 89, pp. 586-601, May 2001.

[43] K. Ramachandran, R. Kokku, R. Mahindra, and S. Rangarajan "60GHz data-center networking: Wireless -¿ worry less?" Technical report, NEC, 2008.

[44] B. A. Floyd, C.-M. Hung, and K. K. O, "Intra-chip wireless interconnect for clock distribution implemented with integrated antenna, receiver, and transmitters," *IEEE J. Solid-State Circuits*, vol. 37, pp. 543-552, May 2002.

[45] M. Sun and Y. P. Zhang, "Performance of inter-chip RF-interconnect using CPW, capacitive coupler and UWB transceiver," *IEEE Trans. Microwave Theory Tech.*, vol. 53, pp. 2650-2655, September 2005.

[46] M. G. Pettus and J. R. A. Bardeen, "System and method for wireless communication in a backplane fabric architecture," U.S. Patent No. 7,929,474B2, April 19, 2011.

[47] J. S. Wesolowski, "Ultra-wideband wireless backplane," U.S. Patent No. 7,373,107B1, May 13, 2008.

[48] M. Chang, V. Roychowdhury, L. Zhang, H. Shin, and Y. Qian, "RF/wireless interconnect for inter- and intra-chip communications," *Proc. IEEE*, vol. 89, pp. 456–466, April 2001.

[49] K. K. O, K. Kim, B. Floyd, J. Mehta, H. Yoon, C.-M. Hung, D. Bravo, T. Dickson, X. Guo, R. Li, N. Trichy, J. Caserta, W. Bomstad, J. Branch, D.-J. Yang, J. Bohorquez, J. Chen, E.-Y. Seok, L. Gao, A. Sugavanam, J.-J. Lin, S. Yu, C. Cao, M.-H. Hwang, S.-H. Hwang, H. Wu, N. Zhang, and J. E. Brewer, "The feasibility of on-chip interconnection using antennas," *IEEE/ACM International Conference on Computer-Aided Design ICCAD-2005*, pp. 979–984, 6-10 November 2005.

[50] J.-Y. Shin, E. G. Sirer, and D. Kirovsi, "On the feasibility of completely wireless data centers," Technical Reports, Cornell University (2011).

[51] A. Valdes-Garcia, S. Reynolds, A. Natarajan, and D. Kam, "Single-element and phased-array transceiver chipsets for 60-GHz Gb/s communications," *IEEE Communications Magazine*, vol. 49, pp. 120–131, April 2011.

[52] H. Vardhan, N. Thomas, S.-R. Ryu, B. Banerjee, and R. Parkash, "Wireless data center with millimeter wave network," *IEEE Proceeding of GLOBECOM10*, pp. 1–6, December 2010.

[53] D. Halperin, S. Kandula, J. Padhye, P. Bahl, and D. Wetherall, "Augmenting data center networks with multi-gigabit wireless links," *Proc. of ACM SIGCOMM*, pp. 38–49, August 2011.

[54] K. Kawasaki, Y. Akiyama, K. Komori, M. Uno, H. Takeuchi, T. Itagaki, Y. Hino, Y. Kawasaki, K. Ito and A. Hajimiri, "A millimeter-wave intra-connect solution," *IEEE Journal of Solid-State Circuits*, vol. 45, no. 12, pp. 2655–2666, December 2010.

[55] J. Branch, X. Guo, L. Gao, A. Sugavanam, J.-J. Lin, and K. K. O., "Wireless communication in a flip-chip package using integrated antennas on silicon substrates," *IEEE Electron Device Letters*, vol. 26, pp. 115–117, February 2005.

[56] K. K. O, K. Kim, B. A. Floyd, J. L. Mehta,H. Yoon,C.-M. Hung, D. Bravo, T. O. Dickson, X. Guo, R. Li, N. Trichy, J. Caserta, W. R. Bomstad, J. Branch, D.-J. Yang, J. Bohorquez, E. Seok, L. Gao, A. Sugavanam, J.-J. Lin, J. Chen, and J. E. Brewer, "On-chip antennas in silicon ICs and their application," *IEEE Transactions on Electron Devices*, vol. 52, pp. 1312–1323, July 2005.

[57] Z. M. Chen and Y. P. Zhang, "Inter-chip wireless communication channel: measurement, characterization, and modeling," *IEEE Transactions on Antennas and Propagation*, vol. 55, pp. 978-986, March 2007.

[58] J. Karedal, A. Singh, F. Tufvesson, and A. Molisch, "Characterization of a computer board-to-board ultra-wideband channel," *IEEE Communications Letters*, vol. 11, pp. 468-470, June 2007.

[59] J. Gelabert, D. J. Edwards and C. J. Stevens, "Experimental evaluation of UWB wireless communication within PC case," *Electronics Letters*, vol. 47, pp. 773–775, June 2011.

[60] H. Chong, A. Bicen, and I. F. Akyildiz, "Multi-ray channel modeling and wideband characterization for wireless communications in the terahertz band," *IEEE Transactions on Wireless Communications*, vol. 14, no. 5, pp. 2402-2412, May 2015.

[61] M. Jacob, S. Priebe, R. Dickhoff, T. Kleine-Ostmann, T. Schrader, T. Kurner, "Diffraction in mm and sub-mm wave indoor propagation channels," *IEEE Transactions on Microwave Theory and Techniques*, vol. 60, no. 3, pp. 833–844, March 2012.

[62] S. Priebe and T. Kürner, "Stochastic modeling of THz indoor radio channels," *IEEE Transactions on Wireless Communications*,vol. 12, no. 9, pp. 4445-4455, September 2013.

[63] A. F. Molisch, "Ultrawideband propagation channels-theory, measurement, and modeling," *IEEE Transactions on Vehicular Technology*, vol. 54, no. 5, pp. 1528-1545, September 2005.

[64] A. A. M. Saleh and R. A. Valenzuela, "A statistical model for indoor multipath propagation," *IEEE Journal on Selected Areas in Communications*, vol. 5, no. 2, pp. 128-137, February 1987.

[65] T. S. Rappaport, S. Sun, R. Mayzus, H. Zhao; Y. Azar, K. Wang, G. N. Wong, J. K. Schulz, M. Samimi, F. Gutierrez, "Millimeter wave mobile communications for 5G Cellular: it will work!," *Access, IEEE*, vol. 1, pp.335–349, May 2013.

[66] S. Kim, A. Zajić, "300 GHz Linearly Tapered Slot Antenna Design and Measurements," *Microwave and Optical Technology Letters* vol. 57, pp.713–717, March 2015.

[67] S. Kim, A. Zajić, "Statistical characterization of 300-GHz propagation on a desktop," *IEEE Transactions on Vehicular Technology* vol. 64, pp. 3330-3338, August 2015.

[68] S. Kim, A. Zajić, "Path loss model for 300-GHz wireless channels," *Proc. of IEEE International Symposium on Antennas and Propagation*, pp. 1–2, Memphis, Tennessee, USA, July 2014.

[69] S. Kim, W.T. Khan, A. Zajić, and J. Papapolymerou, "D-Band Channel Measurements and Characterization for Indoor Applications," *IEEE Transactions on Antennas and Propagation*, vol. 63, pp. 3198–3207, July 2015.

[70] W. Khan, S. Kim, A. Zajić, and J. Papapolymerou, D-band Indoor Path Loss Measurements, *Proc. of 2014 IEEE Antennas and Propagation Society International Symposium (APSURSI 2014)*,pp. 1173-1174, Memphis, Tennessee, USA, July 2014.

[71] S. Kim, A. Zajić, "UTD-Based Modeling of Diffraction Loss by Dielectric Circular Cylinders at D-band," to appear in *Proc. of IEEE APS/URSI 2016*.

[72] S. Kim, A. Zajić, "Characterization of 300 GHz Wireless Channel on a Computer Motherboard," to appear in *IEEE Transactions on Antennas and Propagation*

[73] S. Kim and A. Zajić, "300 GHz path loss measurements on computer motherboard," *10th European Conference on Antennas and Propagation*, Davos, Switzerland, April 2016.

[74] S. Kim, A. Zajić, "Statistical Modeling and Simulation of Short-Range Device-to-Device Communication Channels at sub-THz Frequencies," to appear in *IEEE Transactions on Wireless Communications*

[75] S. Kim and A. Zajić, "Statistical Modeling of THz Scatter Channels," *Proc. European Conf. Antennas and Propag. EUCap09*, pp. 1–5, Lisbon, Portugal, April 2015

[76] G.L. Stuber, *Principles of mobile communication*, 2nd ed. Norwell, MA: Kluwer, 2001.

[77] O.S. Heavens, *Optical Properties of Thin Film Solids*, New York, Dover, 1965.

[78] K. Heidary, "Ultra-wideband (UWB) incidence on multiple dielectric interfaces," *IEEE Antennas and Propagation Society Symp.*, 2004, pp. 1315-1318.

[79] R. Yao, Z. Chen, Z. Guo, "An efficient multipath channel model for UWB home networking," *IEEE Radio Wireless Conf.*, 2004, pp. 511-516.

[80] R. Qiu, "Propagation effects," *UWB Communications Systems-a Comprehensive Overview*, M.G. Di Benedetto *et al.*, Ed.: EURASIP publishing, 2005.

[81] R. Vaughan, J.B. Andersen, *Channels, Propagation, and Antennas for Mobile Communications*, IEE Press, 2003.

[82] C. Jansen, R. Piesiewicz, D. Mittleman, T. Kürner, and M. Koch, "The impact of reflections from stratified building materials on the wave propagation in future indoor terahertz communication systems," *IEEE Trans. Antennas Propagation*, vol. 56, no. 5, pp. 1413-1419, 2008.

[83] R. Piesiewicz, T. Kleine-Ostmann, N. Krumbholz, D. Mittleman, M. Koch, and T. Kürner, "Terahertz characterisation of building materials," *IEEE Electronic Letters*, vol. 41, pp. 1002-1004, 2005.

[84] G. Kadel, R. Lorenz, "Impact of the radio channel on the performance of digital mobile communication systems," *Proc. Sixth IEEE Int. Symp. Personal, Indoor and Mobile Radio Comm. PIMRC95*, 1995, pp. 419-423.

[85] J.P. Rossi, "Influence of measurement conditions on the evaluation of some radio channel parameters," *IEEE Trans. Veh. Technol.*, vol. VT-48, pp. 1304-1316, Jul. 1999.

[86] S. Venkatesh, J. Ibrahim, R. M. Buehrer, "A new 2-cluster model for indoor UWB channel measurements," *Proc. IEEE Antennas Propagation Symp.*, 2004, pp. 946-949.

[87] A. F. Molisch *et al.*, "A comprehensive model for ultrawideband propagation channels of UWB system proposals standard for these applications," *Proc. IEEE Globecom*, 2005.

[88] A. F. Molisch *et al.*, "IEEE 802.15.4a ChannelModel-FinalReport," Tech. Rep., Document IEEE 802.1504-0062-02-004a, 2005.

[89] D. Cassioli, M. Z. Win, A. F. Molisch, "The ultra-wide bandwidth indoor channel: From statistical model to simulations," *IEEE J. Sel. Areas Commun.*, pp. 1247-1257, 2002.

[90] J. Karedal, S. Wyne, P. Almers, F. Tufvesson, A. F. Molisch, "Statistical analysis of the UWB channel in an industrial environment," *Proc. VTC Fall 2004*, 2004, pp. 81-85.

[91] C. C. Chong, Y. Kim, S. S. Lee, "A modified S-V clustering channel model for the UWB indoor residential environment," *Proc. IEEE VTC Spring 2005*, 2005.

[92] B. Kannan *et al.*, "UWB Channel Characterization in Office Environments," IEEE, Tech. Rep. Document IEEE 802.15-04-0439-00-004a, 2004.

[93] B. Kannan *et al.*, "UWB Channel Characterization in Outdoor Environments," IEEE, Tech. Rep. Document IEEE 802.15-04-0440-00-004a, 2004.

[94] D. Cassioli, A. Durantini, "A time domain propagation model of the UWB indoor channel in the FCC-compliant band 3.66 GHz based on pn-sequence channel measurements," *Proc. VTC04 Spring*, 2004, pp. 213-217.

[95] D. Cassioli, A. Durantini, W. Ciccognani, "The role of path loss on the selection of the operating bands of UWB systems," *Proc. IEEE Int. Symp. Personal, Indoor and Mobile Radio Communications*, 2004, pp. 2787-2791.

[96] J. Kunisch and J. Pamp, "Measurement results and modeling aspects for the UWB radio channel," *Proc. IEEE UWBST*, 2002, pp. 19-23.

[97] V. Hovinen, M. Hämäläinen, T. Pätsi, "Ultra wideband indoor radio channel models: Preliminary results," *Proc. IEEE UWBST*, 2002, pp. 75-79.

[98] J. R. Foerster, Q. Li, "UWB channel modeling contribution from intel," IEEE, Tech. Rep. P802.15 02/279SG3a, 2002, IEEE P802.15 SG3a Contribution.

[99] S. S. Ghassemzadeh, R. Jana, C. W. Rice, W. Turin, V. Tarokh, "Measurement andmodeling of an ultra-wide bandwidth indoor channel," *IEEE Tran. Commun.*, vol. 52, pp. 1786-1796, 2004.

[100] A. Alvarez, G. Valera, M. Lobeira, R. Torres, J. L. Garcia, "New channel impulse response model for UWB indoor system simulations," *Proc. VTC 2003 Spring*, 2003, pp. 1-5.

[101] P. Pagani, P. Pajusco, "Experimental assessment of the UWB channel variabilityin a dynamic indoor environment," *Proc. IEEE PIMRC 2004*, 2004, pp. 2973-2977.

[102] (2010) CST Website. [Online]. Available: http://www.cst.com/

[103] http://www.kratosepd.com/ /media/EP/Datasheets/

[104] http://www.nordengroup.com/products/frequency-multipliers/frequency-multiplier-33-to-50-ghz/

[105] http://vadiodes.com/index.php/en/products/broadband-multipliers/10-products/165-wr65x3

[106] http://www.vadiodes.com/index.php/en/12-product/126-wr28shm12

[107] T. Rappaport, *Wireless communications: principles and practice*, Upper Saddle River, NJ, USA: Pretince Hall PTR, 2001.

[108] A. Zajić, *Mobile-to-mobile wireless channels*, Artech Houlse, Boston MA, January 2013.

[109] D. Pozar, *Microwave Engineering*, John Wiley and Sons, Inc., NJ, USA, 2012.

[110] T. Kosugi, M. Tokumitsu, K. Murata, T. Enoki, H. Takahashi, A. Hirata, T. Nagatsuma,"120-GHz Tx/Rx waveuide modules for 10-Gbit/s wireless link system," *2006 IEEE CSICS Dig.*, pp. 25–28, October, 2006.

[111] I. Sarkas, E. Laskin, J. Hasch, P. Chevalier, S. P. Voinigescu, "Second generation transcievers for D-band radar and data communication applications," *2010 IEEE IMS Dig.*, pp. 1328–1331, May, 2010.

[112] E. Laskin, M. Khanpour, S. T. Nicolson, A. Tomkins, P. Garcia, A. Cathelin, D. Belot, S. P. Voinigescu, "Nanoscale CMOS transciever design in the 90-170 GHz range," *IEEE Transactions on Mocrowave Theory and Techniques*, MTT-57, pp. 3477–3490, December 2009.

[113] D. A. McNamara, *et al.*, "Introduction to the Uniform Geometrical Theory of Diffraction", Artech House, MA, 1990.

[114] Infiniband Trade Association, "InfiniBand continues growth among supercomputers on TOP500 list", November 2014 $http : //www.infinibandta.org/content/pages.php?pg = press_room_item\&rec_id = 805$

[115] InfiniBand Trade Association, "InfiniBand roadmap", $http : //www.infinibandta.org/content/pages.php?pg = technology_overview$

[116] Wikipedia, Wireless Gigabit Alliance, $https : //en.wikipedia.org/wiki/Wireless_Gigabit_Alliance$

[117] I. Angulo, D. de la Vega, C. Fernandez, Y. Wu, P. Angueira, J. L. Ordiales, "*An Empirical Comparative Study of Prediction Methods for Estimating DTV Signal Scattering from Wind Turbines*", IEEE Trans. Broadcasting, vol. 57, no. 2, pp. 195–203, June 2011.

[118] L. J. Greenstein, D. G. Michelson, and V. Erceg, "Moment-method estimation of the Ricean K-factor," *IEEE Commun. Letters*, vol. 3, pp. 175–176, June 1999.

[119] A. G. Zajić, G. L. Stuber, T. G. Pratt, and S. Nguyen, "Wide-band MIMO mobile-to-mobile channels: statistical modeling with experimental verification", *IEEE Transactions on Vehicular Technology*, vol. 58, pp. 517–534, February 2009.

[120] R. Saadane, A. Khafaji, J. El Abbadi, and M. Belkasmi, "The influence of people shadowing on the modelling of 60 GHz Band propgation," *Recent Advances in Technoolgoies*, Intech, pp. 275–290, Nov. 2009.

VITA

Seunghwan Kim was born in Seoul, South Korea, on January 29^{th}, 1986. He received Bachelor of Applied Science in Electrical Engineering with Distinction from University of Waterloo, Canada, in 2009. During his degree, he has worked as a Research Assistant at the Telecommunication Group of Korea Electrotechnology Research Institute (KERI), and as a Hardware Engineer at Mitel Networks.

After serving his country from 2010 to 2012 in the Republic of Korea Air Force (ROKAF), he began pursuing his Ph.D. degree in the fall of 2012 with the Electromagnetic Measurements in Communications and Computing (EMC^2) lab in the School of Electrical and Computer Engineering at Georgia Institute of Technology. His research interests are in the area of applied electromagnetics, antenna design, and THz wireless communications.